2022-12-08

Improving Spatial Resolution of Time Reversal Focusing Using Arrays of Acoustic Resonators

Adam David Kingsley
Brigham Young University

Improving Spatial Resolution of Time Reversal Focusing Using Arrays of Acoustic Resonators

Adam David Kingsley

A dissertation submitted to the faculty of
Brigham Young University
in partial fulfillment of the requirements for the degree of

Doctor of Philosophy

Brian E. Anderson, Chair
Scott D. Sommerfeldt
Tracianne B. Neilsen
Karl F. Warnick
Matthew S. Allen

Department of Physics and Astronomy

Brigham Young University

ABSTRACT

Improving Spatial Resolution of Time Reversal Focusing Using Arrays of Acoustic Resonators

Adam David Kingsley
Department of Physics and Astronomy, BYU
Doctor of Philosophy

Using a near-field array of acoustic resonators, it is possible to modify a focused pressure field and enforce a spatial frequency corresponding to the resonator array spacing. This higher spatial frequency makes it possible to focus and image with a resolution that is better than if the focusing were in free space. This near-field effect is caused by the phase shifting properties of resonators and, specifically, the delayed phase found in waves with a temporal frequency lower than that of the resonators in the array. Using time reversal, arrays of resonators are explored and the subwavelength focusing is used to describe the ability to image subwavelength features. A one-dimensional equivalent circuit model accurately predicts this interaction of the wave field with an array of resonators and is able to model the aggregate effect of the phononic crystal of resonators while describing the fine spatial details of individual resonators. This model is validated by a series of COMSOL full-wave simulations of the same system. The phase delay caused by a single resonator is explored in a simple experiment as well as in the equivalent circuit model. A series of experiments is conducted with a two-dimensional array of resonators and complex images are produced which indicate the ability to focus complex sources with better resolution.

Keywords: super resolution, time reversal, equivalent circuit, near-field imaging, spatial inverse filter, acoustic resonators

ACKNOWLEDGMENTS

This work represents the scientific exploration and the journey of many years. I acknowledge the support of my wife who encouraged me to pursue this degree and helped to make it a reality.

I acknowledge the funding I have received from the BYU College of Physical and Mathematical Sciences. I also appreciate the many professors that helped me to conduct this research. The members of my committee have been a wealth of information and direction. Although not on my committee, I would like to thank Dr. Michael Ware for his advice and direction about optical analogs to the acoustic phenomena I was researching.

I recognize the many students that have helped me in this work: Lucas Barnes, Carla Wallace, Rebekah Higgins, Emily Golightly, Jay Clift, Andrew Basham, and Rylee Russell. They have contributed significant amounts of time and effort to further the research.

I am grateful to the researchers at Los Alamos National Laboratory for crafting this project and funding the research that has produced this dissertation. Funding was provided through subcontract No. 527136, under the technology maturation program.

I am indebted to my advisor, Dr. Brian Anderson. He has taught me how to be a physicist and an experimentalist. He has taught me how to write to be understood and he has spent countless hours directing and guiding this project. Most of all, I am grateful that he cared about me as a person, as well as my success as a graduate student.

TABLE OF CONTENTS

LIST OF FIGURES

LIST OF TABLES

Chapter 1

Introduction

This dissertation describes three approaches used to analyze sub-diffraction limited focusing of acoustic waves using resonators. The three approaches consist of analytical, numerical, and experimental methods. These three directions explore the wave physics that result from acoustic waves and resonator interactions. These effects may not be immediately intuitive, however, the models and physical descriptions contained in this dissertation attempt to make a physical understanding more accessible.

Propagating waves have a characteristic wavelength that can be determined by the temporal frequency and the speed of the wave. These characteristics do not change as linear, propagating waves travel. Specifically, no combination of waves can yield modulations that are smaller than the modulations of the highest frequencies. However, when waves encounter a change in the medium, or a boundary condition, the waves conform to the boundary. That is, waves that interact with other media or objects, must maintain certain conditions at the boundary between media. The boundaries are under no constraint concerning resolution. Thus, a boundary may modulate with a spatial frequency (wavenumber) that is much higher than the free-space spatial frequency of the incoming wave. Thus, a wave impinging on a boundary may have a much higher spatial frequency than the same wave possessed when it was propagating. This spatial frequency modulation resulting from boundary-wave interaction does not propagate to distances

far away from this boundary and are, thus, termed *near-field* behaviors; the resulting modified waves are termed *evanescent* waves. These two types of waves (*propagating* and *evanescent*) are a way of describing the waves that exist in and throughout a system interacting with objects and boundaries in the domain.

One way to discuss the impact of boundaries is in terms of the *diffraction limit*. The diffraction limit is a generally ill-defined term [1]. It is worth noting that much of the understanding expressed in this introduction regarding the diffraction limit comes from Ref. [1]. Though it has been refined by some authors, the normal use conveys a general intuition rather than an exact limit. Specifically, the diffraction limit is used to describe two different but related limits to focusing resolution. The first limit is the diffraction as a wave passes through an aperture. Often a circular aperture is used, and the resulting diffraction pattern is called an Airy disk. However, without noise, there is no limit when trying to resolve two Airy disks because the pattern is known. This limit is just a good rule of thumb about when two Airy disks should be considered "resolved." The other context for using the diffraction limit is the focusing of waves onto an imaging plane, and the diffraction limit is used to describe the full width at half maximum (FWHM) of the converging waves. Even in this case, there is no limit to the FWHM as the aperture can be altered to create an arbitrarily small FWHM at the expense of large sidelobes [1]. However, with a complete aperture, the diffraction limit gives a sense of the size of the focal spot generated by the interference of the incoming and outgoing waves.

This is easily understood in one dimension where incoming waves arrive from the left and right. The resulting wave is a standing wave with the same wavelength as the incoming waves. This means that the size of the modulations in the wave is the same size as the focus of these two incoming waves. In higher dimensions the problem gets worse. As waves arrive from points out

of the plane of the image, the perceived wavelength of these waves is even larger than if these waves traveled coplanar to the imaging plane. This means that the focus size is now larger, due to these *trace* wavelengths.

Improving the resolution of an acoustic focus in air is most often limited by this second use of the diffraction limit, the incoming and outgoing waves interact and limit the resulting wave to the wavelengths of the incoming waves. The ability to image something is closely linked to the ability to focus waves with the same characteristics. If waves could be created that focused to a point in space with dimensions much smaller than a wavelength, then a source with subwavelength geometry could be imaged if the roles were reversed. In other words, reciprocity allows speaking of imaging and focusing with similar limitations and capabilities. The only difference is whether the object is a source or a focus and whether the far-field transducers are receiving or transmitting.

How is it then possible to overcome this diffraction limit and obtain subwavelength focusing? The only way this could be achieved is to violate one of the assumptions of the diffraction limit. One idea is to place objects (boundaries) near the imaging plane that modify the incoming waves and produce evanescent waves with subwavelength modulations.

Because acoustic waves respond to an impedance mismatch on the boundary between two media, the ratio of impedances can predict the behavior of the resulting wave. Scatterers have a relative impedance that is very large (e.g., from air to metal) or very small (e.g., from water to air). This mismatch causes strong scattering with the resulting wave being identical to the incoming wave but with possible attenuation and phase inversion. Resonators have a complex, frequency-dependent impedance. Thus, unlike a simple scatterer, the scattered wave has a frequency-dependent phase-shift relative to the incoming wave.

This phase shift can be described as an apparent change in the effective sound speed among a network of scatterers. As the wave interacts with a series of resonators, the phase is repeatedly shifted in a single direction. Because of the phase shifts, the resulting wave may look to be much slower or much faster than an undisturbed wave. When the phase looks like it is behind, it may appear that the speed of sound has decreased; and when the phase looks like it is ahead, it may appear that the speed of sound has increased. This effective sound speed is the *phase speed* of the wave. A lower phase speed results in a higher spatial frequency which in turn increases the focusing resolution of the wave.

Returning to the diffraction limit, if the *phase speed* among the resonators is used as the criterion, then no improvement in resolution occurs. Conversely, if the speed of sound in free space is used, then the diffraction limit is violated by having objects in the near field. Either way, subwavelength modulation using a resonant, near-field boundary is the method we have utilized to improve focusing resolution compared to focusing in free space.

1.1 Time Reversal Overview

Acoustic focusing is easily achieved using acoustic time reversal (TR). TR is a branch of wave physics that was developed in acoustics and has found many applications in this field [2, 3]. The TR process can be described as having four steps. First, a recording is made of an impulse (or another wideband signal). This first recording can be called the forward step. Second, the time-reversed impulse response (TRIR) is calculated by reversing an impulse response in time (or performing a cross-correlation between the source signal and the received signal). Third, if the transducers are not reversible, the positions of the sources and receivers are swapped. Fourth, the TRIR is broadcast into the system and generates a focus. This last step can

be called the backward or focusing step. Although the focusing happens at the end of the TRIR recording, it should be noted that performing a cross-correlation produces a two-sided signal consisting of a TRIR and an IR. In this case, the focus would occur at the center of the cross-correlation.

During the forward recording, some waves travel shorter routes and arrive quickly at the receiver while some waves travel longer paths and arrive later. The time of the waves is then a measure of the paths that the waves travel. When the recording is reversed, waves that travelled the longest paths are emitted first and more direct waves are emitted later. If the end of the TRIR recording is designated as focal time, then the waves with long routes are given more time to travel prior to focal time and the waves with short paths are given less time. As the TRIR propagates, the “first shall be last; and the last shall be first” [4], with the net effect that all waves arrive at the same time [5].

1.1.1 Reciprocal TR

The impulse response (IR) is a time record of waves transiting between two points. An IR is the recording made at one point due to an impulse generated at the other point. If the system does not change with time and there is no flow, the IR is the same regardless of which point makes the impulse and which one records the response. This reciprocity is often utilized in TR research to simplify the forward and backward steps of TR.

Practically, TR is often performed without reversible transducers. Thus, to broadcast the impulse response from the position of the receiver requires physically swapping the place of the sources and receivers. When reciprocity can be assumed, then the impulse that is recorded at the position of the receiver is the same IR that would be received if positions were swapped. Such a

system is invariant to the swapping of the transducers and the step of swapping the transducers can be skipped. This method of performing TR is sometimes called reciprocal TR since it depends on reciprocity [5].

1.1.2 Advantages of TR

Time reversal is closely related to beamforming. Beamforming could be described as a free-space version of TR. In free space, a measurement of the IR would simply yield an impulse that is time delayed by the distance between source and receiver. With several sources, measurements would produce the exact same time delays that would be calculated with a beamforming method. In contrast to beamforming, TR incorporates scattering and reflections and thus is robust in reverberant systems. In fact, using the principle of image sources, additional reflections in the system produce additional image sources [6]. Although these additional image sources are linked to the original source and thus do not create additional degrees of freedom, the additional angles can actually improve the aperture and therefore the focusing ability of TR process [7].

Like reflections, dispersion is handled well by TR [8]. Dispersion affects the wave speed as a function of the frequency, but the same TR methods can produce a focus. Indeed, time-reversing and broadcasting an IR smeared by dispersion produces a focus in the same way that time-reversing and broadcasting an IR smeared by reverberation (multiple scattering) produces a focus.

Time reversal also has the capability of focusing signals other than an impulse [9]. This can be accomplished by using the target signal in the forward step and not performing a cross-correlation but only time-reversing the signal response. Now this reversed signal response is sent into the system and the signal is recorded at the focal location. Alternately, the TRIR can be

convolved with the target signal. This result is then broadcast into the system and the target signal is focused at the focal location.

As the TRIR propagates through a reverberant environment, receivers at points along the path would typically only be able to measure an incoherent addition of the waves that are heading toward the focal location. This result means that TR could be used to communicate privately between two points if the environment was sufficiently reverberant as to produce an incoherent signal at every point other than the focal position [10].

1.1.3 Disadvantages of TR

The limitations of TR correlate with the assumptions described earlier: The system is linear, time invariant (or at least statistically time invariant), and there is no flow. Specifically, nonlinearities present in both steps would produce timing differences between the forward and backwards steps because the produced signal amplitudes are not the same, or there may be additional sources broadcasting in the backward step. These nonlinearities could be in the form of changes to the sound speed or changes to the attenuation. If the changes are small, it would be expected that the quality of the focus would degrade as waves are arriving at unintended times. However, if the timing of the focus is unimportant, these nonlinearities can produce a benefit [11]. In fact, creating nonlinearities at/near the focal location with otherwise linear broadcasts of TRIR signals may be the goal of the TR focusing [12].

Time-invariance is necessary as the forward and backward steps are separated in time. If the system is changing, then the quality of the focus degrades depending on the time between those two steps. This does not include a constant flow. When performing TR with a constant flow in

the medium, the constant flow must be reversed direction during the backward step [13]. If the flow cannot be reversed then the direction of propagation between the forward and backward steps must remain the same. In other words, reciprocal TR must be used.

1.2 Phononic Crystal

A *phononic crystal* is the acoustic analog to a *photonic crystal*. It indicates the acoustic properties of the material are due to some cell or crystalline structure. Originally described for their scattering ability, it has become clear that it is the resonances of the material that are key. TR has been used to explore subwavelength focusing when using arrays of resonators, though these studies were restricted to using only the direct sound in the IRs [14, 15, 16]. The phase speed in phononic crystals has also been explored using techniques other than TR [17, 18, 19].

1.3 Outline

The goal of this research is to use TR focusing as an analog for acoustic imaging and show that an array of acoustic resonators can improve focusing resolution in a reverberant environment. TR possesses the ability to focus waves in a phononic crystal because scattering and dispersion are compensated for in the normal TR process. For this reason, TR was chosen as the method to explore the ability to focus waves among arrays of resonators. First, we consider the case of a duct with many side-branch resonators. The spacing of the resonators is much less than a wavelength. Considering only propagating plane waves, when far away from the resonance frequency, the waves are unaffected by the resonators and continue down the duct. However, as the frequency of the incoming wave approaches the resonance frequency from

below, the resonators interact with the waves and the resulting phase speed is lower than the speed of sound.

Chapter 2 is an article published in the Journal of the Acoustical Society of America where this network of resonators was investigated using an equivalent circuit model. The model was used to explore the effect of quality factor on the amplitude and spatial extent of TR focus. The quality factor was modified by changing the geometry of individual resonators. This study found that lower quality factors allowed for a larger bandwidth of frequencies to be affected by the resonators. This larger bandwidth experienced smaller effective wavelengths than found in free space. Although the bandwidth was larger, the waves with frequencies closest to the resonance frequency of a single resonator still experienced far more of a change in wavelength. This larger bandwidth also meant that a larger bandwidth experienced scattering and the resulting amplitude was lower. The focus is only found over one resonator and the ability to focus between resonators is severely limited. For frequencies above the resonance of a single resonator, the resulting wave no longer oscillates spatially but instead exponentially decays. This decay lessens as the frequency continues to rise until the resulting wave is unperturbed by the side-branch resonators.

Chapter 3 describes the continued research of resonators in a duct but with a full-wave numerical simulation in COMSOL Multiphysics. This chapter constitutes a manuscript that was submitted and is currently under review. This model compares the numerical results to the equivalent circuit model. The simulations show strong coupling between the resonators as well as considerable attenuation of the waves as a result of the interaction with the resonators. The COMSOL model showed strong agreement with the findings from the computationally more efficient equivalent circuit model. This agreement was confirmed, in part, by producing a TRIR

using the equivalent circuit model and broadcasting that TRIR into the COMSOL model. The quality and timing of the focus are strong evidence that the equivalent circuit model accurately describes the pressure among the resonators. With the agreement between the COMSOL and equivalent circuit models, the simpler, less expensive, and faster modeling using equivalent circuits is desirable. The faster modeling also means it is much easier to conduct parameterization studies of other variables not already explored, such as the frequency of resonance and the spacing of the resonators. An experiment was also conducted with a single resonator using the 4" plane wave impedance tube at Brigham Young University. The phase shift described at the beginning of this chapter was observed and helps to understand the effective wavelengths getting smaller as the phase is shifted more.

Chapter 4 is an article published in the Proceedings of Meetings on Acoustics following a presentation given in May of 2022. The article outlines the LabVIEW software used for TR experiments at BYU called Easy Spectrum Time Reversal (ESTR). This software is a robust and comprehensive executable that was created by the author. Inspired by a user interface for similar software created at Los Alamos National Laboratory, ESTR presents an easy interface for undergraduate and graduate students studying TR. ESTR includes many options found in the acoustic TR research as well as the ability to include user-created MATLAB scripts to extend the capabilities of ESTR. The current version of ESTR represents years of development conducted concurrently with the research in this dissertation. ESTR can also control the 2-D scanning system at BYU. Thanks to John Ellsworth's upgrades, the 2-D scanning system is substantially more reliable and ESTR can perform repeatable, high-resolution scans and produce spatial pressure maps of TR focusing.

A version of ESTR with an alternate user-interface was also created for underwater experiments conducted at BYU [20]. The title of this version is Easy Spectrum Acoustic Underwater (ESAU). This version has the capability of interacting with multiple Spectrum systems as well as controlling two robotic arms from Universal Robotics for underwater spatial scans. The similarities in the software allow for interoperability of the ESTR/ESAU with the hardware at BYU.

As of October 2022, ESTR/ESAU has been used in several published works as well from the research in eight student theses/dissertations. As this author prepared for the next steps of research, Jay Clift, an undergraduate researcher, became involved in TR research and accepted the responsibility to maintain ESTR. After the author trained Jay to use ESTR and LabVIEW, maintenance of ESTR was passed to Jay. ESTR will continue to be a vital part of the TR research at BYU going forward. Future development is planned to include control of the Scanning Laser Doppler Vibrometer system within ESTR.

Chapter 5 describes a series of experiments conducted on a network of resonators using the software described in Chapter 4. This chapter is adapted from a manuscript that is being prepared for submission. This resonator array has not previously been studied in a 3-D environment. Successful attempts to produce focusing/imaging of complex geometry sources are shown. This work predicts the improved ability to image complex sources at a distance due to the presence of a resonant material in the near field of the sources. The experiments in this chapter use a method called the spatial inverse filter. An undergraduate researcher, Andrew Basham became involved in this phase of the research. Andrew became proficient at using ESTR and conducting spatial scans in the reverberation chamber. While the computation and processing were conducted by this author, the spatial scans were performed by Andrew.

Chapter 6 summarizes all the work done and points to additional work that is being actively explored. It also includes suggestions of future work that can be done.

Overall, this work shows physical explanations and a way of understanding the modulation of waves near arrays of resonators. This work presents a method for parameterization studies of resonator arrays and shows the results from some such studies. Results shown here describe the ability of focusing over an array of resonators in a reverberant space. Using the models in this dissertation, the quality of the focus can be explored, and more confidence can be obtained before modifying or fabricating a resonant material. Results show subwavelength resolution (as compared to free space) is obtainable when imaging sources above a resonant material even when the receivers are in the far field, even in a reverberant environment.

Chapter 2

Super-resolution within a one-dimensional phononic crystal of resonators using time reversal in an equivalent circuit model

An equivalent circuit model is able to accurately describe the acoustic propagation in a one-dimensional system. A simulation of an equivalent circuit model was used to predict the pressures inside a finite duct with anechoic terminations. This duct has evenly spaced Helmholtz resonators that contribute to a shortening of the wavelength not seen by any individual resonator. T. J. Ulrich is a researcher at Los Alamos National Laboratory and was involved in the formulation of this project and advised on the direction of the research. This chapter is an article published as A. D. Kingsley, B. E. Anderson, and T. J. Ulrich, "Super-resolution within a one-dimensional phononic crystal of resonators using time reversal in an equivalent circuit model," *J. Acoust. Soc. Am.* **152**(3), 2022 https://doi.org/10.1121/10.0013832. It is reprinted in this dissertation under the terms of ASA's Transfer of Copyright Agreement, item 3. I hereby confirm that the use of this article is compliant with all publishing agreements.

JASA ARTICLE

Super-resolution within a one-dimensional phononic crystal of resonators using time reversal in an equivalent circuit model

Adam D. Kingsley,[1] Brian E. Anderson,[1,a)] and T. J. Ulrich[2]
[1]*Acoustics Research Group, Department of Physics and Astronomy, Brigham Young University, Provo, Utah 84602, USA*
[2]*Los Alamos National Laboratory, Los Alamos, New Mexico 87545, USA*

ABSTRACT:
An equivalent circuit model has been developed to model a one-dimensional waveguide with many side-branch Helmholtz resonators. This waveguide constitutes a phononic crystal that has been shown to have decreased phase speed below the resonance frequency of an individual resonator. This decreased phase speed can be exploited to achieve super-resolution using broadband time reversal focusing techniques. It is shown that the equivalent circuit model is capable of quantifying this change in phase speed of the crystal and also the small-scale wave-resonator interactions within the crystal. The equivalent circuit model enables the parameterization of the physical variables and the optimization of the focusing bandwidth by balancing the combination of increasing resolution and decreasing amplitude near the resonance frequency. It is shown that the quality factor—in this case, the quality factor determined by the geometric shape of each resonator—controls the range of frequencies that are strongly affected by the Helmholtz resonators. © *2022 Acoustical Society of America*. https://doi.org/10.1121/10.0013832

(Received 12 April 2022; revised 13 July 2022; accepted 11 August 2022; published online 1 September 2022)
[Editor: Yun Jing] Pages: 1263–1271

I. INTRODUCTION

Time reversal (TR) is a signal processing method to obtain a focus of waves.[1–3] Originally called matched signal processing,[4,5] it combines an exploration step (forward step), where the impulse response is obtained, with a focusing step (backward step), which uses the time-reversed impulse response to generate a constructive interference of waves. First used in underwater acoustics, TR has found application in several fields, including seismology,[6] lithotripsy,[7] and nondestructive evaluation.[3]

TR has been used to localize acoustic sources. Applications include locating finger taps to use a solid media as a touch interface,[8] localizing the source of a gunshot in an urban environment,[9] and localizing and characterizing the great Sumatra earthquake.[10] These methods of localization require a backward step that is performed by modeling the environment, including scatterers, and numerically back propagating the impulse response signals from the receivers to find a point of maximum convergence. TR localization and imaging is well known to be limited by the diffraction limit, though if the finite size of imaged sources exceeds a half wavelength, then the true spatial extent is clouded by interference in focused waves.[11]

When focusing waves using TR, both direct and scattered waves simultaneously converge to a point in space creating a constructive focus that is diffraction-limited. Focusing to a spatial extent smaller than the diffraction limit is termed super-resolution. The diffraction limit has multiple useful definitions but typically constrains the spatial extent of the converging of waves to be no smaller than a half wavelength, $\lambda/2$.[12] The primary assumption of the diffraction limit given is that the focus must be in the far field of the source. Several examples exist where super-resolution was achieved in a modified system, several of which used TR. One example is of microwaves focusing among resonators.[13] In this work, the authors placed small antennae receivers among many resonating antennae. Similar work was also done with focusing acoustic waves among soda can resonators,[14] though later it was shown that TR was not necessary due to the regular arrangement.[15] Super-resolution has also been achieved experimentally by using absorbers[16] surrounding the focus as well as numerically[17] by simulating a similar region of absorption near the focus. Obtaining super-resolution with TR has also been demonstrated with near field amplification[18] and by using an active acoustic sink[19] as well as a passive acoustic sink.[20] Each of these examples was done with objects located within or information obtained within the near field.[21]

As described by Maznev *et al.*,[12] the diffraction limit cannot be broken. They assert that sub-diffraction-limited focusing is only possible when violating an assumption of the diffraction limit. A simple physical explanation is that the waves will conform to boundary conditions with perhaps higher spatial frequency than the wave contained elsewhere. Applying this additional restriction would mean that the diffraction limit requires that the focus not only must be in the far field of the source but also must be in the far field of any subwavelength objects. Focusing in a phononic crystal clearly violates this restriction, so although the diffraction limit is not being broken, according to this definition, the properties of the crystal allow for super-resolution focusing compared to waves outside the crystal.

a)Electronic mail: bea@byu.edu

The spatial extent of a TR focus in a one-dimensional (1-D) system is limited by principles like those in diffraction-limited systems. Although in the 1-D case, there is no aperture for diffraction to occur, the interference of direct and scattered waves creates a focal peak limited by the smallest wavelength. Because the measurement axis is the same as the propagation direction, there is no increase in measured wavelength due to oblique angles of approach.

Previous work in TR has shown that focusing near resonators or absorbers can produce a spatial focus much smaller than a wavelength. In this paper, a 1-D duct with periodic side-branch resonators is modeled that constitutes a phononic crystal.[22] This model has been studied in the context of transmission spectra,[23] band structure,[24] and the influence of detuned resonators.[25] However, previous studies[26,27] use an effective medium approach, and the resonators' effect is spread over the length of the duct. To predict the wave-focusing ability that TR offers in this system, it is essential to know the influence of resonator geometric properties as well as focus position relative to resonator position.[15] In essence, the equivalent circuit model allows characterization of the wave field within the crystal.

The purpose of this paper is to present an equivalent circuit model of focusing waves in a duct with many resonators, using TR. Typically, the TR process involves measuring an impulse response, $h_{A,B}$, between two points (A and B), reversing that impulse response (flipping it in time), and playing the reversed impulse response from one of the two points, which can result in focused energy at the other point.[1–3] Tanter *et al*. mention that TR focusing is equivalent to an autocorrelation of an impulse response.[28] More specifically, simulating TR in the time domain consists of obtaining $h_{A,B}$ and then performing an auto-correlation of $h_{A,B}$, thereby obtaining the temporal response ("focal signal") at point B due to broadcasting the time-reversed impulse response, $h_{A,B}(-t)$, from point A. Mathematically, this is calculated as

$$r_B(t) = h_{A,B}(-t) * h_{A,B}(t), \tag{1}$$

where r_B is the response of the signal at point B. When calculating the response at other locations (such as point C) due to the broadcast of $h_{A,B}(-t)$, the response becomes

$$r_C(t) = h_{A,B}(-t) * h_{A,C}, \tag{2}$$

where r_C is the response at point C while focusing occurs at point B. In the frequency domain, an auto-correlation is an auto-spectrum, and the cross correlation is a cross-spectrum. Thus, the temporal relations become spectral relations through a simple Fourier transformation,

$$h_{A,B}(t) * h_{A,B}(-t) \rightarrow H_{A,B}(\omega)H^*_{A,B}(\omega) \tag{3a}$$

and

$$h_{A,C}(t) * h_{A,B}(-t) \rightarrow H_{A,C}(\omega)H^*_{A,B}(\omega). \tag{3b}$$

Note that $*$ denotes a convolution, whereas * denotes a complex conjugation. A parametric study of the quality factor of the resonators and focusing position on the spatial extent and amplitude of waves in the duct is also presented. It is shown that the focusing bandwidth and resolution can be improved by using resonators with low absorption and a low quality factor. The model presented here enables a quick study of many other physical properties of interest. Note that continuous waves are employed here, which can be focused with TR even with single frequencies.[29]

Equivalent circuit, or lumped element, models have been used in acoustics[30] to study 1-D systems and the interaction of waves with side branches, changing cross section, and arbitrary impedances.[31–36] This model can only explore the plane wave propagation of waves in the duct, and consequently, side branches occur at discrete points along the duct rather than over an area. However, this simplified approach allows for faster numerical studies of physical parameters over a range of frequencies.

II. EQUIVALENT CIRCUIT MODEL

The equivalent circuit model utilizes electrical elements that represent lumped acoustic elements but also includes complex, frequency-dependent impedance elements to account for the phase changes of the wave as it propagates some distance. To model an infinite domain outside the region of resonators, anechoic terminations are added to both ends of the duct as resistors. An anechoic termination matches the characteristic acoustic impedance of the duct (with a resistance value of $\rho_0 c/S$), where ρ_0 is the density of air, c is the speed of sound, and S is the cross-sectional area of the duct. This impedance element simulates a semi-infinite duct. This element also eliminates the standing waves that would be created in a duct of finite length, which we want to avoid since the standing waves can overshadow the effects we are trying to study.

Sources can be added as side branches in the duct. The equivalent circuit represents the source by placing it in parallel with the anechoic termination. This implies that some of the energy radiated by the source propagates toward the network of resonators, and some directly propagates toward the anechoic termination. Loudspeakers can be modeled as constant current sources because their internal impedance is much higher than $\rho_0 c/S$. The source strength is chosen to be unity in the appropriate units as the resulting transfer function is ultimately the desired result of the model, and it does not depend on source strength (i.e., linear acoustic propagation is assumed).

Propagation through a duct segment of constant cross section is accomplished by use of the acoustic "T-network."[37] Three reactive, frequency-dependent elements placed in a T-shaped configuration model the proper evolution of the phase as the wave propagates through the circuit (see Fig. 1). The two elements on the horizontal branch of the T are each of value $(j\rho_0 c/S)\tan(kL/2)$, while the element on the vertical branch of the T has a value $-(j\rho_0 c/S)\csc(kL)$.

JASA
https://doi.org/10.1121/10.0013832

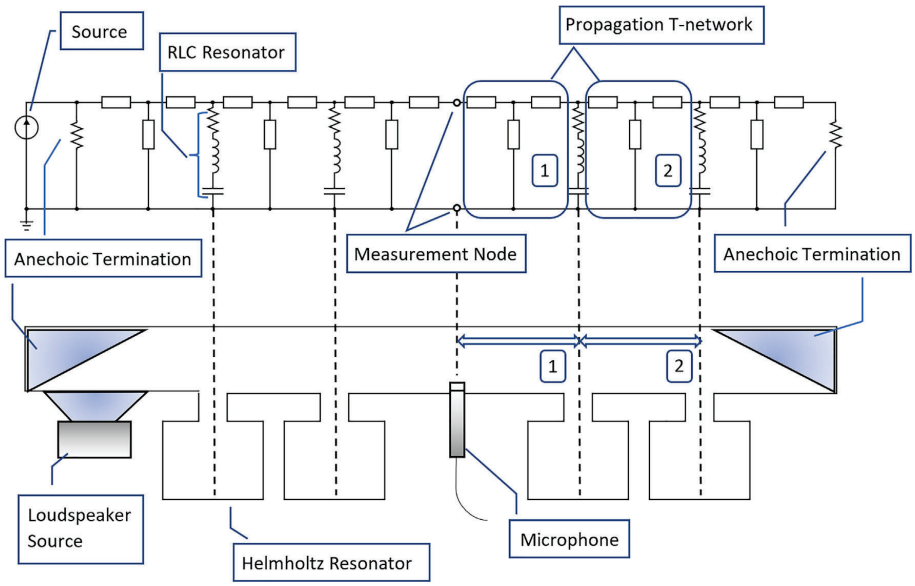

FIG. 1. (Color online) An equivalent circuit model of a waveguide with four side-branch resonators. The equivalent circuit (top) is shown with the corresponding acoustic system (bottom). Dashed lines represent the direct analog between domains. Solid (blue) triangles represent anechoic wedges in the acoustic domain and are modeled as purely resistive, impedance matched elements in the electrical domain. The loudspeaker source is modeled as a current source in the electrical domain. Two of the six "T-networks" for modeling propagation in the electrical domain (labeled [1] and [2]) match the portions of the waveguide that they represent.

Each T-network can span an arbitrary distance with respect to a wavelength of a constant cross section portion of the waveguide just by changing the single length, L, parameter (and by modeling the appropriate cross-sectional area). In this model, there is a T-network between the source and the first resonator and then a T-network between each resonator.

An acoustic resonator can be modeled using an equivalent electrical resonating circuit consisting of the series combination of a resistor, inductor, and capacitor, forming an "RLC circuit." The inductive element represents the mass-like inertia of the air in the neck that undergoes a lumped acceleration without compression. This acoustic mass has an equivalent inductance of $M_A = \rho_0 l/S$, where l is the length of the neck (including end corrections) and S is the cross-sectional area of the neck. The volume of the resonator below the neck can be considered a lumped compliance that undergoes compression but no acceleration. The volume is then represented as an equivalent capacitor with a capacitance of $C_A = V/(\rho_0 c^2)$, where V represents the volume of the resonator below the neck. Without any absorptive material in the resonator, the losses are due to thermoviscous effects[38] and can be represented by a resistor with an acoustic impedance value of $R_A = 2mc\alpha_w$, where m is the total acoustic mass of the neck and α_w is the absorption coefficient for wall losses.[39] For the dimensions of the system, the value of the acoustic resistance changes by only ~7% across the frequency band of interest; thus, we obtained a frequency-averaged value for these losses and used this single number value for R_A. The RLC circuit is naturally resonant in the same way the Helmholtz resonator has a single lumped-element resonance. The study presented in this paper uses Helmholtz resonators that always have a resonance frequency of 700 Hz. This frequency was arbitrarily chosen. We expect similar findings to occur for resonators having different frequencies of resonance.

In the assembled circuit, the only circuit nodes exist within the T-network (non-physical) and at the junctions with resonators and sources (see Fig. 1). For arbitrary spacing of measurement points at locations along the waveguide/duct between resonators, additional nodes must be introduced. Measurements of the wave field at locations along the waveguide can be done in the circuit through the introduction of a circuit node represented at the physical location of interest for a measurement. This is accomplished by splitting the T-network into a pair of T-networks that span the same physical distance as the original network. This produces a node between the networks at the measurement position. Calculating the electric potential (i.e., voltage) at the measurement point is equivalent to measuring the acoustic pressure at the physical point in space.

Figure 1 shows a simplified waveguide system with only four resonators in the lower half of the figure. The equivalent electrical circuit is shown above. Circuit elements depicted as boxes represent frequency-dependent impedances with values given previously. The RLC circuit

components are represented by classic electrical impedance equation forms for the electric analogs of those acoustic elements. The acoustic system shows a microphone measuring the pressure at a point in the waveguide where a node has been introduced in the model by splitting the T-network.

Iterating over a list of measurement points, each produces a unique circuit as each measurement point requires the insertion of a node. Using Kirchhoff's voltage law for loop analysis, the circuit can be formed into a system of equations. Each equation consists of the sum of potential drops over the elements in the loop due to the current in the loop as well as the current in the adjacent loops through shared loop elements. In matrix form, this linear system of equations can be represented as $Z\vec{I} = \vec{V}$, where Z is the matrix of impedance values (here representing acoustic impedances), $\vec{I}$ is the vector of unknown current values (here representing acoustic volume velocities), and $\vec{V}$ is the known net potentials (here representing acoustic pressures) for each loop. The resulting potentials in $\vec{V}$ will all be zero except for the loops that contain a source. Because the source is modeled as an ideal flow source and is in parallel with the anechoic termination, a Thevenin equivalent potential source was substituted that places the new potential source in series with the anechoic element.[40] This reduces the circuit by one loop and provides a known net voltage for that single loop. Solving for the unknown currents can then be done with a numeric linear solver. We used MATLAB's built-in linear solver, `mldivide`. Once the currents are calculated, the voltage at the measurement point can be calculated by finding the potential relative to ground. This is achieved by calculating the potential drop across the elements that lead to ground. To calculate the potential at the measurement node labeled in Fig. 1, the potential drop along the shortest path to ground is calculated. In the case of Fig. 1, that is two of the elements of propagation T-network [1], just downstream of the node. First the potential across the vertical element is calculated using the currents from the loops on both sides of that element, and then the potential across the left horizontal element is calculated using just the current in that loop. Summing the potential from both elements results in the complex acoustic pressure at that measurement point due to a single source. Solving the circuit at each frequency in the bandwidth provides the desired transfer function between the source and that single measurement point.

After obtaining the transfer function at each measurement point, the spatial extent of TR in the frequency domain is performed by choosing a focal location and calculating the cross-spectra of the transfer function of the target location with the transfer function of every measurement position.[41,42] The resulting set of cross-spectra describe the response at each measurement point when producing a focus at the focal location. Repeating the process for a source at each end and summing the results generated by each of the sources provide the spatial extent of the focus when both sources are active.

To conduct a parametric study of physical parameters, a model was chosen that would remain the same between studies except for the specific parameter to be varied. The model used represents a system with a 3 m long waveguide with a cross-sectional diameter of 10 cm. Cross-modes are not expected in this waveguide until frequencies greater than 2 kHz. A velocity source was added at each end of the duct with equal amplitudes. The resonator region consists of 51 side-branch resonators positioned every 2 cm in the central third of the waveguide from 1 to 2 m. The resonators have a resonance frequency that is held at 700 Hz. The spacing between resonators is 0.04λ (where λ is the wavelength of the resonance frequency) or 2 cm in this case. Measurements are made throughout the duct with a spacing of 0.0025λ or $\sim$1.2 mm by changing the length variable in the T-network circuit elements. A focus position was chosen to be equally distant between two resonators at 1.51 m (nearly equidistant between the sources). The bandwidth studied was 550–710 Hz.

Figure 2 shows the process of simulating TR focusing for a single source at a single frequency. Figures 2(a) and 2(b) show the magnitude and phase of the transfer function, H, between a source and the target focus position with a line marking 625 Hz. Figure 2(c) shows the relative response, $real(H)$, at every position within a duct at this same frequency of 625 Hz. Performing the cross-spectrum between the single value of H at 625 Hz and the response at all positions returns the response everywhere when focusing at this one frequency to this one position. Because Fig. 2 shows the normalized response, this is equivalent to a phase shift that produces a large response at the target focus position. This phase-shifted response is shown in Fig. 2(d). A movie showing the response as a function of phase shift is shown in Mm. 1. This process can be conducted at every frequency,

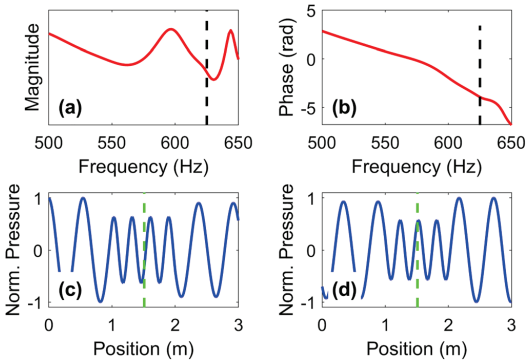

FIG. 2. (Color online) The process of simulating TR in the frequency domain. The magnitude and phase of the frequency response at a target focal location are shown in (a) and (b), with 625 Hz marked with a black, dashed line. The relative response (the real part of the response) throughout the duct is shown in (c). The conjugate of the response at the focal position is then multiplied by the complex response at every position to produce a focus at the target focal location (d).

https://doi.org/10.1121/10.0013832

and the results are summed to produce the response across the whole bandwidth.

Mm. 1. Movie illustrating the phase-shifting of a single frequency to make the source emission produce a positive peak at the focal location. This is a file of type "mp4" (0.8 MB).

In summary, each simulation includes the following steps:

(1) Create a circuit with impedance values calculated for a single frequency.
(2) Split a T-network into two T-networks to create a node where the response can be measured.
(3) Solve the circuit for the flow in every loop of the circuit.
(4) Calculate the potential at the spatial measurement point relative to ground using Ohm's law and the known flows and impedances.
(5) Repeat steps 2–4 for every spatial measurement point in the duct.
(6) Repeat steps 1–5 for every frequency in the bandwidth of interest.
(7) Calculate the cross-spectra between the frequency response at the target focal location and the frequency response at each spatial measurement point.
(8) Sum the real part of the cross-spectrum at each spatial measurement point.
(9) Repeat steps 1–8 for a second source on the other end of the duct.
(10) Superpose results from both sources.

III. RESULTS

In one dimension, the diffraction limit can be defined as the full width at half maximum (FWHM) of the highest frequency sine wave in the bandwidth. For a sine wave, the half maximum points occur at $kx = [\pi/6, 5\pi/6]$ or, equivalently, $x = [\lambda/12, 5\lambda/12]$. Thus, the FWHM of the pressure distribution of 1-D waves is $\lambda/3$. Figure 3 shows a representative TR focus within the waveguide composed of the focusing that occurs over a range of frequencies. The focus shows a FWHM of $\sim\lambda_{\min}/12$, or a fourfold improvement over focusing that would be obtained without the presence of the resonators. By inspecting individual frequencies in Fig. 2, the shortened wavelength components are visible within the resonator region. In the absence of resonators, the waves propagate with a free-space wavelength. Because the interaction of waves near the resonance frequency of a resonator leads to more reflection of those waves, the pressure amplitude drops within the phononic crystal. However, these strong interactions also result in a higher spatial frequency. TR focusing is defined as being at the location where the amplitude is the largest. In the case of Fig. 3(d), the amplitude is largest at the target focal location. However, the neighboring "sidelobe" peaks have significant amplitudes. The amplitude of the sidelobes is largely influenced by the limited bandwidth employed in the focusing, as would be expected from superposition and Fourier analysis. The use of a wider bandwidth reduces the amplitudes of the sidelobes relative to the focal amplitude. Known TR methods for reducing the amplitude of sidelobes include the idea of iterative TR (Ref. 14) and the inverse filter.[28] These methods typically achieve relative sidelobe amplitude reductions at the expense of a lower focal amplitude. In this paper, no additional methods have been applied, and the results use only the most basic TR process. It is important to note that it is more difficult to achieve lower sidelobe amplitudes in a 1-D medium, with only two sources, and using continuous wave TR.[29,43] The focus amplitude is larger because the spatial extent of the focusing at each frequency constructively interferes at that location due to the TR process.[29] Note that frequencies above the resonance frequency do not spatially oscillate and are heavily attenuated by the resonators, and although those frequencies do not contribute significantly to the focus, they do worse than the diffraction limit, resulting in less significant super-resolution (if they are included in the bandwidth).

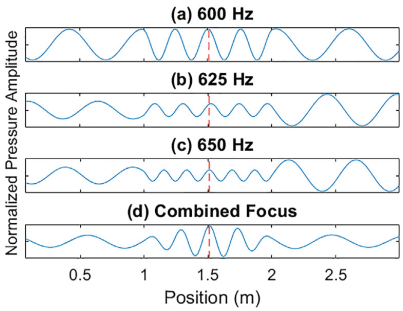

FIG. 3. (Color online) Focus over a uniform bandwidth of 600–650 Hz. Individual frequencies are shown [(a), (b), and (c)] as examples with the entire combined bandwidth shown on the right (d).

The focusing achieved at frequencies near resonance lends itself to an analysis of the effective wavelength of each frequency at the focal location. An effective wavelength, λ_{eff}, for each frequency component, f, of the focusing can be found by measuring the FWHM of the peak closest to the target focal location and setting the FWHM equal to $\lambda_{\text{eff}}/3$ (the FWHM of a sine wave in a 1-D system). This λ_{eff} can be larger or smaller than the free-space wavelength due to the interactions with the resonators. Using λ_{eff} and f, the phase speed of the wave can be calculated, $v = f\lambda_{\text{eff}}$.

Figure 4 shows the phase speed versus frequency for this example network of resonators. Below resonance, the phase speed is below the speed of sound in the model. In this model, the phase speed is below the speed of sound for all frequencies down to 47 Hz with a phase speed of 257 m/s, which is the lowest frequency that can be measured in the domain. Near resonance, the wave field is oscillating with a spatial frequency that matches the physical spacing of the resonators, though with very small amplitudes. However, immediately after crossing the resonance frequency, the wave ceases to spatially oscillate within the resonator

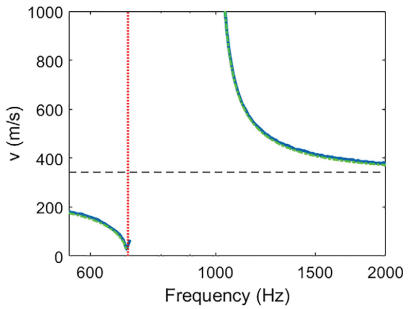

FIG. 4. (Color online) Comparing phase speed between equivalent circuit model and the effective medium approach used by Bradley (Ref. 26) as presented by Sugimoto *et al*. (Ref. 27). Solid blue line, calculated wave speed from the FWHM of the closest peak to the focus. Dotted-dashed green line, from the model presented by Sugimoto *et al*. Dashed black line, bulk wave speed in air. Dotted red line, resonance frequency of an individual resonator. A drop in phase speed is visible below resonance, and above resonance the wave eventually propagates and the phase speed drops to that of the speed of sound in air.

network, and instead the wave exponentially decays across the resonator network. Because the waves do not spatially oscillate in the resonator network, the effective wavelength is greater than the length of the resonator network. At higher frequencies, the acoustic waves do not interact strongly with the resonators, and once again, the signal propagates with effective wavelengths less than the length of resonator network, allowing for the phase speed to be measured. At even higher frequencies, the effective wavelengths eventually return to the normal, plane-propagation wavelengths, and the phase speed converges back to the speed of sound.

To validate the results from the equivalent circuit model, the dispersion relation given by Bradley[26] and later by Sugimoto and Horioka[27] is used to compute a phase speed for the physical system presented here. This phase speed is a large-scale effect of the phononic crystal, and the equivalent circuit model should result in the same phase speed while allowing for finer exploration of the focusing waves. The two systems being modeled are only different in the length of the phononic crystal. The effective medium models use an infinite crystal, but the equivalent circuit model requires a finite length to the phononic crystal. Representation of an infinite domain would require knowing the input impedance to a semi-infinite crystal and using that impedance as the termination on the finite domain. As shown in Fig. 4, the analytical model by Bradley[26] as presented by Sugimoto and Horioka[27] shows excellent agreement with the results from the equivalent circuit model. This agreement lends confidence to the equivalent circuit model approach to explain large- and small-scale interactions with the resonators.

IV. PARAMETRIC STUDY OF RESONATOR IMPEDANCE

Of the variables used to construct the model, perhaps the most conspicuous is that of the impedance of the resonators. In previous research utilizing phononic crystals of soda cans, the impact of the resonator shape (and, hence, its impedance or impact on quality factor) on the resolution improvement was not studied. If the frequency bandwidth of study is small compared to the resonance frequency and is close to the resonance frequency, f_0, the shape of the impedance curve of the resonators is governed by the mass and compliance of the resonator. The shape of a resonator's impedance curve is often described by the quality factor of the resonator. This acoustic quality factor, Q, incorporates three variables, namely, mass, compliance, and resistance,

$$Q = \frac{f_0}{f_u - f_l} = \frac{\omega_0 M_A}{R_A} = \frac{1}{R_A}\sqrt{\frac{M_A}{C_A}}, \tag{4}$$

where f_u and f_l are the half power frequencies above and below f_0, respectively, and $\omega_0 = 2\pi f_0 = (M_A C_A)^{-1/2}$ is the angular resonance frequency. Because of the dependence on resistance, the Q is frequently used to study the behavior of a resonator as the damping is changed. For our study, we keep the resistance as well as the resonance frequency the same. However, the values of mass and compliance can change (one going up while the other goes down proportionally) while maintaining the same resonance frequency, but the M_A/C_A ratio changes and, therefore, Q changes. Changing this ratio causes the resonance peak in the impedance magnitude to sharpen or broaden. A high Q leads to a sharp resonance peak, where a low Q leads to a broad resonance peak. It is important to note that although one is sharp and one is broad, if the resonance frequency and the resistance are kept constant, the values of the impedance minima will be the same (see Fig. 5). The pressure amplitude of the response of an individual resonator will also remain the same for a forced excitation.

The acoustic mass and compliance are constrained by physical necessity. One constraint that we used was to ensure that the acoustic mass and compliance must maintain the lumped-element characteristics of a Helmholtz resonator (though a higher order model for the resonator could have been used that would have modeled something like a quarter

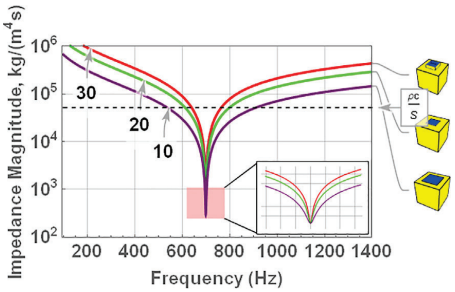

FIG. 5. (Color online) Impedance curves for three different shaped resonators. The quality factors of the resonators (going from top to bottom) are 30, 20, and 10. The acoustic impedance of a 4-in. diameter duct is also plotted as the dashed line. Resonance is 700 Hz. To increase visibility, the resonators shown are not scaled with size. Inset, impedance curves at resonance.

https://doi.org/10.1121/10.0013832

wavelength resonance and higher order modes along the resonator's length). This constraint means that every dimension of the neck and volume must be small compared to a wavelength so that no standing waves can form. To separate these regions and use the classical equations for resonance, it has been found[44] that the cross section of the neck must be less than ∼40% of the cross section of the volume.

A range of Q was calculated with the physical constraints that the neck must be strictly less than $\lambda/4$ and the cavity must have the largest dimension less than $\lambda/4$. The minimum neck length is also restricted as its physical length goes to zero and only the acoustic end corrections remain, and this provides a nonzero lower bound to the acoustic mass. As the neck gets longer, the acoustic mass increases, but so does the thermoviscous resistance. For the examples given, the Q was limited to a range of 10–30 (these values were determined for an individual resonator unattached to the waveguide). These resonators produce shapes like those found on the right side of Fig. 5.

Figure 5 shows that with the same resonance frequency, a lower Q results in a broader impedance curve near their minima. A resonator couples well to the acoustic waves if it has an impedance similar to that of the waveguide. A broader impedance curve results in more frequencies close to the impedance of the waveguide and stronger interactions with the resonators. Thus, a lower Q resonator will interact with the waves in the waveguide over a broader range of frequencies. It is similarly desirable to have a lower Q when using Helmholtz resonators for filtering acoustic waves.[38] A lower Q implies a smaller length neck, a large neck cross-sectional area, and a larger volume for the resonator.

Across the range of Q, competing priorities arise. Figure 6 shows that frequencies closer to the resonators' resonance frequency and resonators with a lower Q lead to a smaller effective wavelength. However, in Fig. 7, it is apparent that the amplitude of the focus is lower in these conditions. Although a broader resonance peak allows the resonator to influence a greater range of frequencies and thus provide a sharper focus (as shown by the effective

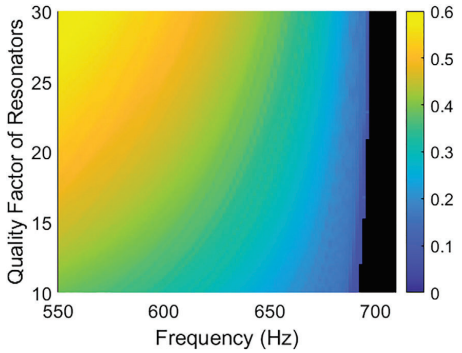

FIG. 6. (Color online) Fractional effective wavelength ($\lambda_{\text{eff}}/\lambda$) of waves among the resonators across a range of frequencies. Data omitted for undetermined effective wavelengths.

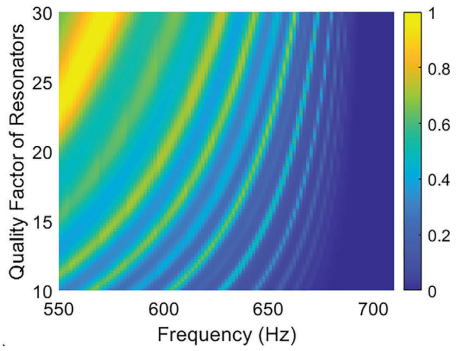

FIG. 7. (Color online) Amplitude of the focus across a range of quality factors and frequencies. The oscillations visible in the data are a result the maximum moving between resonators.

wavelength; Fig. 6), the amplitude of the focus also goes down (as shown by the focal amplitude; Fig. 7). These same competing priorities are found at every Q as the frequency approaches resonance; the overall peak amplitude goes down, but the spatial extent of the focusing also becomes narrower. Thus, there is a trade-off between the spatial resolution one may obtain and the amplitude of the focusing. It was also found, when using a finite bandwidth of frequencies, that the sidelobe amplitudes become more comparable to the focal amplitude as the frequencies in the bandwidth approach the resonators' resonance frequency.

The oscillations visible in the amplitude dependence displayed in Fig. 7 are a result of attempting to focus between two resonators. Each of the sources produces a maximum near the focal location, but the maximum is always over a nearby resonator. As the source frequency changes, the maximum may move between resonators. The ability for the two sources to be in phase at the focal location is not always guaranteed.

As mentioned in the Introduction, part of the advantage of using equivalent circuits is the ability to explore the discretization of the space. Maznev *et al*. previously found that for single frequency focusing, the peak amplitude was always over a resonator, whether the intended focus location was over a resonator or not.[15] The equivalent circuit model treats the intersection of the resonator and the duct as occurring at a single point in space. Although this intersection is not physical, this behavior of the focusing reported in the experimental findings by Maznev *et al*. is replicated in the equivalent circuit model. Figure 8 shows the peak amplitude at the intended target location of the focusing as the target focal location is moved across the locations of four of the resonators, including attempts to focus sound at many locations between the resonators. Also shown is the spatial extent of two representative foci at 1.48 m (nearly exactly between resonators) and 1.517 m (near, but not exactly at, a resonator). Focusing near a resonator produces a higher amplitude. In fact, focusing near a resonator can produce a higher amplitude focus at other points than an attempt to

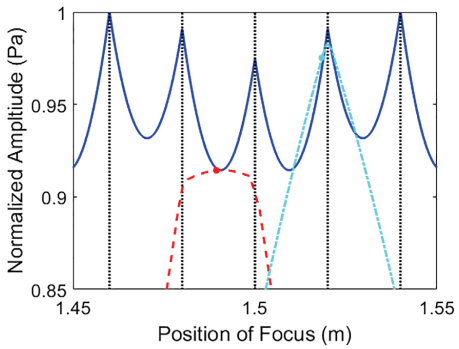

FIG. 8. (Color online) Amplitude of different foci as the target position is moved through a small range of positions near the middle of the set of resonators. The bandwidth is the same as in Fig. 3. Solid blue line, total amplitude at the focus location when TR is performed to focus a wave at that position. Dotted black lines, resonator positions. Red dashed line and cyan dotted-dashed line, spatial extent of the focus when focusing at 1.49 and 1.517 m, respectively. The focus location is marked with a dot.

focus at that point. This is shown in Fig. 8, where the (dotted-dashed cyan) focus occurring near the 1.52 m resonator produces amplitudes over an interval of 6.6 mm that are greater than an attempted focus at those positions. The resonators then are the target of the focusing, and reducing the spacing increases the focusing resolution. Thus, as stated by Maznev *et al*., no matter how small the FWHM may become, the space has been effectively discretized by the resonators, and the true resolution is that of the resonator spacing. It seems likely then that focusing between the resonators is simply a superposition of focusing at the adjacent resonators.

V. CONCLUSION

An equivalent circuit model has been presented that describes the behavior of waves in a phononic crystal with finite length and anechoic terminations. The model has been verified by comparing the phase speed to results from the literature. Effects among the resonators that have been previously observed in experiments have been observed in the equivalent circuit model. It has been shown that the presence of the resonators decreases the phase speed and leads to super-resolution when combined with TR focusing techniques. The quality factor of the resonators has been explored, and it has been shown that broadband focusing is more easily achieved with low quality factors when the resistance is kept constant. The trade-off between resolution and focal amplitude, and hence the quality of the focusing (here lower quality focusing means high sidelobe amplitudes relative to the focal amplitude), has also been explored, with frequencies near resonance yielding better spatial resolution but also contributing lower amplitude toward the focusing over a bandwidth of frequencies. This model can be used to explore other phononic crystal configurations in one dimension to obtain both phase speed behaviors and wave-resonator interactions.

This equivalent circuit model fits the analytical models as presented by Sugimoto *et al*. when looking at the effect of the medium on the large-scale parameter of phase speed. Although the methods of arriving at the phase speed are very different, the close agreement in the results shows that the equivalent circuit model can describe a crystal as if it were an effective medium. It also can be used to study waves within the crystal, and results match the small-scale effect of the focus snapping to an individual resonator as seen in the experimental results of Maznev *et al*. Although super-resolution has been shown, it has also been shown that the limiting resolution is the placement of the resonators, which serve as the effective measurement apparatus, with the resonators acting as individual pixels, and a focusing resolution below the spacing of the resonators is not possible.

The equivalent circuit model can describe large and small effects that are exhibited by a wave traversing a 1-D phononic crystal. This model has been used to parameterize some of the physical variables present in the model and has shown that the Q influences the bandwidth of contributing frequencies. This model has been shown to be useful for exploring this model and can describe other configurations. Previous work in phononic crystals has explored the influence of losses and alternating resonance frequencies on the absorption and phase speed of the waves.[25] This model could be used to explore additional and arbitrary complications in the configuration of resonators.

ACKNOWLEDGMENTS

Funding was provided by Los Alamos National Laboratory, Subcontract No. 527136, under the technology maturation program. Additional support was provided by the BYU College of Physical and Mathematical Sciences.

[1]M. Fink, "Time reversed acoustics," Phys. Today **50**(3), 34–40 (1997).
[2]B. E. Anderson, M. Griffa, C. Larmat, T. J. Ulrich, and P. A. Johnson, "Time reversal," Acoust. Today **4**(1), 5–16 (2008).
[3]B. E. Anderson, M. C. Remillieux, P.-Y. L. Bas, and T. J. Ulrich, "Time reversal techniques," in *Nonlinear Acoustic Techniques for Nondestructive Evaluation*, 1st ed., edited by T. Kundu (Acoustical Society of America, New York), pp. 547-581 (2018).
[4]A. Parvulescu and C. S. Clay, "Reproducibility of signal transmissions in the ocean," Radio Electron. Eng. **29**(4), 223–228 (1965).
[5]C. S. Clay and B. E. Anderson, "Matched signals: The beginnings of time reversal," Proc. Meet. Acoust. **12**(1), 055001 (2011).
[6]C. S. Larmat, R. A. Guyer, and P. A. Johnson, "Time-reversal methods in geophysics," Phys. Today **63**(8), 31–35 (2010).
[7]G. Montaldo, P. Roux, A. Derode, C. Negreira, and M. Fink, "Ultrasound shock wave generator with one-bit time reversal in a dispersive medium, application to lithotripsy," Appl. Phys. Lett. **80**, 897–899 (2002).
[8]R. K. Ing and N. Quieffin, "In solid localization of finger impacts using acoustic time-reversal process," Appl. Phys. Lett. **87**(20), 204104 (2005).
[9]S. Cheinet, L. Ehrhardt, and T. Broglin, "Impulse source localization in an urban environment: Time reversal versus time matching," J. Acoust. Soc. Am. **139**(1), 128–140 (2016).
[10]C. Larmat, J.-P. Montagner, M. Fink, Y. Capdeville, A. Tourin, and E. Clévédé, "Time-reversal imaging of seismic sources and application to the great Sumatra earthquake," Geophys. Res. Lett. **33**, L19312, https://doi.org/10.1029/2006GL026336 (2006).

[11]B. E. Anderson, M. Griffa, T. J. Ulrich, and P. A. Johnson, "Time reversal reconstruction of finite sized sources in elastic media," J. Acoust. Soc. Am. **130**(4), EL219–EL225 (2011).
[12]A. A. Maznev and O. B. Wright, "Upholding the diffraction limit in the focusing of light and sound," Wave Motion **68**, 182–189 (2017).
[13]G. Lerosey, J. de Rosny, A. Tourin, and M. Fink, "Focusing beyond the diffraction limit with far-field time reversal," Science **315**(5815), 1120–1122 (2007).
[14]F. Lemoult, M. Fink, and G. Lerosey, "Acoustic resonators for far-field control of sound on a subwavelength scale," Phys. Rev. Lett. **107**(6), 064301 (2011).
[15]A. A. Maznev, G. Gu, S. Y. Sun, J. Xu, Y. Shen, N. Fang, and S. Y. Zhang, "Extraordinary focusing of sound above a soda can array without time reversal," New J. Phys. **17**, 042001 (2015).
[16]G. Ma, X. Fan, F. Ma, J. de Rosny, P. Sheng, and M. Fink, "Towards anti-causal Green's function for three-dimensional sub-diffraction focusing," Nat. Phys. **14**(6), 608–612 (2018).
[17]A. Mimani, "A point-like enhanced resolution of experimental Aeolian tone using an iterative point-time-reversal-sponge-layer damping technique," Mech. Syst. Signal Process. **151**, 107411 (2021).
[18]S. G. Conti, P. Roux, and W. A. Kuperman, "Near-field time-reversal amplification," J. Acoust. Soc. Am. **121**(6), 3602–3606 (2007).
[19]J. de Rosny and M. Fink, "Overcoming the diffraction limit in wave physics using a time-reversal mirror and a novel acoustic sink," Phys. Rev. Lett. **89**(12), 124301 (2002).
[20]F. Ma, J. Chen, J. Wu, and H. Jia, "Realizing broadband sub-wavelength focusing and a high intensity enhancement with a space-time synergetic modulated acoustic prison," J. Mater. Chem. C **8**, 9511–9519 (2020).
[21]F. Ma, Z. Huang, C. Liu, and J. H. Wu, "Acoustic focusing and imaging via phononic crystal and acoustic metamaterials," J. Appl. Phys. **131**, 011103 (2022).
[22]M.-H. Lu, L. Feng, and Y.-F. Chen, "Phononic crystals and acoustic metamaterials," Mat. Today **12**(12), 34–42 (2009).
[23]X. Wang and C. M. Mak, "Acoustic performance of a duct loaded with identical resonators," J. Acoust. Soc. Am. **131**(4), EL316–EL322 (2012).
[24]Z. G. Wang, S. H. Lee, C. K. Kim, C. M. Park, K. Nahm, and S. A. Nikitov, "Acoustic wave propagation in one-dimensional phononic crystals containing Helmholtz resonators," J. Appl. Phys. **103**(6), 064907 (2008).
[25]J. Guo, J. Cao, Y. Xiao, H. Shen, and J. Wen, "Interplay of local resonances and Bragg band gaps in acoustic waveguides with periodic detuned resonators," Phys. Lett. A **384**(13), 126253 (2020).
[26]C. E. Bradley, "Acoustic Bloch wave propagation in a periodic waveguide," Technical report of Applied Research Laboratories, ARL-TR- 91-19 (July), University of Texas, Austin, TX, 1991.
[27]N. Sugimoto and T. Horioka, "Dispersion characteristics of sound waves in a tunnel with an array of Helmholtz resonators," J. Acoust. Soc. Am. **97**(3), 1446–1459 (1995).
[28]M. Tanter, J. Thomas, and M. Fink, "Time reversal and the inverse filter," J. Acoust. Soc. Am. **108**(1), 223–234 (2000).
[29]B. E. Anderson, R. A. Guyer, T. J. Ulrich, and P. A. Johnson, "Time reversal of continuous-wave, steady-state signals in elastic media," Appl. Phys. Lett. **94**(11), 111908 (2009).
[30]G. Bertuccio, "On the physical origin of the electro-mechano-acoustical analogy," J. Acoust. Soc. Am. **151**(3), 2066–2076 (2022).
[31]B. B. Bauer, "Equivalent circuit analysis of mechano-acoustic structures," Trans. IRE Prof. Group Audio **AU-2**(4), 112–120 (1954).
[32]B. E. Anderson, C. B. Hilton, and F. Giorgini, "Equivalent circuit modeling and vibrometry measurements of the Nigerian-origin Udu Utar drum," J. Acoust. Soc. Am. **133**(3), 1718–1726 (2013).
[33]C. B. Goates, M. F. Calton, S. D. Sommerfeldt, and D. C. Copley, "Modeling acoustic resonators using higher-order equivalent circuits," Noise Control Eng. J. **67**(6), 456–466 (2019).
[34]S. Pyo and Y. Roh, "Structural design of an acoustic planar array transducer by using the equivalent circuit method," Ultrasonics **108**, 106219 (2020).
[35]B. E. Anderson and S. D. Sommerfeldt, "Solving one-dimensional acoustic systems using the impedance translation theorem and equivalent circuits: A graduate level homework assignment," J. Acoust. Soc. Am. **150**(6), 4155–4165 (2021).
[36]E. Brandão, W. D. Fonseca, and P. H. Mareze, "An algorithmic approach to electroacoustical analogies," J. Acoust. Soc. Am. **152**(1), 667–678 (2022).
[37]W. P. Mason, *Electromechanical Transducers and Wave Filters* (Van Nostrand, New York, 1942), pp. 204–205.
[38]U. Ingard, "On the theory and design of acoustic resonators," J. Acoust. Soc. Am. **25**(6), 1037–1061 (1953).
[39]L. E. Kinsler, A. R. Frey, A. B. Coppens, and J. V. Sanders, *Fundamentals of Acoustics*, 4th ed. (Wiley, New York, 2000), pp. 284–286.
[40]H. von Helmholtz, "Ueber einige Gesetze der Vertheilung elektrischer Ströme in körperlichen Leitern mit Anwendung auf die thierisch-elektrischen Versuche" ("Some laws concerning distribution electrical currents conductors with applications to experiments animal electricity"), Ann. Phys. Chem. **165**(6), 211–233 (1853).
[41]M. H. Denison and B. E. Anderson, "Time reversal acoustics applied to rooms of various reverberation times," J. Acoust. Soc. Am. **144**(6), 3055–3066 (2018).
[42]J. V. Candy, A. J. Poggio, D. H. Chambers, B. L. Guidry, C. L. Robbins, and C. A. Kent, "Multichannel time-reversal processing for acoustic communications in a highly reverberant environment," J. Acoust. Soc. Am. **118**, 2339–2354 (2005).
[43]S. Yon, M. Tanter, and M. Fink, "Sound focusing in rooms: The time-reversal approach," J. Acoust. Soc. Am. **113**(3), 1533–1543 (2003).
[44]R. L. Panton and J. M. Miller, "Resonant frequencies of cylindrical Helmholtz resonators," J. Acoust. Soc. Am. **57**(6), 1533–1535 (1975).

Chapter 3

Time reversal in a 1D phononic crystal using finite-element modeling and an equivalent circuit model

A phononic crystal acts as a dispersive medium with a phase speed that is much lower than the bulk wave speed at frequencies below the resonance of a single resonator. Time reversal is used to compensate for the phase shifts caused by individual resonators as the waves enter the medium and enables focusing of acoustic waves among the crystal. An equivalent circuit model is shown that can predict the dispersion and attenuation of the crystal and is compared in both frequency and time to a full wave finite-element simulation of a duct with periodic side-branch resonators. The phase shift due to a single resonator is also shown. This chapter has been submitted as a manuscript and has been accepted for publication in the Journal of the Acoustical Society of America as an Express Letter and it is now in press. I hereby confirm that the use of this article is compliant with all publishing agreements.

3.1 Introduction

Acoustic Time Reversal (TR) is a method used to exploit multiple scattering to create a focus of waves [3]. Originally utilized for underwater communication [21, 2], TR has found application for focusing and imaging waves among metamaterials [16], phononic crystals [15],

and complex media [22]. Physically, TR enables using the full impulse response of a system, including the reverberation caused by multiple scattering, to obtain converging waves at a target focal position. The time reversal of the impulse response aligns the phase of direct and scattered waves to create a coherent wavefront [5].

In this chapter, a duct with periodic side-branch resonators is studied using a finite-element simulation as well as an equivalent circuit model. This duct and resonator system constitutes a classical, one-dimensional phononic crystal. Metamaterials like this have been studied extensively for their ability to manipulate phase speed and other properties. Phononic crystals has been studied specifically for its band structure properties, however, this 1-D phononic crystal exhibits interesting properties below the bandgap. Similarly, below the resonance frequency of a single resonator in the crystal, this system significantly decreases the phase speed among the resonators. Previous studies have treated this arrangement as an equivalent material and proceed to average the resonator properties over the length of the duct [17, 18]. However, when focusing acoustic waves among the resonators, the local effects of resonators are important [19]. This chapter shows numerical simulation results for both frequency and time domain simulations of TR focusing within the duct. Sub-diffraction limited focusing is apparent when compared to the bulk wave speed in air.

These full-wave simulations are compared to a less computationally expensive method based on an equivalent circuit model [23]. Simulated focusing is compared between the circuit model and the finite-element simulations. In addition, the impulse response results from the circuit model are used to produce focusing in the simulation. This approach shows that the equivalent circuit model can simulate a focus that is in close agreement with the focus obtained in a full-wave simulation. A difference is visible when inspecting the spatial results on a small

scale: Where the equivalent circuit model produces non-differentiable points in the pressure when over a resonator, the finite-element results are smooth. This difference is explained by the difference in modeling of junctions between the resonators and the main duct. The equivalent circuit model can only model junctions (resonator necks) of zero width whereas the finite-element model has finite spatial extent resonator openings, and as such the interaction between the resonators and the duct is spread over the necks' area.

3.2 Model

The primary model studied consists of a 3 m duct with a diameter of 5 cm and 51 resonators positioned in the central third of duct. Both ends of the duct were modeled as anechoic, and the left end of the model included a pressure source. A Helmholtz resonator was modeled that produced a notch in the downstream pressure at 700 Hz. The neck forms a curved junction with the cylindrical duct and has a length of 0.0232 m, measured along the shortest side. The ratio of the cross-sectional area of the neck compared to the widest area of the volume is kept at 20%. The radius of the neck is 0.0106 m, and the volume of the resonator cavity was 5.5E-5 m^3. Resonators were positioned every 2 cm axially and 80º angularly between each adjacent resonator so that the desired resonator density could be achieved as shown in Fig. 3.1.

3.2.1 COMSOL Model

The finite-element simulations were conducted using COMSOL Multiphysics® (COMSOL Inc., Version 5.6) using the *Pressure Acoustics* interfaces and specifically either the *Frequency Domain* interface which solves the Helmholtz equation or the *Transient* interface which solves

the wave equation. The ends of the duct were modeled as anechoic with the *plane wave radiation* boundary condition which uses an impedance matching condition and assumes the cross-section of the wave has constant phase. Additionally, an *incident pressure field* was added to the model at the ends which models a pressure source. All other boundaries were modeled as rigid. The simulation in the frequency domain used a range of frequencies from 500 to 700 Hz in steps of 1 Hz. The simulation in the time domain used a fixed sampling frequency of 42 kHz in order to resolve the maximum frequency of 700 Hz. The simulation results was saved every 0.1 ms for the length of the 0.21 s simulation.

The mesh for this model required many more elements than would be expected considering the smallest free-space wavelength. Because the resonators modulate the field on a scale comparable to their size, the duct was meshed so that several points existed over the opening of a single resonator. The central section of the duct was also meshed with a finer mesh so that axial pressures could be explored with even finer detail as shown in Fig. 3.1. Specifically, this mesh provided over 1200 spatial sampling points along the 3 m of the axis.

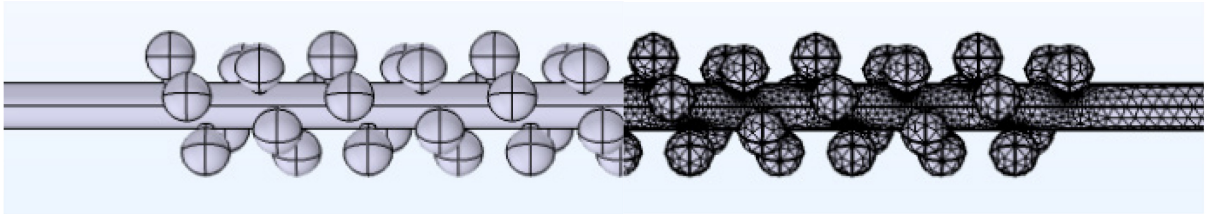

Figure 3.1 A composite image showing a portion of the COMSOL model on the left half and a portion of the generated mesh on the right. The portions of the duct not shown are straight-pipe continuations of the duct and possess a similar mesh.

3.2.2 Equivalent Circuit Model

An equivalent circuit model may incorporate lumped and waveguide elements that account for the flows and potentials to solve for physical variables in the system. The methods for creating this system using an equivalent circuit model were extensively described previously [23] and are summarized here. The equivalent circuit elements include a volume velocity source modeled as an ideal AC flow source, an anechoic termination as a resistor with a resistance equal to the characteristic acoustic impedance of $\rho_0 c/S$, and each resonator as a series LC circuit (series RLC if thermoviscous losses are present). Wave propagation between physical elements utilizes an equivalent T-network of frequency-dependent reactive elements. The upper two elements on the horizontal branch of the T-network have an impedance value of $j\,\rho_0 c/S \tan(kL/2)$, and the vertical branch element of the T-network has a value of $-j\,\rho_0 c/S \csc(kL)$, where ρ_0 is the mass density, c is the speed of sound, S is the cross-sectional area, k is the wavenumber, and L is the length of the duct that the T-network represents. These T-networks connect all the various elements, but an extra T-network is also inserted to create a node in the circuit where the potential can be measured. The potential represents the axial pressure in the duct at that location between the T-networks.

The solution to the equivalent circuit is then mathematically constructed in this case by using Kirchhoff's voltage law for each loop of the circuit to generate a system of equations. Thévenin's theorem was employed to generate an equivalent circuit with only potential sources. Then the system of equations is solved by using MATLAB (Mathworks 2022a) and the suite of functions represented by the mldivide (matrix left divide) function [24]. The resulting currents (flows) can then be used to solve for the potential, and thus the pressure, at any node. This

method of solving for the pressure is then repeated for each measurement position to obtain the response along the duct for a single frequency. The frequency is then incremented, and the whole process is repeated to obtain the axial response at the new frequency. This process continues until the entire spectrum is obtained for each measurement position along the length of the duct.

3.2.3 Quality Factor

The finite-element model was used to calculate the quality factor, Q, of any resonant mode using an eigenfrequency analysis and the relation between eigenfrequency and Q:

$$Q = \frac{|\lambda|}{2\lambda_{\text{imag}}}, \tag{3.1}$$

where $|\lambda|$ is the magnitude of the complex eigenvalue and λ_{imag} is the imaginary part of the eigenvalue. To measure this quality factor for an individual resonator, a resonator was placed in a circular baffle with a radial extent of more than one wavelength and a spherical radiation condition was placed on the resulting hemispherical boundary. The domain consists of the hemispherical space between the circular baffle and the hemispherical boundary. An eigenfrequency analysis together with Eq. (3.1), returned a Q of 52.6. This value was compared to a bandwidth calculation using a *Frequency Domain* simulation. Specifically, the squared pressure spectrum inside the resonator was used to calculate the Q using

$$Q = \frac{f_{\text{res}}}{\Delta f}, \tag{3.2}$$

where f_{res} is the resonance frequency and Δf is the bandwidth of the squared response using the full width at half-maximum (FWHM). The method returned a value of 52.4, in agreement with COMSOL's eigenfrequency analysis result.

The Q of the resonator was also calculated from the common lumped-element model of a resonator, and the typical corresponding equation for the Q of a simple resonator:

$$Q = \frac{\omega_0 m}{R}, \tag{3.3}$$

where ω_0 is the natural angular frequency of the resonator, m is the acoustic mass of the resonator, and R is the total losses of the resonator through radiation and thermoviscous losses. For the models used here, no thermoviscous losses were included and the acoustic resistance consisted entirely of radiative losses of the resonator through its opening. This radiation resistance was calculated using Eq. (10.8.9) from Kinsler *et al.* [25],

$$R_{\mathrm{rad}} = \frac{\rho_0 \omega_0^2}{2\pi c}, \tag{3.4}$$

where ρ_0 is the density of air, c is the speed of sound in air, and ω_0 is the same as in Eq. (3.3). The acoustic mass, m, is calculated using

$$m = \rho_0 L/S, \tag{3.5}$$

where ρ_0 is the density of air, L is the effective length of the neck, and S is the cross-sectional area of the neck. The effective length was calculated as the physical length of the neck in addition to an end correction for both the baffled and cavity ends. The baffled end correction of $0.82a$, comes from the work of Kergomard and Garcia [26] as well as others [27]. The cavity end correction of $0.68a$, comes from the work of Dalmont *et al* [28]. In these corrections, a is the radius of the neck. Using these calculations, the resonator has a Q of 54.7, a 4% difference from the finite-element model results of 52.6. Although these values showed good agreement, many numerical and analytical investigations of the end correction for the cavity end of the neck produce very different values [29, 30, 31, 32].

When these same resonators are connected to a duct instead of a large baffle, the Q value changes considerably. With the resonator connected to a cylindrical duct with a diameter of 5 cm, instead of a circular baffle, an eigenvalue analysis returns a Q of 5.1 using Eq. 3.1 and a *Frequency Domain* simulation returns 5.0 using Eq. 3.2. The lumped-element model of the Helmholtz resonator is the same as in Eq. (3.3), except that the duct end has an end correction of $0.67a$ from the work of Ji [33]. The equations given by Ji considered only necks that were sufficiently long such that all cross-modes would be expected to decay. However, in this work, the neck is only ~1 diameter long and there may be a significant contribution of the cross-modes not taken into consideration when using this lumped-element model of the resonator. An equivalent circuit model of a resonator connected to a duct, instead of a large baffle, gives a Q of 17.7 using Eq. (3.2). This large discrepancy shows that the lumped-element model of the resonator (and thus the equivalent circuit model) does not have as strong a response to a change in the duct impedance as does the finite-element model.

3.2.4 Simulating Time Reversal Focusing

In this chapter, TR is used as a tool for focusing sound waves among the network of resonators. Spatial focusing of waves is analogous to imaging resolution in the reciprocal case. TR focusing requires obtaining the impulse response (IR) to a desired focal location. By broadcasting the time-reversed impulse response (TRIR), the system produces a focused impulse at the focal location. The mathematical explanation is that as the emissions of the TRIR travel through the room, it is equivalent to convolving the TRIR with the IR of each point in the room which produces a maximum response at the focal location. When simulating this interaction to obtain a spatial response, it is necessary to know the impulse response between the source and each measurement point in the system. Then cross-correlations reveal the response at every measurement position with an autocorrelation occurring at the focal location [34]. When simulating this in the frequency domain, instead of impulse responses, transfer functions are measured, and instead of cross-correlation operations, cross-spectral operations show the resulting frequency response. If the spatial response is desired, then the real part of the frequency response can be extracted to show the relative response at each position for a given frequency at a point in time. All the responses can then be summed to show the result over a range of frequencies.

In the same way, an equivalent circuit model can create a transfer function to each point within the duct and simulate the spatial extent of the focusing. This chapter also shows the results when the transfer function from the equivalent circuit model is used to generate focusing in a finite-element time-domain simulation. This coupling of models helps to further validate the ability of the circuit model to accurately reconstruct the interaction of the waves with the resonators.

3.3 Results

Using this resonator design within the phononic crystal described earlier, a series of TR simulations were conducted to focus waves to nearly the center of the crystal ($x = 1.51$ m). Using a finite-element simulation in the frequency domain, the response was measured along the axis of the duct. The transfer function, *H*, was calculated as the complex response at each point along the axis due to the source. The cross-spectra were calculated using the *H* from the source to the target focal location ($x = 1.51$ m) and the *H* from the source to each measurement point along the axis. Then the real part of each cross-spectra was extracted and summed to produce the total response at a point in space. The collection of responses at each point in space provides the spatial extent of the simulated focus.

The same process was performed with the equivalent circuit model and a spatial focus was obtained. Lastly, an inverse Fourier transform was performed on the transfer function from the equivalent circuit model and the resulting TRIR was broadcast into a *Transient* COMSOL simulation producing another focus resulting from a hybrid combination of these two models. These three results are shown in Fig. 3.2.

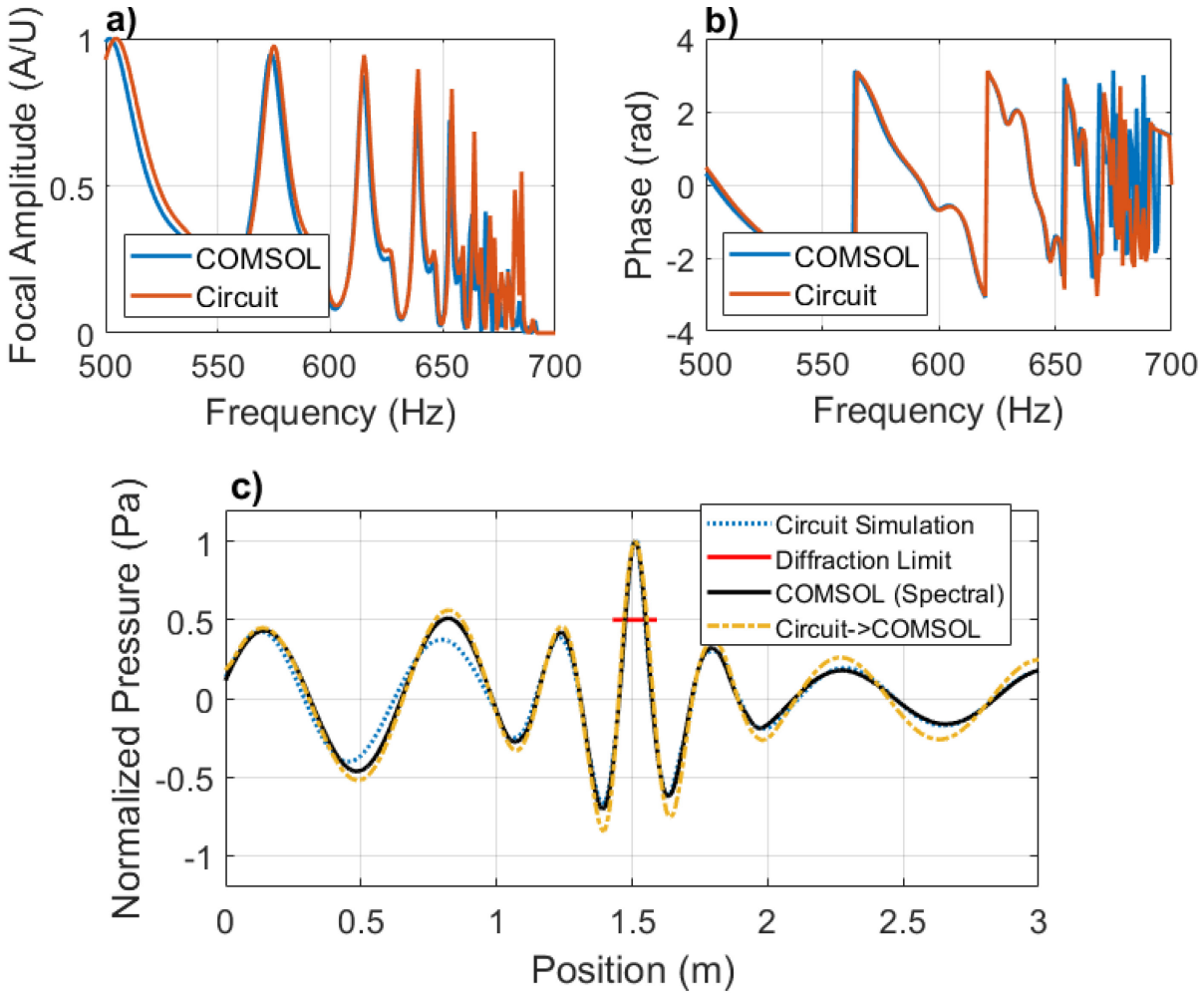

Figure 3.2 Finite-element simulations and equivalent circuit model comparisons for a focus at 1.51 m along the length of the duct with the mesh shown in Fig. 3.1. Amplitude and phase for the transfer function are shown in (a) and (b). Spatial extent of the focus is also shown in (c) for simulations from the circuit model, the *Frequency Domain* simulation, and the *Transient* simulation using the transfer function from the equivalent circuit model. The diffraction limit is also shown using the FWHM of a sine wave at the resonance of a single resonator (700 Hz).

Close agreement is observed in Fig. 3.2 for both the magnitude and phase of the transfer functions obtained through the equivalent circuit model and the finite-element model for frequencies below ~670 Hz. The magnitude of the transfer function obtained from finite-element model drops off above this frequency and although the error in phase increases, the lower amplitude means that these errors do not have a strong effect on the focus. The close agreement

between models for the spatial distribution of the focus validates the equivalent circuit model as being able to simulate focusing in this phononic crystal for this configuration.

3.4 Physical Insights

The phononic crystal studied here is comprised of resonators. An individual Helmholtz resonator is commonly used to filter acoustic waves. The lower phase speed induced by a collection of resonators can be seen as phase shifts imposed by individual resonators. Waves below resonance experience a phase lag as they pass an individual resonator, whereas waves above resonance experience a phase advance. The cumulative effect of many resonators can be described as a decrease or an increase to the phase speed [17, 18]. The following simulations as well as an experiment were conducted to measure this phase shift.

Simulations were conducted with and without losses in both a *Frequency Domain* simulation as well as an equivalent circuit model. The equivalent circuit model used Kinsler *et al.* [25], Eq. (10.8.10) for the losses in the resonator, which produced more damping than is visible in the experimental results. A *Frequency Domain* simulation utilized the thermoviscous losses model in the neck of the resonator and an accompanying finer mesh near the boundary in the neck.

An experiment was conducted in an impedance tube with anechoic terminations with a single side-branch resonator with a resonance frequency of 100 Hz. Two measurements were made using a synchronous output/input acquisition system [34] in the case with and without the resonator. A linear chirp was broadcast from one end of the duct and after passing the Helmholtz resonator, the response was measured by a microphone. A cross-correlation of the chirp response with the chirp produced the impulse response. The transfer function was calculated using the

Fourier transform of the impulse response. Using the cases with and without the resonator, the difference in phase was calculated. A time shift was then calculated by dividing the phase shift by the angular frequency. This time shift represents the lag or advance because of the acoustic wave interacting with the resonator.

The experimental results as well as the results of an equivalent circuit model of this setup are shown in Fig. 3.3. Simulations and experiment show a delay below resonance and an advance above resonance. By adding damping, the simulations are better able to match the smooth transition around resonance. The terminations in the impedance tube are expected to be anechoic down to ~95 Hz, which may be the reason for the asymmetry in the experimental results below resonance.

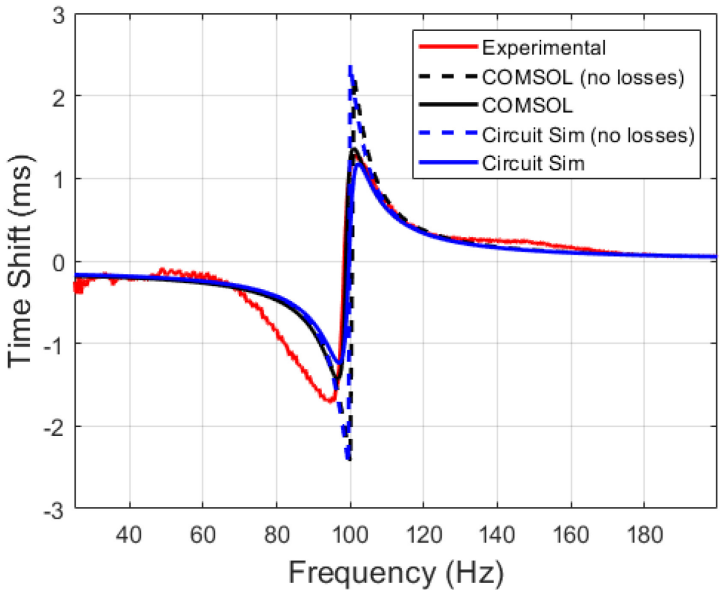

Figure 3.3 The time shift of each frequency downstream of a side-branch Helmholtz resonator with a resonance frequency of 100 Hz is shown. Equivalent circuit simulations as well as finite-element simulations are shown with and without losses. Experimental results are also shown.

This advance and lag can be seen spatially using a *Transient* simulation as shown in Fig. 3.4. Two domains were created with one having a side-branch resonator with a resonance frequency

of 700 Hz. A single-frequency tone is played into the ducts from the left at a frequency below or above resonance and green-colored isosurfaces are plotted to show the zero pressure planes of the wave as they move through the duct. The downstream phase is visible as the relative position of these isosurfaces (see Fig. 3.4).

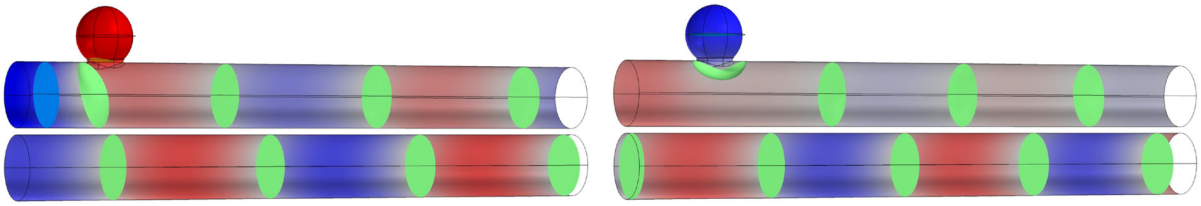

Figure 3.4 The pressure in a duct below (above) resonance on the left (right). Phase delay/advance is seen by the relative positions of the isosurfaces that propagate downstream and to the right of the resonator. Red represents high positive pressure and blue represents high negative pressure with green representing zero.

Although the phase delay due to a single resonator is insufficient to explain subwavelength focusing possible among many resonators, the cumulative effect of many resonators is to slow the phase speed in the same way that a single resonator delays the phase of a single frequency below resonance. The advance in the phase above resonance can also be seen as the reason that waves above resonance have a much higher phase speed. When the phase speeds are the highest, the wave appears to be in-phase everywhere and does not spatially oscillate.

3.5 Conclusion

It has been shown that TR focusing is able to construct sub-diffraction limited focusing within a phononic crystal made up of side-branch resonators. This has been explored in a full-wave, 3-D simulation of a 1-D phononic crystal. This sub-diffraction limited focusing occurs only when the spatial extent of the focusing is compared to the bulk wave speed in air rather than

using the phase speed in the phononic crystal to determine the diffraction limit. An equivalent circuit model has been shown to be capable of predicting the transfer function to a focal position within this finite-length crystal and is thus suitable for predicting the phase speed within the crystal with much less computational resources.

The effect of a single resonator on the phase of the downstream wave has been shown using experimental results (see Fig. 3.3). The resulting phase shift was shown to be simulated well by a finite-element, frequency-domain simulation as well as an equivalent circuit model. Animations were created to show this phase shift. When thermoviscous damping was added, the numerical results produced very close agreement between the three methods. This effect of a single resonator provides some intuition about the behavior that many resonators have on the phase speed of the resulting wave.

Chapter 4

Development of software for performing acoustic time reversal experiments

The experimental validation of this research necessitates the automation of conducting time reversal experiments. Hardware for conducting experiments consists of a Spectrum Instrumentation MIMO system as well as a 2-D scanning system for precise positioning of a microphone. A compiled program was created by the author using LabVIEW that is capable of applying many different types of improvements to time reversal while presenting an easy user interface. The software can also automate the collection of spatial pressures using the scanning system. J. M. Clift is an undergraduate researcher that began managing the development of the software. J. E. Ellsworth performed a major remodel of the electronics of the scanning system and made it possible to be repeatable. T. J. Ulrich and P.-Y. Le Bas are responsible for past software whose user interface inspired the current software interface. This chapter consists of an article published as A. D. Kingsley, J. M. Clift, B. E. Anderson, J. E. Ellsworth, T. J. Ulrich, and P.-Y. Le Bas, "Development of software for performing acoustic time reversal with multiple inputs and outputs," *Proc. Meet. Acoust.* 46, 055003 (2022) https://doi.org/10.1121/2.0001583. It is reprinted in this dissertation under the terms of ASA's Transfer of Copyright Agreement, item 3. I hereby confirm that the use of this article is compliant with all publishing agreements.

Volume 46 http://acousticalsociety.org/

182nd Meeting of the Acoustical Society of America
Denver, Colorado
23-27 May 2022

Signal Processing in Acoustics: Paper 3pSP1

Development of software for performing acoustic time reversal with multiple inputs and outputs

Adam D. Kingsley, Jay M. Clift, Brian E. Anderson and John E. Ellsworth
Department of Physics, Brigham Young University, Provo, UT, 84604;
adamkingsley@gmail.com; j@clift.org, bea@byu.edu, jee@byu.edu

Timothy J. Ulrich and Pierre-Yves Le Bas
Los Alamos National Laboratory, Los Alamos, NM; tju@lanl.gov; pylb@lanl.gov

At Brigham Young University, acoustic time reversal experiments are conducted in solids and fluid media. The experimental setup involves synchronized generation and acquisition hardware. The synchronized hardware allows for multi-channel generation, and in some cases, multi-channel acquisition of time reversal focusing. A LabVIEW application has been compiled to increase ease of use and repeatability for the students conducting experiments. Forward and backward steps of time reversal are conducted through this simple user interface. The software is also able to control a 2D positioning system that allows for the measurement of the spatial extent of a time reversal focus. Modifications to traditional time reversal processing, such as inverse filtering and one-bit processing, may be easily implemented in the software. This paper describes the hardware and software that facilitates time reversal research.

Published by the Acoustical Society of America

 https://doi.org/10.1121/2.0001583

1. INTRODUCTION

Time reversal (TR) is a signal processing technique for focusing waves.[1,2,3] It was originally performed by broadcasting an impulse and recording the response at another point[4] called the forward step. Broadcasting the response from either the source or receiver would produce a focus of waves at the other point, called the backward step. The amplitude of TR focusing increases and the amplitude of sidelobes decreases with additional sources used in the TR process due to the additional modes that can contribute to the focusing.[5] Similarly, TR focal amplitude benefits from reflections which can be seen as additional sources of converging waves.[6,7] Using a chirp instead of an impulse response has been shown to improve the signal-to-noise ratio for the simple reason that more power can be put into the system at each frequency during a long sweep rather than a short impulse.[8,9] When using a chirp signal during the forward step, the impulse response is obtained through a cross-correlation rather than a simple temporal inversion.

Using additional sources necessitates obtaining the impulse response from each source at the receiver location. The signal responses must be obtained sequentially, and time synchronized. The synchronization is essential because each source is going to attempt to create a focus and if the separate focusing events are not synchronized then the temporal and spatial resolution of the focus will be degraded. Synchronization can be achieved by enforcing simultaneous sampling from the source and receiver or by knowing the delay between the start times of the source and receiver recordings.

The purpose of this paper is to describe the challenges and solutions for creating a synchronized MIMO (multiple-input, multiple-output) system. This paper also lays out some of the capabilities that enable several TR processing methods, filtering of results, and spatial scans of the pressure field. Conducting TR experiments requires the necessary hardware as well as an intuitive software solution for the many students that will be using the system. This paper describes the hardware configuration used at Brigham Young University as well as the considerations and software solutions used in the program.

The original interface was inspired by software designed by T.J. Ulrich and Pierre-Yves Le Bas of Los Alamos National Laboratory who each developed software for similar purposes.

2. HARDWARE

The hardware setup used at Brigham Young University for TR research is a set of three Spectrum Instrumentation PCIe cards synchronized by a Star-Hub add-on module. The Star-Hub mounts directly to one of the cards and distributes the host card's clock to all the synchronized cards (including the host card). Two M2i.6022-exp arbitrary waveform generation (AWG) cards, each with 4 channels are hardware synchronized to a single M2i.4931-exp digitizer card. The Star-Hub distributes a sampling clock to all the cards in the system with minimal phase delay, enforcing the desired output-input synchronization.

To conduct 2D scans of the signal/focus response, two Applied Motion Products STAC 6i controllers are each connected to an Applied Motion Products HT23-550D stepper motor. Each motor controls the axis of a custom Macron Dynamics Inc. translation stage (see Fig. 1). This translation stage allows for 4 m^2 of scanning area with sub-millimeter precision. The frame can be assembled standing up or lying flat for measuring in a vertical or horizontal plane, respectively. Typically used by acoustics classes at Brigham Young University, this scanning system has been used in other research.[10,11,12]

Also at Brigham Young University, impulse response measurements are made in a water tank with a similar hardware configuration but with a derivative software interface.[13]

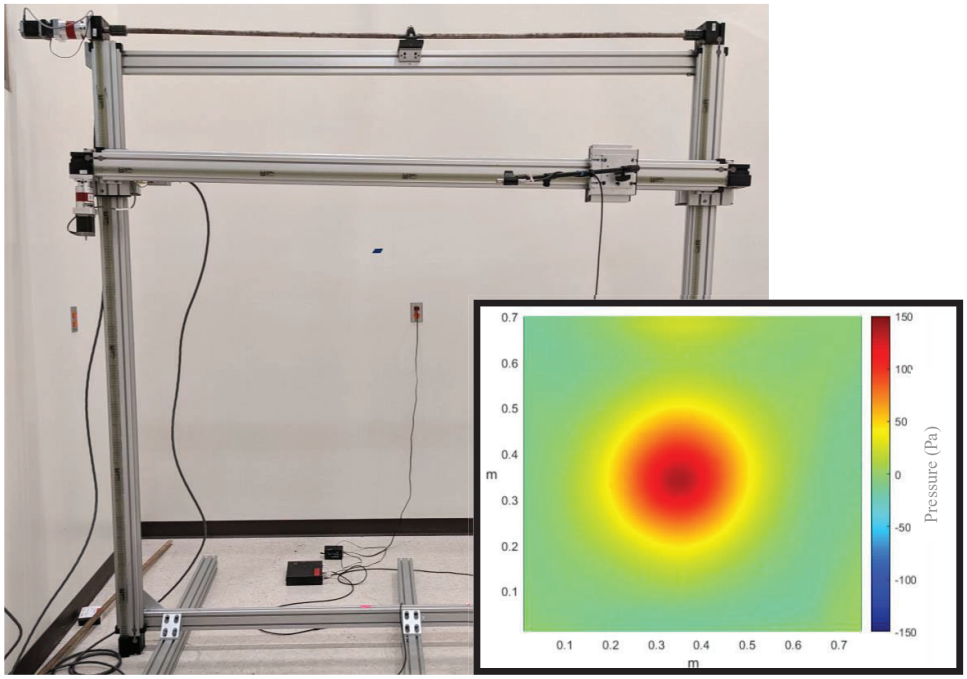

Figure 1. The Macron Dynamics Inc. translation stage used at Brigham Young University. The y-axis motor is horizontal at the top left. The crossbar is raised and lowered by the y-axis motor using the belts on the left and right connected by the rod at the top. The x-axis motor is on the left and controls the translation stage along the crossbar. Inset: An example result of a spatial scan of a focus obtained using TR.

3. SOFTWARE

Considering the hardware came from multiple manufacturers, LabVIEW was chosen as the most convenient programming language capable of interfacing with the internal and external hardware. With the goal of making a simple interface with the Spectrum cards, the software was named Easy Spectrum Time Reversal (ESTR). As shown in Fig. 2, the main function (termed Virtual Instrument or VI) serves as the hub for interface and commands but presents the user with access to the input/output subVIs or subfunctions. These subVIs generate, capture, and store the data that is used in ESTR. When initializing, the main VI and these subVI's (including the Motion VI) exchange references to their action queues so they can communicate in real-time.

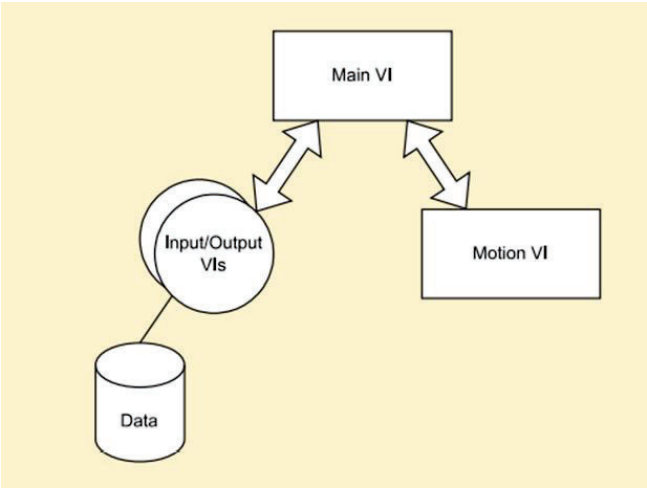

Figure 2. The hierarchy of ESTR is shown. The Main VI handles communication and operations between the subVI's as well as TR calculations. The subVI's for input and output handle the data and the subVI for motion control interfaces with the translation stage.

When ESTR starts, an initialization routine is run to discover the number of cards currently connected to the computer. Sets of controls are then made visible on the front panel for each card that was discovered. The user interface of ESTR consists of two copies of output/input displays (see Fig. 3). The set on the left is for the forward step of the TR process, i.e., for broadcasting the output signal sequentially and recording the signal responses from the single output to the enabled inputs. The set on the right is for the backward step of the TR process, i.e., for simultaneous broadcasting of all enabled output channels and recorded by all enabled input channels. Controls at the top of ESTR start the forward or backward steps. These options allow for averaging measurements as well as inserting a delay so that any reverberating sound remaining in the system can decay before the next recording starts.

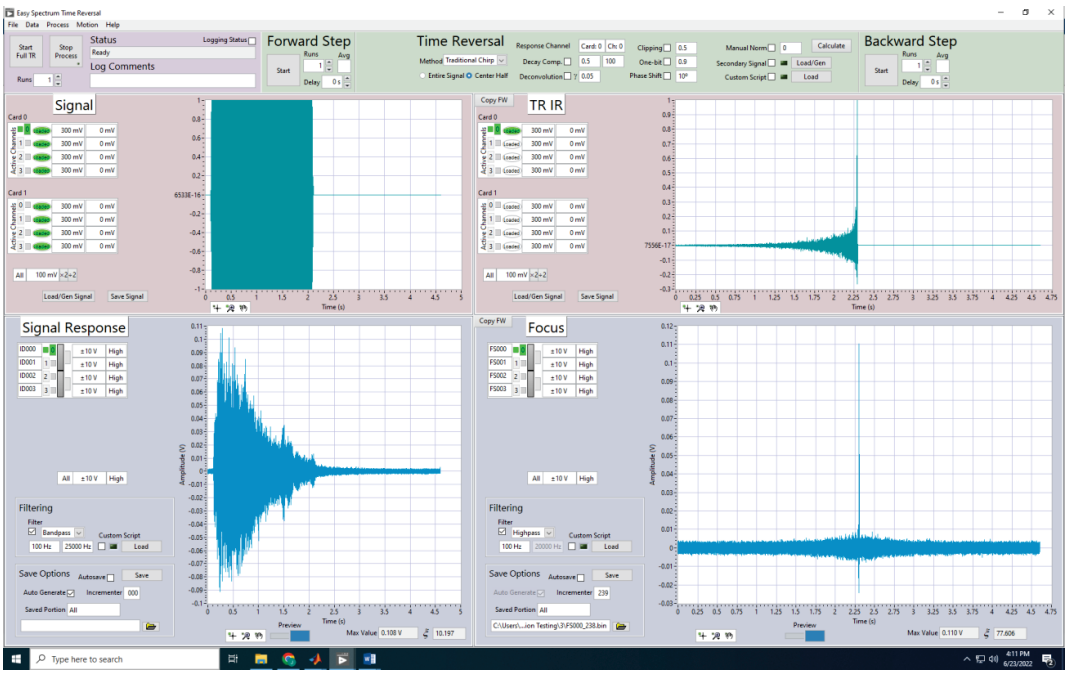

Figure 3. The main ESTR user interface is shown with the four panels labelled "Signal", "Signal Response", "TR IR", and "Focus". ESTR is currently showing controls for 2 output cards and 1 input card. Each card is equipped with 4 channels. The experiment shown used a chirp from a single channel to generate the focus seen in the bottom right.

Each of these pink and blue colored panes is run as an asynchronous VI that holds its own set of data. This data is an object containing the canonical data as well as metadata about the origin of the data (see Fig. 4). The data object is passed to the main VI when saving so that the metadata from all the steps can be brought together and saved in a corresponding log file. The dataset object (as well as the data contained in the object) are passed by reference within LabVIEW. The dataset object can contain up to three copies of the data with associated metadata as well as waveform objects for graphing. The first copy of the data is called the canonical copy and serves as the most reliable set of data. It is referenced and copied but never edited. The second copy is used when the user applies a filter. A copy of the canonical is made and the filter is applied to the copy. Lastly, the spectral data is the Fourier transform of the canonical data and is calculated once if the user changes the graph to view the spectrum.

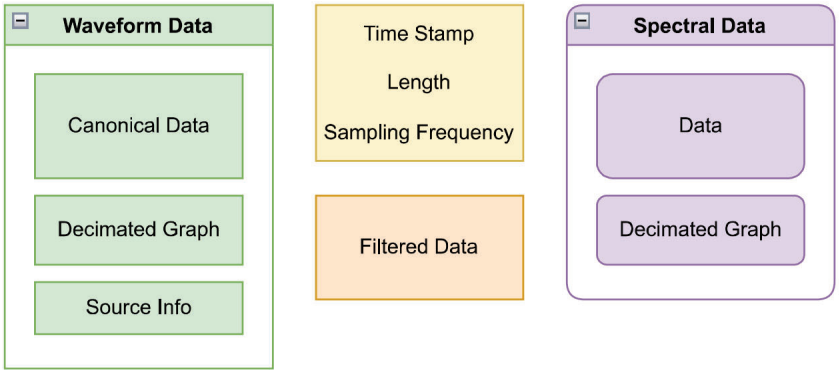

Figure 4. A schematic of the data object passed between the subVI's that make up the output/input and the main ESTR vi that processes and saves the data. Three copies of the data are shown with a canonical, filtered, and spectral datasets.

The user begins by generating a signal within ESTR or loading a data file to be used as the signal. Importing a signal starts when the user selects "Load/Gen Signal" button, and a new VI launches with signal generation options (shown in Fig. 5). The user selects the channels to load with data and then to whether to generate or import the data. The generation allows for a linear or logarithmic chirp, or a gaussian-modified sinusoidal pulse. The data is made of a signal portion with leading and trailing portions (zeros) with no signal. The trailing portion is for capturing the full impulse response ring down after the signal has finished playing. The leading portion allows verification that any reverberation from a previous broadcast has died down to the background noise before the next broadcast begins.

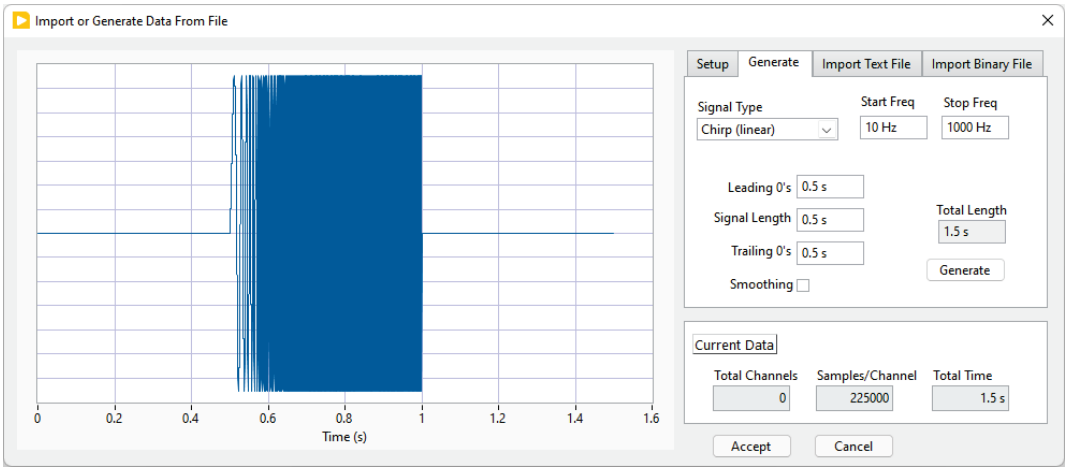

FIG. 5. The window for the subVI that handles importing or generating signals. The user selects the target channels and sampling rate, then the user can either import or generate a signal. Shown is a linear chirp signal from 10-1000 Hz without smoothing. If the user accepts the signal, then it is transferred to the output subVI.

After generating or importing data, the waveform is shown in the signal graph in the top left. The forward step can then be performed, and the signal response recorded (the recorded signal has the exact same time duration as the broadcast signal). After this forward step, ESTR can calculate the time-reversed impulse response (TRIR) using the signal and its response. Methods for calculating the TRIR are contained in a pane at the top of ESTR. This pane is shown in Fig. 6. The user can choose any set of options, including

combinations of options, and the TRIR(s) is(are) immediately calculated and displayed. This immediate feedback is helpful when enabling methods that use a threshold to distinguish between the parts of the signal to amplify or reject as noise. The order of the options in the Time Reversal pane is also the order that the calculation is performed. Finally, the TRIR(s) are normalized to maximize the available gain. Several of these options for calculating the TRIR are the result of published methods. The options include:

1. Response Channel. Although multiple inputs channels can be enabled, one of them must be chosen as the response channel when calculating the TRIR. The other enabled input channels are not used for the TR process but may have other uses.
2. Method. This option dictates whether the response is assumed to be the impulse response (e.g., when a pulse signal is played), in which case the TRIR is just the time-reversed response, or whether to perform a cross-correlation to obtain the TRIR from the signal (e.g., a chirp signal) and its response.
3. Entire Signal/Center Half. After the cross-correlation is performed, the resulting TRIR is twice the length of the signal. The beginning and ending of this cross-correlation are often near the noise floor. This option allows the user to only use a TRIR that is the same length of the signal and is taken from the center half of the TRIR (deleting the first and last quarters of the signal).
4. Decay Compensation.[14,15,16] Using an envelope of the decay of the TR, the decay is removed to allow the maximum amplitude of the TRIR. A larger amplitude is obtained than when simply reversing the impulse response and this method has been shown to introduce less harmonic frequency content into the TRIR signals than the clipping and one-bit techniques introduce.
5. Deconvolution.[17,18,19,20] As a modification of the IR, the deconvolution, or inverse filtering method compensates for frequencies with low amplitude in the IR by inverting the spectrum. When performing the inversion, frequencies outside of the signal bandwidth, or frequencies with a response below the noise floor, may be inverted to become very large. A modification to the deconvolution method places a constant bias in the denominator and stabilizes (regularizes) the deconvolution function, giving an upper bound to the output.
6. Clipping.[21,15,16] Clipping changes the maximum value to a fraction of the normalized TRIR. Samples with a magnitude greater than the threshold are placed at the threshold and the TRIR is normalized again.
7. One-bit.[22] Similar to clipping, the one-bit method uses a threshold and samples with a magnitude exceeding the threshold are placed at the threshold. Samples below the threshold are placed at zero. The TRIR is then normalized again.
8. Phase shift.[23] This allows for arbitrary phase shift added to all frequencies to manipulate the focus (e.g., to change the TRIR to focus the derivative of the response).
9. Secondary Signal. This is used for convolving a secondary signal with the TRIR prior to the broadcast of the backward step. In this way the impulsive focus can instead be a focus of the secondary signal (to communicate or deliver a desired signal).
10. Custom Script. This option allows the user to load a MATLAB script to manipulate the data in a way not already available in ESTR to truly create an arbitrary waveform.

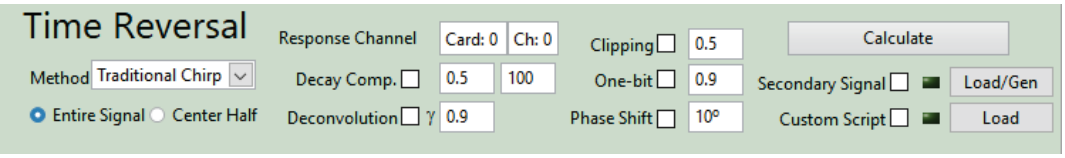

Figure 6. Options for calculating the time-reversed impulse response. Although changing any option immediately calculates the TRIR, the "Calculate" button allows using the default settings.

The filtering and save options for the forward or backward steps are located at the bottom of the input windows. This pane is shown in Fig. 7. The filtering is done with a zero-phase, 1st-order, Butterworth filter so that the timing of the waves is not affected. Because the canonical data is preserved, the filtering can be

turned on and off and the user can immediately see the results. The user can also load a MATLAB script to perform custom filtering. The save options include autogenerating filenames. The filenames consist of the channel name and an incrementor. To prevent accidental deletions, no overwriting is allowed.

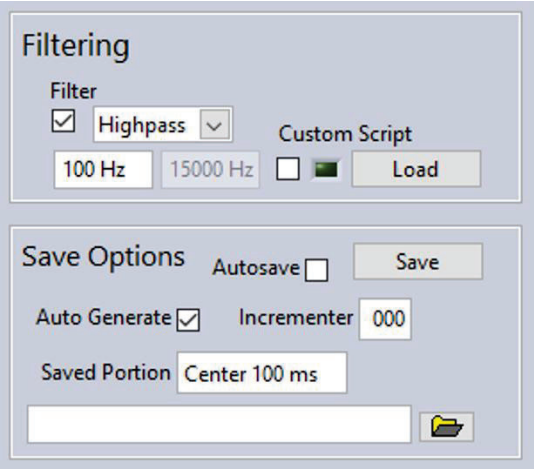

Figure 7. Options for filtering and saving the recorded data. These requests are handled by the input subVI.

4. MEMORY MANAGEMENT

The Spectrum cards have a maximum sampling frequency of 30 MHz. Utilizing the high sampling frequencies must include memory management considerations. Typically, LabVIEW performs its own memory management and garbage collection but in the case of large data sets (256 MB/channel) several tools are available and utilized in ESTR.

The first tool is passing by reference instead of by value. The data objects that are associated with each channel, are stored as a LabVIEW Data Value Reference. Within the object, the canonical and filtered data are each stored by reference. The output/input VIs must individually destroy the reference when the data is discarded, but this hierarchy is natural, and all data storage is left to the individual output/input VIs. In this way, the data is not duplicated while being viewed by the separate VIs performing calculations or saving. The memory requirements have been brought down to consist almost entirely of the data stored in the data object.

Another tool is when the data is first loaded into ESTR, the LabVIEW graph object is generated so that it can be called with minimal delay and without reproductions of the waveform object. In addition, the waveform objects are decimated when the data has many more points than the screen has pixels. In ESTR, the plots are limited to one million points. If the signal consists of more than one million points, the data is separated into 500,000 bins and the minimum and maximum of each bin stored in a new waveform object. If this decimation is performed, a warning label is made visible on the graph that informs the user that zooming in on the data will show inaccurate information.

Lastly, to save on time and memory requirements, the cards are not reloaded with the same data that has already been loaded. The Spectrum cards allow for playing the same signal several times without loading the waveform again. Because many TR experiments involve averaging or repeating the same signal, this saving of memory is also a time savings. To determine if new data needs to be loaded to the cards, the timestamp information from the loaded dataset is compared to the timestamp of the new dataset. If the timestamps are the same, then the data is not loaded to the cards and the previously loaded data is used instead. This simple comparison has found to be successful and sometimes necessary to reduce the time for some of the longer spatial scans. For a different system with a higher bus speed, this step will not save as much time.

5. MOTION CONTROL

ESTR uses a subVI for performing spatial scans (see Fig. 8). Initialization of the subVI starts an optional homing routine that moves the translation stage to trigger a magnetic proximity switch in both axes. After this routine the positions entered by the user are consistent between experiments. Several combinations can be performed which include performing a fully new TR experiment at each point, conducting the forward step at one point and the backward step at all points, or to perform just the forward or backward step at each position.

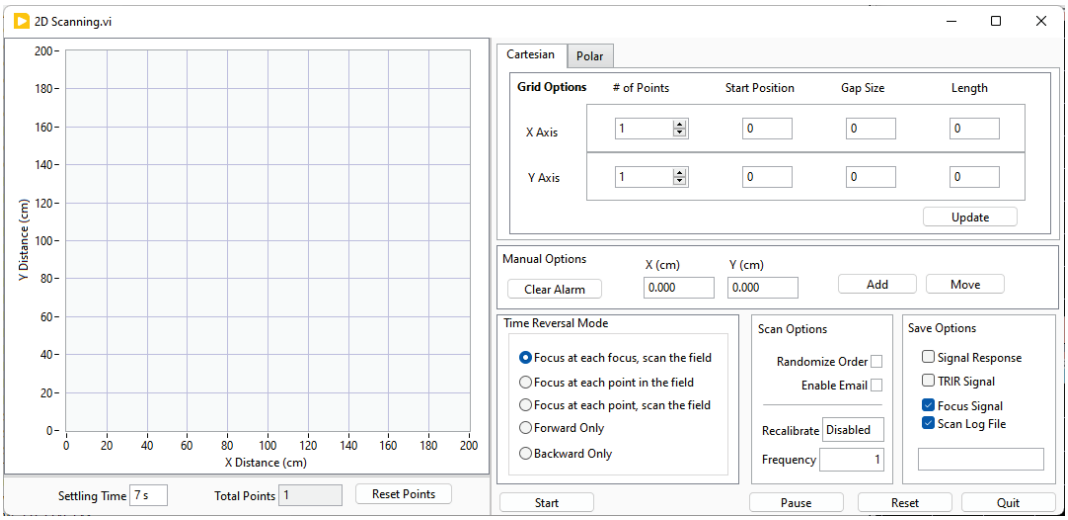

Figure 8. The 2D scanning subVI with the graph of points on the left and the grid and scan options on the right. The scanning system can also be moved to manual points by entering the X- and Y-coordinates or by clicking on the graph and then the move button.

The grid can be generated with regular spacing in each dimensions using rectangular or polar spacing. After generating a grid of points, the user can right-click a single point and designate it as the focal position. Currently the movement between points is a spiral originating at the focus and moving outward. This spiral progression allows for the highest accuracy in the measurement of the focal event, including the measurement at the focal location and the nearby surrounding locations, since temperature or other conditions may slightly change over time. If there is no focal position specified, the next position is just the one closest to the current position. Moving between the points can also be randomized which greatly increases the time to scan but ensures that temporal artifacts (e.g., a brief temperature fluctuation or a brief change in background noise) do not become spatial artifacts. Rastering options are being added as well as an option to do line scans.

Like the delay between successive recordings in ESTR, a settling time allows for the noise generated by the motors, (as well as vibration of the microphone arm), to decay after each movement of the positioning system.

6. CONCLUSION

This paper has described the hardware configuration for the TR MIMO system used at Brigham Young University. The 2D scanning system has also been described. The user interface for performing TR measurements and calculation along with the control of the 2D scanning system has been shown. Various TR processing techniques can be implemented, along with allowing for custom signal processing. Some of the considerations for data integrity and memory management have been describe and the architecture has

been outlined. Development continues on ESTR, but this paper provides insights into the core construction of the software.

Since its beginnings several years ago, ESTR has the gained many capabilities and has proven to be an essential part of the experimental TR work being performed at Brigham Young University. Although the students come and go, ESTR continues to gain features thanks to the next generation of students. Focusing on data integrity, repeatability, and ease of use, ESTR allows new student researchers to start making meaningful measurements with little training overhead.

ACKNOWLEDGMENTS

Funding was provided by Los Alamos National Laboratory, subcontract number 527136, under the technology maturation program. Additional support was provided by the BYU College of Physical and Mathematical Sciences.

REFERENCES

[1] M. Fink, "Time reversed acoustics," *Phys. Today* **50**(3), 34-40 (1997).

[2] B. E. Anderson, M. Griffa, C. Larmat, T.J. Ulrich, P.A. Johnson, "Time reversal". *Acoust. Today* **4**(1), 5–16 (2008)

[3] B. E. Anderson, M. C. Remillieux, P.-Y. Le Bas, and T. J. Ulrich, "Time reversal techniques," Chapter 14 in *Nonlinear Acoustic Techniques for Nondestructive Evaluation*, 1st Edition, Editor Tribikram Kundu, ISBN: 978-3-319-94476-0 (Springer and Acoustical Society of America), 547-581 (2018).

[4] C. S. Clay and B. Anderson, "Matched signals: The beginnings of time reversal," *Proc. Meet. Acoust.* **12**(1), 055001 (2011).

[5] S. Yon, M. Tanter, and M. Fink, "Sound focusing in rooms: The time-reversal approach," *J. Acoust. Soc. Am.* **113**(3), 1533 (2003)

[6] G. Ribay, J. de Rosny, and M. Fink, "Time reversal of noise sources in a reverberation room," *J. Acoust. Soc. Am.* **117**(5), 2866–2872 (2005).

[7] A. Derode, P. Roux, and M. Fink, "Robust Acoustic Time Reversal with High-Order Multiple Scattering," *Phys. Rev. Lett.*, **75**(23), 4206–4209 (1995).

[8] B. Van Damme, K. Van Den Abeele, Y. Li, and O. Bou Matar, "Time reversed acoustics techniques for elastic imaging in reverberant and nonreverberant media: An experimental study of the chaotic cavity transducer concept," *J. Appl. Phys.* **109**, 104910 (2011).

[9] B. E. Anderson, M. Clemens, and M. L. Willardson, "The effect of transducer directivity on time reversal focusing," *J. Acoust. Soc. Am*. **142**(1), EL95–EL101 (2017).

[10] B. D. Patchett, and B. E. Anderson, "Nonlinear characteristics of high amplitude focusing using time reversal in a reverberation chamber," *J. Acoust. Soc. Am.* **151**, 3603-3614 (2022)

[11] M. C. Mortenson, S. Gilbert, T. B. Neilsen, K. L. Gee, and S. D. Sommerfeldt, "Bandwidth extension of intensity-based sound power estimates," *J. Acoust. Soc. Am.* **147**, EL409 (2020)

[12] T. S. Furlong, B. E. Anderson, B. D. Patchett, and S. D. Sommerfeldt, "Active noise control using remotely placed sources: Application to magnetic resonance imaging noise and equivalence to the time reversal inverse filter," *Appl. Acoust.* **176** (2021)

[13] C. T. Vongsawad, T. B. Neilsen, A. D. Kingsley, J. E. Ellsworth, B. E. Anderson, K. N. Terry, C. E. Dobbs, S. E. Hollingsworth, and G. H. Fronk, "Design of an underwater acoustics lab", *Proc. Mtgs. Acoust*. **45**, 070005 (2021)

[14] A. S. Gliozzi, M. Scalerandi, and P. Antonaci, "One-channel time-reversal acoustics in highly attenuating media," *J. Phys. D: Appl. Phys*. 46, 135502 (2013).

[15] M. L. Willardson, B. E. Anderson, S. M. Young, M. H. Denison, and B. D. Patchett, "Time reversal focusing of high amplitude sound in a reverberation chamber," *J. Acoust. Soc. Am*. **143**(2), 696-705 (2018).

[16] S. M. Young, B. E. Anderson, M. L. Willardson, P. E. Simpson, and P.-Y. Le Bas, "A comparison of impulse response modification techniques for time reversal with application to crack detection," *J. Acoust. Soc. Am*. **145**(5), 3195-3207 (2019).

[17] M. Tanter, J.-L. Thomas, and M. Fink, "Time reversal and the inverse filter," *J. Acoust. Soc. Am.* **108**(1), 223–234 (2000).

[18] M. Tanter, J.-F. Aubry, J. Gerber, J.-L. Thomas, and M. Fink, "Optimal focusing by spatio-temporal filter. I. Basic principles," *J. Acoust. Soc. Am.* **110**(1), 37–47 (2001).

[19] T. Gallot, S. Catheline, P. Roux, and M. Campillo, "A passive inverse filter for Green's function retrieval," *J. Acoust. Soc. Am.* **131**(1), EL21–EL27 (2012).

[20] B. E. Anderson, J. Douma, T. J. Ulrich, and R. Snieder, "Improving spatio-temporal focusing and source reconstruction through deconvolution," *Wave Motion* **52**(9), 151–159 (2015).

[21] C. Heaton, B. E. Anderson, and S. M. Young, "Time reversal focusing of elastic waves in plates for an educational demonstration," *J. Acoust. Soc. Am.* **141**(2), 1084–1092 (2017).

[22] A. Derode, A. Tourin, and M. Fink, "Ultrasonic pulse compression with one-bit time reversal through multiple scattering," *J. Appl. Phys.* **85**(9), 6343–6352 (1999).

[23] L. A. Barnes, B. E. Anderson, P.-Y. Le Bas, A. D. Kingsley, A. C. Brown, and H. R. Thomsen, "The physics of knocking over LEGO minifigures with time reversal focused vibrations," *J. Acoust. Soc. Am*. **151**(2), 738-751 (2022).

Chapter 5

Focusing above a two-dimensional array of resonators in a three-dimensional environment

Time reversal focusing above an array of resonators creates subwavelength features when compared to waves in free space. Previous work has shown the ability to focus acoustic waves near the resonators with and without time reversal with an array placed coplanar with acoustic sources. In this work, a 2-D array of resonators is studied with a full 3-D aperture of waves in a reverberation chamber. The full impulse response is recorded, and the spatial inverse filter is used to produce a focus among the resonators. Additionally, complex images are produced by extending the spatial inverse filter to create focal images such as dipoles and quadrupoles. Although waves at oblique angles would be expected to degrade the focal quality, it is shown that complex focal images can still be achieved.

5.1 Introduction

A complex acoustic source can be described as a source with finite spatial extent and possibly nonuniform phase. In acoustics, the source can be rapidly imaged, e.g., by acoustic cameras [35]. However, determining the phase and amplitude distribution of such a source is complicated and becomes even more difficult when the dimensions of the source are

subwavelength in scale and the distance to the detector is great. Furthermore, if the source is in a reverberant environment, then traditional beamforming techniques (e.g., as used by acoustic cameras) are greatly hindered by the inherent multiple scattering. Because of principles similar to the diffraction limit, recordings of waves in the far field of a source produce indistinguishable patterns [1]. Imaging is closely related to focusing of waves and, thus, the ability to focus a complex pattern is used to represent the ability to image a complex source. In other words, if a complex image can be created by distant sources, then a complex source can be imaged by distance receivers. The question of imaging a distant source then moves to the question of acoustic focusing at a distance.

Acoustic time reversal (TR) focusing is a mature subject [21, 2, 3, 5] used for focusing waves in many different contexts including medical ultrasound [36] and non-destructive evaluation of structures [37, 38]. TR has also been used to image a source by numerical backpropagation of the recorded waves [39, 13]. The simple process of TR begins with emitting a signal from a source and recording that signal with a receiver, or using a receiver to record the emissions from an unknown source. By time-reversing the recorded signal and broadcasting it from the receiver location, a focus is observed at the source location. Alternatively, if one has control over the source broadcast, then a cross-correlation of the broadcasted chirp signal with the recorded response to this chirp signal yields the band-limited impulse response (IR). This IR may be reversed in time and the broadcast of the time reversed IR (TRIR) yields delta-function like focusing of energy. This process of broadcasting the TRIR causes all frequencies to constructively interfere at a point in space and time. The TRIR may be broadcast from the original source and the focusing happens at the receiver, or the TRIR may be broadcast from the receiver location and the focus occurs back at the original source location. The temporal

characteristics of the TR focus can be changed by convolving the TRIR with a desired signal and then broadcasting this modified TRIR. The new focal signal becomes the desired signal instead of the delta-function like response.

This reversal of the recordings is the simplest version of TR. When performed experimentally for laboratory testing, it is often convenient to broadcast the reversed recordings (i.e. TRIR) from the source locations instead of from the receiver locations. This method is sometimes called reciprocal TR [5] because it depends on the reciprocity of the system to allow for an equivalent response between a pair of points, regardless of which point is the source and which is the receiver. Imaging a source can then be related to the ability to focus a spatio-temporal signal that represents the source. The ability to focus complex characteristics is equivalent to the ability to image the complex characteristics of a source.

Sub diffraction limited focusing has been the goal of many focusing methods [16]. TR has been shown to be capable of producing a focus much smaller than the diffraction limit would suggest in free space. This is performed by modifying the near-field of the focus using a source [40], absorbers [41, 13] or resonators [14, 15, 42]. Because the diffraction limit was postulated for propagating waves, it does not apply to the near-field evanescent waves and thus sub-diffraction limited focus sizes are achieved if the free-space diffraction limit is used as the criterion [1]. This can be understood by examining the boundary conditions. Near a boundary, the propagating waves must conform to match the boundary conditions. The boundary is under no constraints about resolution and so the waves, when close to a boundary, may have much higher spatial resolution than found in the free-space propagating wave.

When seeking to create a spatial focus, the impulse responses between each source and every point in the imaging area must be taken into consideration. A transfer function (***H***)

represents the frequency transform of the impulse response. At each frequency, $\boldsymbol{H}$ is represented by a complex number, H_{SR}, represents the response between source ($\boldsymbol{S}$) and receiver ($\boldsymbol{R}$) with both amplitude and phase. All the interactions between sources and receiver positions can then be represented with a matrix formulation:

$$\begin{bmatrix} H_{11} & \cdots & H_{n1} \\ \vdots & \ddots & \vdots \\ H_{1m} & \cdots & H_{nm} \end{bmatrix} \begin{bmatrix} S_1 \\ \vdots \\ S_n \end{bmatrix} = \begin{bmatrix} R_1 \\ \vdots \\ R_m \end{bmatrix}, \tag{5.1}$$

where n and m refer to the number of the source and receiver locations respectively. Although this equation only represents a single frequency, it describes a total response rather than the individual response represented by a single transfer function.

As written, Eq. (5.1) does not allow for producing a specified response. However, by inverting the transfer function matrix $\boldsymbol{H}$, a desired response vector $\boldsymbol{R}$ can be used to discover the necessary source signals to produce such a response:

$$\begin{bmatrix} S_1 \\ \vdots \\ S_n \end{bmatrix} = \begin{bmatrix} H_{11} & \cdots & H_{n1} \\ \vdots & \ddots & \vdots \\ H_{1m} & \cdots & H_{nm} \end{bmatrix}^{-1} \begin{bmatrix} R_1 \\ \vdots \\ R_m \end{bmatrix}. \tag{5.2}$$

This spatial inverse method uses the inverse of $\boldsymbol{H}$ to obtain calculate the source vector $\boldsymbol{S}$ has been used in acoustics as well as in electromagnetic propagation [43, 44]. A method of iteratively discovering the inverse transfer matrix has also been utilized in a similar TR experiment [15]. This problem is ill-posed and is often unstable. Taking the inverse of the transfer function can often lead to inverting small responses that are dominated by noise. The resulting inverse would then be dominated by these noisy signals. To solve this problem, a singular value decomposition is first performed producing a series of transfer matrices. Use of eigenmodes or a singular value decomposition have been used in acoustic TR in the past [45, 46]. Each transfer matrix can be represented as $\boldsymbol{H} = \boldsymbol{U\Sigma V}^{\dagger}$, where $\boldsymbol{U}$ and $\boldsymbol{V}$ contain a sequence of

eigenmodes, † designates the conjugate-transpose operation, and $\boldsymbol{\Sigma}$ is a diagonal matrix whose elements consist of the corresponding eigenvalues. To invert this series of matrices requires taking the reciprocal of the elements (eigenvalues) in $\boldsymbol{\Sigma}$,

$$[\boldsymbol{U\Sigma V}^{\dagger}]^{-1} = [\boldsymbol{V\Sigma}^{-1}\boldsymbol{U}^{\dagger}] = \left(\boldsymbol{V} \begin{bmatrix} \frac{1}{\sigma_{11}} & 0 & \cdots & 0 \\ 0 & \frac{1}{\sigma_{22}} & \ddots & \vdots \\ \vdots & \ddots & \ddots & 0 \\ 0 & \cdots & 0 & \frac{1}{\sigma_{tt}} \end{bmatrix} \boldsymbol{U}^{\dagger} \right). \tag{5.3}$$

Because many of the eigenvalues are small, regularization is often applied. Before taking the reciprocal, a threshold for the eigenvalues is introduced and the eigenvalues above the threshold, l, are determined. After taking the inverse of $\boldsymbol{\Sigma}$, any elements originally below the threshold ($\sigma_{nn} < l$) are set to zero. In this way, a noise-filtered inverse of $\boldsymbol{H}$ is calculated. The threshold can be determined empirically by using the quality of the results and repeating the process with different thresholds. For the experiments described in this chapter, a threshold of 10% of the max was applied at each frequency to remove just the lowest eigenvalues. It is expected that improvement to this regularization would lead to an improved image using the resulting inverse matrix.

The purpose of this chapter is to show that complex sources may be imaged with sub-diffraction limited resolution using TR in the presence of an array of near-field resonators. This chapter explores the ability of this spatial inverse filter method to produce complex images in the pressure field. An array of soda cans is reused from previous focusing work [15, 19]. This time, however, the array is in a reverberation chamber, and the full impulse response of the room (i.e., a 3-D aperture) is utilized for focusing sound above this 2-D array of resonators. This chapter builds on the previous work with scatterers (see Appendix A) as well as the work with resonators

in one dimension from Chapter 2 [23] and Chapter 3. In this chapter, results are shown for an experimental setup where complex 2-D images are produced in the near-field of the resonators.

5.2 Experimental Setup

An array of soda cans constitutes an acoustic metamaterial, or phononic crystal, possessing properties that come from the arrangement and properties of the individual elements [14]. This array of soda cans has been previously shown to produce focusing on the order of the size of the opening in a single soda can, although the resolution is actually limited by the discretization of the space, which is clearly the spacing between soda cans [15, 19].

The current experiment places the 2-D metamaterial in a 3-D space to test the ability of the material to modify the waves and create images with high spatial frequency. In the reverberation chamber, some of the impinging waves come at oblique angles and do not interact with the whole array in the same way as coplanar waves. Prior work by Lemoult *et al*. [15] and Maznev *et al.* [19] principally or wholly utilized coplanar waves [15, 19]. This is similar to measuring a plane wave with an array of microphones. If the plane wave travels along the axis of the microphones, the measured wavelength is the true wavelength of the wave. However, if the plane wave is incident at an oblique angle to the microphone array, any incident wave manifests a wavelength across the array that is greater than the true wavelength of the wave. The extreme case is when the wave direction is perpendicular to the microphone array. Since all of the microphones would record simultaneous excitation, the array would effectively record the arrival of a wave with an infinite wavelength.

The experimental setup of an array of soda cans (12 fl. oz.) held in a vertical plane as shown in Fig. 5.1(a). A 1 m^2 steel plate hangs on a vertical piece of medium density fiberboard. Each

soda can has a small magnet glued to the underside that allows the cans to stay firmly in contact with the metal plate while also allowing the flexibility of other arrangements of the cans. Suspending the cans in the vertical plane allows the experiment to be moved away from the walls and floor where a spatial dependence to the focusing amplitude has been found [47]. The vertical plane was also convenient for the 2-D scanning system, which is positioned coplanar to the array with a microphone attached to the translation stage. When moving over the array, the microphone is 1 cm above the soda cans. Eight Mackie HR824mk2 loudspeakers are placed throughout the room roughly at the same height as the bottom of the resonator array constituting a horizontal plane that is perpendicular to the array of the cans. The loudspeakers were oriented such that they were pointing away from the cans, towards the chamber walls to minimize the strength of the direct sound arrivals relative to the reverberant sound [48]. The whole setup is positioned within the large reverberation chamber at Brigham Young University. The chamber measures 4.96 x 5.89 x 6.98 m with a total volume of 204 m^3. The Schroeder frequency, above which the field is assumed to be diffuse, is 355 Hz. Custom LabView software (ESTR) described in Chapter 4 [34] is used along with a Spectrum Instrumentation MIMO system to control the loudspeakers, microphone and scanning system.

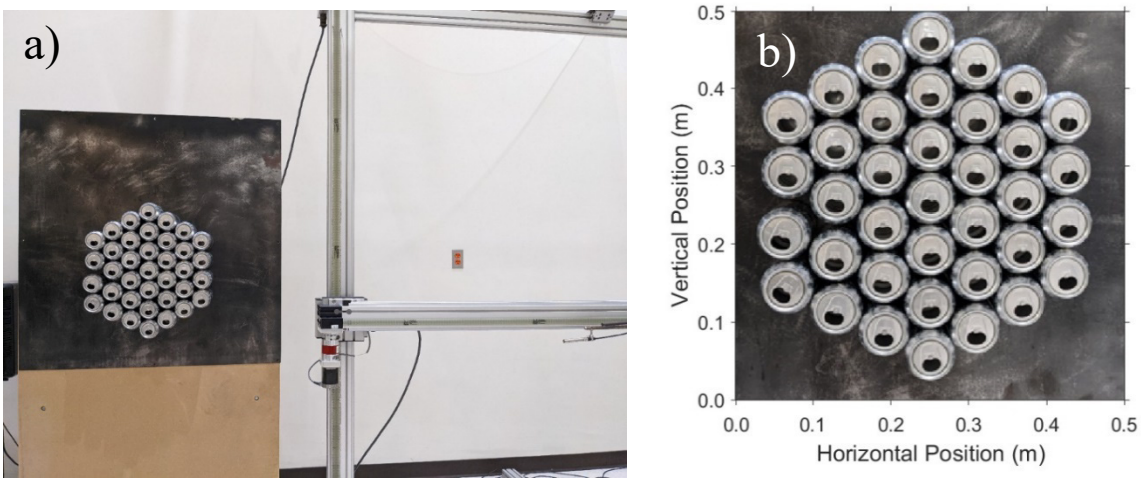

Figure 5.1 (a) Photograph of the experimental setup. (b) A hexagonal array of soda cans is mounted in the vertical plane and a 2-D scanning system is used to make measurement above the soda cans.

The experimental procedure is similar to acoustic TR except instead of simply reversing the impulse response, the spatial inverse filter described above (Eqs. (5.1)-(5.3)) is used to create the signals for the focusing step. First, a series of chirp broadcasts are made from each source. The microphone is moved between sets of broadcasts to capture the response at each measurement position in the grid above the array of soda cans. Time invariance is assumed: Many measurements are made by a single microphone are assumed to imitate the simultaneous recording of many microphones. A swept sine wave (chirp) is used because it generates near uniform amplitude over a range of frequencies, which results in a high signal to noise measurement of the impulse response for the bandwidth [49]. For this experiment, a grid of 51 x 51 points was used with a spacing of 1 cm, each measurement point was centered over the opening in the can. Figure 5.1(b) shows the measurement area as well as the position of the cans relative to the measurement area.

The chirp had a bandwidth of 300 Hz to 425 Hz. By cross-correlating the response with the chirp signals, an impulse response is obtained between each source and receiver position. A

Fourier transform of these impulse responses yields a series of transfer matrices, one for each frequency. Using the inverse of an individual transfer matrix $\boldsymbol{H}$, the necessary signal $\boldsymbol{S}$, can be calculated from a desired response $\boldsymbol{R}$, for a single frequency. This spatial inverse method was performed by solving Eq. (5.2) for each frequency and producing spectra for each source. Due to the attenuation of the array, an upper frequency of 410 Hz was used during this step, leading to an effective bandwidth of 300 Hz to 410 Hz. An inverse Fourier transform then produces a set of eight time signals, which are broadcast into the system and generate a focus above the array. Figure 5.2 shows the magnitude of the spectrum for the chirp, an example spectrum of an impulse response, an example spectrum produced by the spatial inverse filter, and an example resulting focus spectrum. The drop in amplitude as the frequency approaches the resonance of a single can (approximately 400 Hz) is seen in the impulse response spectrum. This attenuation near resonance is expected by previous research into reflection by single resonators but also by the resonator arrays constructed previously [15, 19].

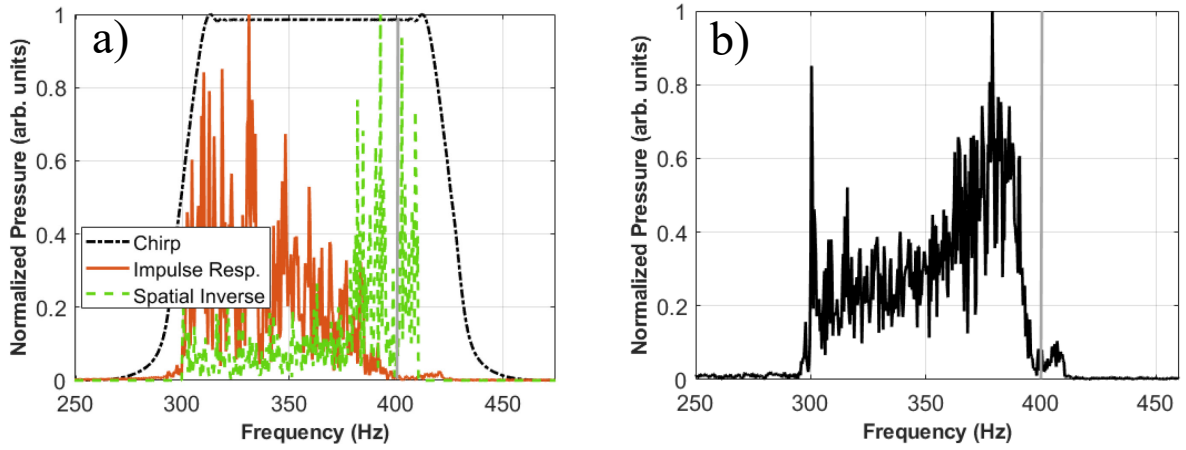

Figure 5.2 (a) Spectra for the forward signal (black, dot-dashed), the calculated impulse response (red, solid), and the derived signal to create a point focus using a spatial inverse filter (green, dashed). (b) The spectrum at the resulting focus. A vertical gray line marks the approximate resonance frequency of a single resonator (400 Hz).

5.3 Results

The results from a series of experiments are described in this section. The results utilize the process described above with several different specified response patterns. The rectangular grid above the soda cans consists of 2601 points. This grid was trimmed down to a hexagonal area which represents the measurement surface made above the resonator array. For the 1392 locations above the resonator array, the pressures at the focal time compose the desired image $\boldsymbol{R}$. The experiments conducted in this chapter only used a few points that were set to nonzero values. Although the image is 2-D, Eq. (5.2) uses a 1-D vector of sources and receiver positions, regardless of their relative positions. This vectorized image, $\boldsymbol{R}$, was then combined with each frequency of the transfer matrix $\boldsymbol{H}$, one by one, to obtain the spectra of the source signals $\boldsymbol{S}$. These spectra were converted to time waveforms, imported into ESTR, and broadcast simultaneously from all loudspeakers.

5.3.1 Monopole Focusing

The first and most simple focusing is that of a monopole, point focus. By setting a single point of $\boldsymbol{R}$ to be one, and all other points to be zero, the sharpest focusing can be measured. Monopole focusing at two different positions is shown in Fig. 5.3. Also shown is the case when cans are not present. Positions above individual soda cans were chosen as targets.

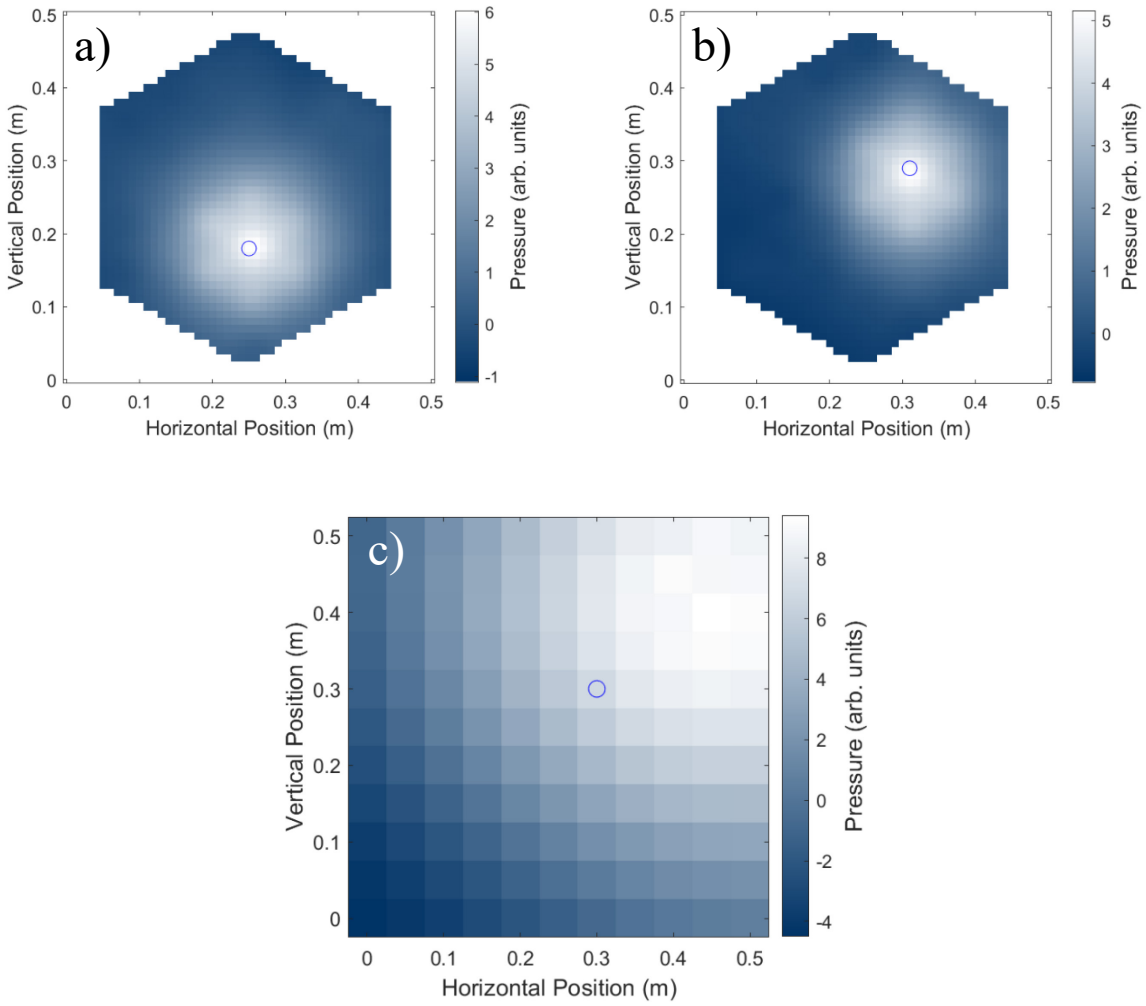

Figure 5.3 Spatial plots of the pressure amplitude over the array for the monopole case. White represents high pressure and blue represents low (or negative) pressure. A blue circle marks the target position. (a) Focus at the can just below center. (b) Focus at the can above and to the right of center. (c) A case without resonators with the focus location shown with a blue circle.

It is evident from Fig. 5.3 that the spatial inverse filter can produce a focus that is much smaller in spatial extent than without the cans present. In the case of no resonators, the spatial inverse filter does not produce a maximum at the focal location. This error in the location of the focus without cans may be caused by an improper threshold applied to the SVD process. This threshold is responsible for filtering out noise before the inverse is calculated. Thus, amplified noise may be shifting the focal position.

Although using the spatial inverse filter couples the responses of the sources, the frequencies are still independent variables. Because the frequencies are independent, a target image can be achieved more easily with some frequencies than others. Bringing together the contributions of the many frequencies may lend more total power to frequencies for which the target image is not well reproduced. For the array of soda cans, the dispersion relation does not follow a linear function of frequency and yields much smaller wavelengths than in free space and has been explored previously [19, 23]. With the assumption that high-resolution images are more able to be generated with higher frequencies, the focus above the cans was filtered with progressively smaller bandwidth (while maintaining the same upper frequency cutoff and using that same upper frequency to define the resolution in each case). With a reduced bandwidth the focus becomes tighter, suggesting that coupling the thresholds between frequencies may have the advantage of increasing the sharpness of the focus. Figure 5.4 shows the spatial extent of the focusing when using a bandpass filter with the lower frequency marked in the legend. As the lower passband frequency increases, the focus becomes tighter (always better for the case with resonators than without).

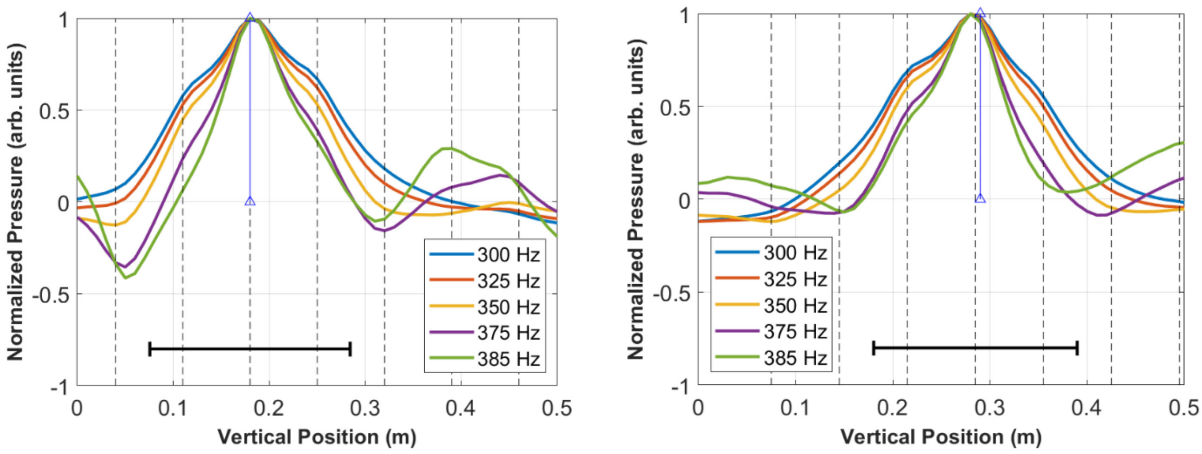

Figure 5.4 Normalized pressure above an array of soda cans at focal time. The target focus location is shown with a vertical line and a blue arrow. Several bandwidths are shown with the lower limit in the legend and a constant upper limit of 410 Hz. A quarter wavelength at 410 Hz is marked, for scale, with a black horizontal line. As the passband becomes smaller, the focus becomes tighter. Black dashed vertical lines denote the locations of can openings.

The results in Fig. 5.4 are further analyzed by considering the full-width at half maximum lengths in Table 5.1. These values are taken from the graphs in Fig. 5.4 but written in terms of the free-space wavelength in air of the highest frequency in the bandwidth (410 Hz). The size of the focusing at the two different target focal positions are similar and always much better than without the resonators present. As expected, the values also show that the higher frequencies are much more capable at producing a sharp focus when compared to the case without resonators. For the narrowest filter results shown, the bandwidth is only 25 Hz; this case is still capable of focusing to a target position and produces a focus to a location five times smaller than without the cans present. This result is impressive because in the limit that the bandwidth narrows to a single frequency then the waveform becomes a sine wave with no distinct focus. So, although the array of soda cans is only 2-D and many waves may come from oblique angles to the array, the array is still capable of interacting with the coplanar waves sufficiently to cause a high spatial frequency in the resulting focus. This work lends confidence to the ability of a 2-D acoustic

metamaterial to improve imaging, even in a 3-D space. For future applications, it is important to understand that these results were obtained when the loudspeakers are in a plane that is perpendicular to the plane of the soda cans and that the multiple scattering (reverberation) exploited by the TR process tends to provide incident waves from all directions.

Table 5.1 Full width at half-maximum (FWHM) values of the focal pressure for the bandwidths used in Fig. 5.2, with λ as the free field wavelength at 410 Hz.

Lower passband frequency	**300 Hz**	**325 Hz**	**350 Hz**	**375 Hz**	**385 Hz**
Position 1 FWHM	0.202 λ	0.188 λ	0.164 λ	0.115 λ	0.113 λ
Position 2 FWHM	0.204 λ	0.193 λ	0.170 λ	0.128 λ	0.108 λ
No Cans FWHM	0.596 λ	0.576 λ	0.570 λ	0.572 λ	0.564 λ

5.3.2 Dipole Wave Field

The next imaging case was the orientation of the resulting focus of a dipole wave field. To generate dipole focus, two points of $\boldsymbol{R}$ were chosen to have nonzero values of +1 and –1. Two dipoles, one in the vertical and one in the horizontal plane were focused. The resulting spatial maps of are shown in Fig. 5.5. Although the vertical dipole is well-aligned with the vertical axis, the horizontal dipole suffers from some angular uncertainty and looks more like it is focusing diagonally. This difference may have to do with the symmetries in the array of cans. For closer examination, a line scan is plotted in Fig. 5.6 and shows an asymmetric dipole for the horizontal dipole. The spatial map, however, shows that the orientation seems to be the source of the error. There are several possible reasons for this result. A limitation of having the sources in the same plane in the room could lead to an error in orientation. The attempt to create a dipole using cans

that are not adjacent could cause this error. As the size of the dipole (i.e., distance between poles) increases, more error in the orientation may occur using the spatial inverse methods. A large spatial side lobe could exist below the horizontal dipole that was unavoidable due to some geometric symmetry in the setup. Lastly, a position closer to the edge of the array was used for targeting. Positions close to the edge should exhibit properties somewhere between that of central portion of the array and free space. Another feature shown in Fig. 5.6 are bumps above each resonator. These bumps were predicted by a previous model of a one-dimensional array using an equivalent circuit approach [23] and show a strong near-field interaction with the resonators.

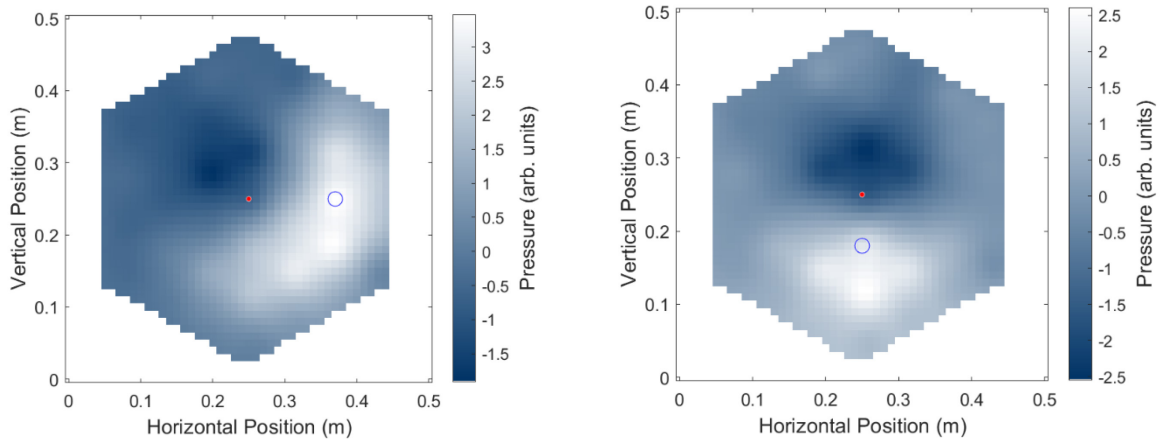

Figure 5.5 The spatial extent of a horizontal (left) and vertical (right) dipole at focal time. White represents high pressure and blue represents low pressure. A blue circle marks the target positive pole. A red dot marks the target negative pole.

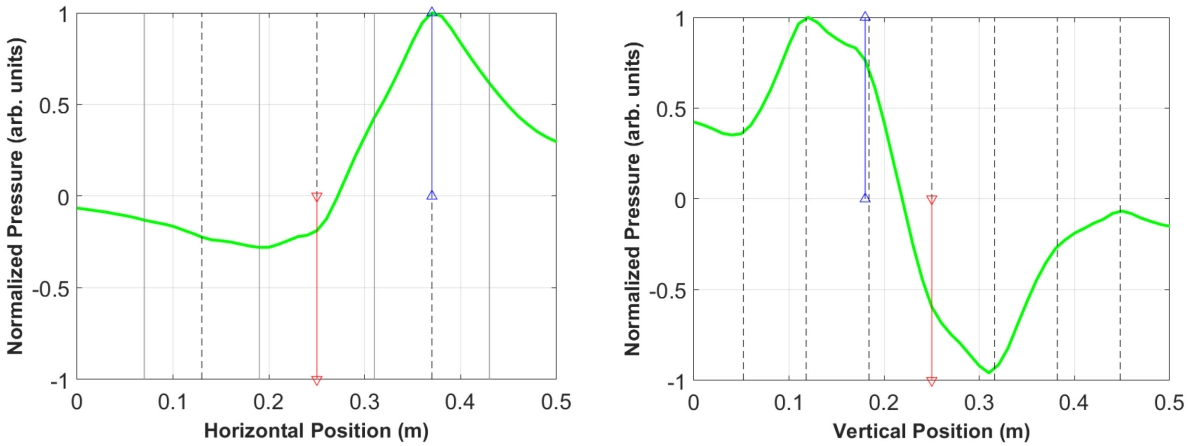

Figure 5.6 Normalized pressure values along the axis of the horizontal (left) and vertical (right) dipoles. The target positive pole is shown with a vertical line and a blue arrow and the target negative pole is shown with a vertical line and a red arrow. The positions of cans along the axis are shown with dashed vertical lines. The horizontal dipole has columns of cans that are out of plane; these are marked with a solid grey line.

5.3.3 Quadrupoles

Two different types of quadrupoles were attempted. A vertically oriented longitudinal quadruple and a lateral quadrupole. Similar to the dipole cases, several values of ***R*** were set to nonzero values. As shown in Fig. 5.7, for the vertical longitudinal quadrupole, the positive poles were collocated, and the resulting target amplitudes were [-0.5 1 -0.5] within the ***R*** vector. The lateral quadrupole did not have the poles placed over cans but instead were placed nearly centered between the cans in a square arrangement. The patterns for both quadrupoles are in very good agreement with the expected pressure patterns of these classic source arrangements. Figure 5.8 shows a plot of the 1-D pressure along the vertical axis of the longitudinal quadrupole. A quadrupole was created but the position of the poles does not exactly match that of the target pattern. For comparison, Fig. 5.9 shows the focusing results when these patterns are attempted using the spatial inverse filter but without the resonators present. The resulting pressure fields

show faint signs of creating the target patterns but not all of the poles are captured in the resulting image, whereas with the resonators present the spatial extent of the patterns is much tighter.

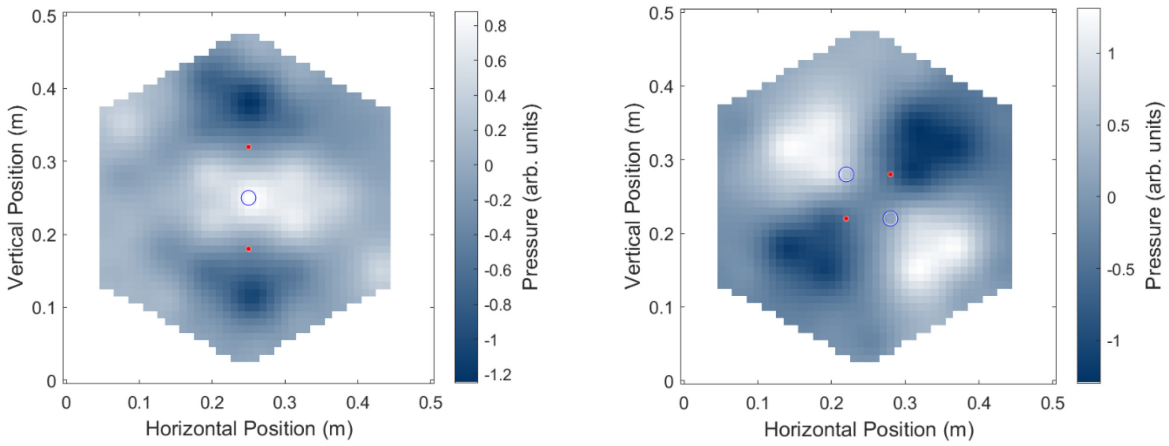

Figure 5.7 Pressure amplitudes at focal time for vertically-oriented longitudinal (left) and lateral (right) quadrupole. These patterns show nodal lines and spatial extent that is much smaller than could be reproduced without the resonators. White represents high pressure and blue represents low pressure. A blue circle marks a target positive pole. A red dot marks a target negative pole.

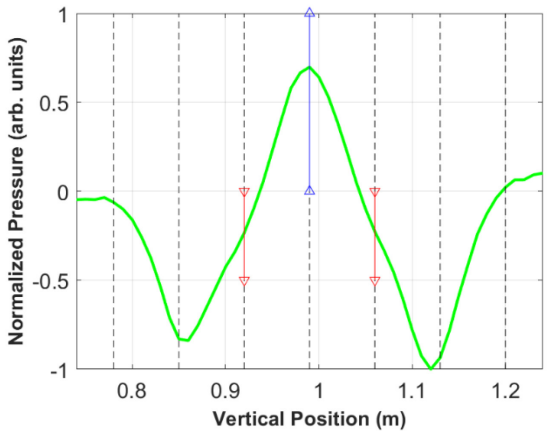

Figure 5.8 One dimensional plot of the normalized pressure of the longitudinal quadrupole along the vertical axis. The positions of the positive and negative poles are denoted by vertical lines with blue and red colored arrows, respectively.

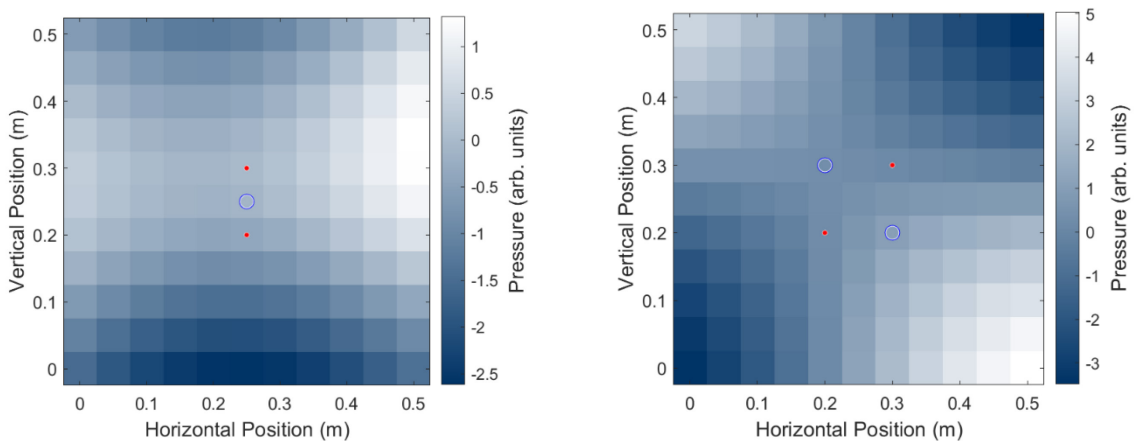

Figure 5.9 Pressure for a vertically-oriented longitudinal (left) and lateral (right) quadrupoles created without the presence of resonators. Although the patterns are visible, the spatial extent of the pattern is much wider than when the resonators are present. White represents high pressure and blue represents low pressure. A blue circle marks a target positive pole. A red dot marks a target negative pole.

5.3.4 Complex pattern

The last target pattern was a much more complex pattern. An attempt was made to obtain a 'Y' pattern (a simplified version of the Brigham Young University logo). The ***R*** vector contains 19 nonzero values with 7 values set to +1 and 12 values set to –1. Figure 5.10 shows the result of this attempt. The signals were filtered with a bandpass from 375 Hz to 410 Hz. The resulting pattern does indeed resemble a 'Y' but suffers from resolution limitations near the arms of the 'Y'. There appears to be a positive pressure hexagon shape around the outside perimeter that distorts the intended image most likely due to fringe effects. Figure 5.10 also shows a cropped image and modified colormap meant to empirically enhance the 'Y'.

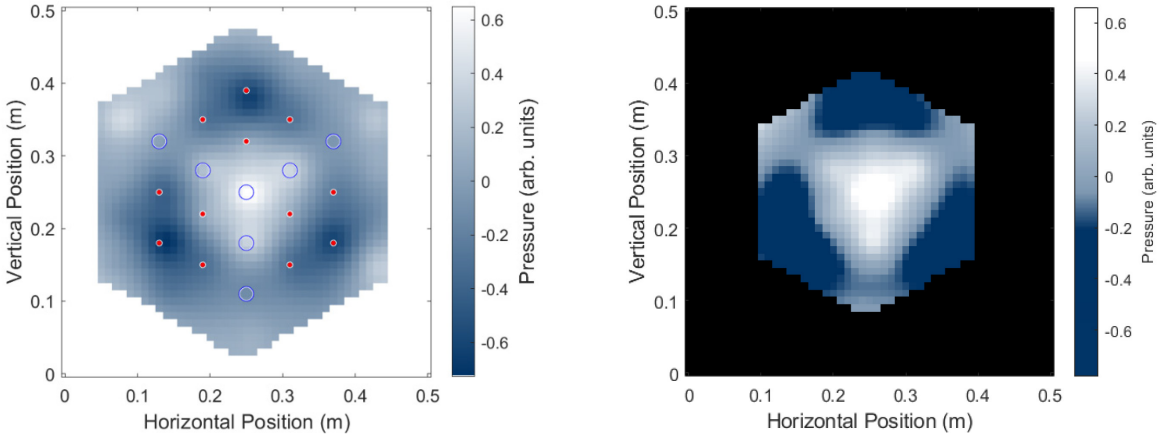

Figure 5.10 A complex 'Y' target pattern is obtained over resonators (left). White represents high pressure and blue represents low pressure. A blue circle marks a target positive pole. A red dot marks a target negative pole. By reducing the image area and adjusting the color scale, an improved version of the 'Y' is easier to see (right).

5.4 Conclusion

As evidenced by the spatial results for imaging of complex sources shown in this chapter, a 2-D array, resonant acoustic metamaterial is capable of modifying near-field pressure in a 3-D environment. This capability to recreate complex imaging fields, including orientation, means that the ability to image a complex source located near a resonant material could be improved beyond the diffraction limit of free-space waves. In effect, the material can extend the size of the source, relative to a wavelength, in a similar fashion to a lens, and enable far-field imaging of sub-wavelength features. Limitations on the ability to create any arbitrary image could possibly occur due to the arrangement of sources or the geometry of the setup. Specifically, knowledge of the impulse responses above the resonators is necessary to create the images seen in this work using a spatial inverse filter.

This work is a natural extension of previous work with acoustic metameterials and especially arrays of resonators. This study has shown subwavelength focusing is possible

because the wavelengths above the array are much smaller than in free space. The results confirm that using a simultaneous solution, such as inverting the transfer matrix to obtain a spatial inverse filter, is a viable method for producing high resolution images from a distance. Evidence has been given that the full impulse response, including reflections from all directions within the room and scatterers, does not meaningfully impair the ability to produce sub-diffraction limited images. Although the spatial inverse filter solves for the contributions from all of the sources at a single frequency, some frequencies have higher spatial frequencies above the cans and manually filtering the results or coupling the thresholds, can yield even tighter focusing.

Chapter 6

Conclusions

This dissertation outlines the three approaches used to analyze the sub-diffraction limited focusing of acoustic waves in the presence of near field resonators. The research approaches include analytical, numerical, and experimental methods that together describe the wave physics interactions of the acoustic waves near an array of resonators. These interactions of wavelengths that are much smaller than free-space wavelengths may appear to be unusual, but the compact spacing of the arrays of resonators and the impact of each resonator on the phase of propagating waves causes these effects. By building the arrays from the properties of single resonators, a better understanding of the physics involved has been presented.

6.1 Equivalent Circuit Analytic Model

The first major approach taken to model these systems was in using an equivalent circuit analytic model. In the waveguide, the resonators cause partial reflections and thus attenuate the incoming waves. Without anechoic terminations these reflections would immediately lead to large standing waves outside the array of resonators with amplitudes that would be many orders of magnitude greater than the amplitude of the waves found among the resonators. By introducing losses at the ends of the waveguide, the response among the resonators is easier to see. The geometric properties of the resonators have been studied and especially their influence

on the subwavelength focusing. Specifically, lower quality factors, which describe resonances with wider bandwidths, lead to corresponding larger bandwidths of subwavelength behavior. As the frequency approaches the resonance of a single resonator from below, the resulting effective wavelength decreases rapidly. With this decreased effective wavelength, however, comes a much stronger attenuation and the resulting focus is much smaller in amplitude as a result. In summary, a tradeoff exists between the increased resolution of the focusing with a wider bandwidth and the resulting amplitude of that focusing. To maximize imaging resolution and ensure that the image stays within the resonator array, then low Q resonators are desirable.

The equivalent circuit model also describes a strong interaction at every resonator position. This interaction is visible as a local amplitude gain where the slope of the spatial pressure changes quickly. These local amplitude gains were initially thought to be non-physical, especially when the numerical simulations did not seem to show these bumps in the spatial pressure. However, the experimental results over a 2-D array did show these bumps.

6.2 Numerical COMSOL Simulations

The natural extension to the equivalent circuit model was a full-wave simulation using COMSOL Multiphysics. This numerical simulation served as a validation of the equivalent circuit model while also extending the results to the case when the side-branch resonators have finite-sized necks at the junctions with the main duct. The COMSOL simulations confirmed the validity of the observations in the equivalent circuit model, which is much faster to run computationally. Although the underlying models are very different, excellent agreement was generally found when comparing the transfer functions of the two models. However, the transfer

functions deviate considerably for frequencies near the resonance frequency of a single resonator.

Creating the COMSOL model first required measuring not only the resonance frequency of a single resonator but also the change to the resonance frequency when that resonator is placed into the model duct. The radiation impedance of the resonator was strongly affected by the dimensions of the duct, and although numerical models exist for the impedance of this type of junction, the models produced different results. The equivalent circuit model was able to predict the same impulse response in the duct. This prediction was verified by using the impulse response generated by the equivalent circuit model to generate a focal event within the COMSOL model.

The COMSOL model was used to view the full-wave pressure in the duct and near the openings of the resonators. The modeled wave was confined to the openings of the resonators, as suggested by the circuit modeling, as the frequency approached the resonance frequency of a single resonator. When the spacing of the resonators was much smaller than a wavelength, the resulting modified wave appeared to have an effective wavelength that varied on the order of the spacing of the resonators. In other words, at the frequencies where the wave was most affected by the resonators, the period of the wave matched the period of the resonators.

6.3 Experimental Results

The first experiments were conducted with scatterers (work done mostly by an undergraduate student, Emily Golightly). These results can be found in Appendix A. The results showed that the path length could be changed with pure scatterers (no reactance). Although the resulting wave could appear to have subwavelength properties, the waves were simply rerouted

around the scatterers, such that the measurements were not being conducted along the direction of propagation. Rather the measurement points were made at selected observation points along the main trunk of the system. Three-dimensional experiments were conducted with 1000 spherical scatterers in a tight lattice and a simple improvement in focusing was found. In this most extreme case of waves entering a small structure, the minimal improvement was expected by the small change in the path length of the wave. The author contributed a lot of ideas and analysis tools for this research effort in addition to the ESTR software that was used.

The experimental efforts then shifted to the reactance and phase shifting properties of resonators. A simple experiment was conducted, similar to historical experiments performed with laser light in dispersive media [50, 51]. A pulse of sound was sent down a plane wave tube and past a single Helmholtz resonator. Using measurements with and without a resonator, a resulting phase shift could be calculated. The phase shift was delayed below resonance and then was advanced above resonance, similar to what was found with the phase speed of a wave in the 1-D duct of resonators studied in COMSOL (see Chapter 3). The phase speed decreases to very low values below resonance but immediately above resonance the values are so high that waves do not appear to propagate but rather attenuate. Although this simple shift by a single resonator was insufficient to explain the exact nature of the overall phase speed in an array of resonators, it does provide some physical intuition about the changes in the phase speed of resonators among an array of them.

The final suite of experiments was conducted using a 2-D array of Helmholtz resonators, specifically, Barq's branded root beer cans. The cans were suspended away from the walls and floor and a two-dimensional scanning system moved a microphone over the cans. Measurements of the impulse responses from eight loudspeakers were made at various locations in a grid with

very fine spatial resolution over the cans. The cans provided sufficient differences in the impulse responses between subwavelength points, such that focusing could be achieved at arbitrary target cans within the array. Although some waves could come into the array with near-normal incidence (perpendicular to the plane of the resonator array), this did not stop the waves among the cans from creating subwavelength images that could not be achieved without the resonators present.

6.4 Future Work

As this work has progressed, several areas of interest have arisen that will be the subject of future research.

6.4.1 Reducing dimensions

This 2-D experiment in 3-D space raises the possibility of further improvements by restricting the dimensions. Undergraduate student Andrew Basham is currently conducting research using a 2-D waveguide by placing a second boundary above the resonators and restricting wave propagation to only waves that are coplanar with the array. The author has been heavily involved in the advisement and planning of these experiments.

6.4.2 Obfuscation of a source

This work has primarily focused on increasing resolution, another goal of the research is to obfuscate the radiation from sources. Although the focal results look very different when using the resonator array compared to when the array is absent, the question remains if the focus looks

significantly different when the array is only present for the forward or backward steps of the TR process. This approach would simulate the ability of the resonator array to encode information about the source that can only be reconstructed when the properties and positions of the resonators are known.

Los Alamos National Laboratory is interested in this dual-purpose improvement of using resonators, that is, improving imaging resolution for authorized listeners and degraded resolution for unauthorized listeners. In other words, while the resonator array improves the imaging resolution, it remains to be seen if the resonator array degrades the imaging resolution if the cans are not taken into account during imaging.

6.4.3 Decomposing the wave field

Basham is also currently working to decompose the wave field to view the in-plane and out-of-plane contributions to the pressure. The in-plane contributions are expected to be more affected by the resonators. This method may mean that it is possible to use the array in a 3-D space, but then computationally reduce the field to simulate when the array is in a 2-D space.

6.4.4 Nonlinearities at the mouths of the cans

When the soda can array was assembled, early experiments showed the time of the focus moved with a linear increase in the amplitude of the sources. This amplitude-dependent timing is most easily attributed to the orifices of the soda cans. Expected nonlinearities arise at an orifice due to the change in the way the particle velocity pattern at the opening changes with increasing amplitude. Although the focal amplitude was not high enough to generate waveform steepening

or Mach stem formation nonlinearities, the pressure inside the resonators may be large enough. Further research into this possibility is expected to be undertaken by a future student.

Appendix A

Super resolution, time reversal focusing using path diverting properties of scatterers

This appendix consists of the work of several researchers at Brigham Young University related to subwavelength focusing. Originally the overall research was directed at using the scattering rather than the resonant properties of a material. As the research into subwavelength focusing using TR began, the possibility of using scatterers was explored. Lucas Barnes was an undergraduate researcher that helped to assemble a network of 1000 metal balls. Two undergraduate researchers, Emily Golightly and Rebekah Higgins, began conducting experiments with the scatterers. As research continued, the idea of path diverting scatterers was proposed and Golightly began working with that topic. Later, other students including Rylee Russell and Spencer Neu, constructed a new arrangement of the ball scatterer network and Russell conducted a suite of experiments aimed at measuring the improvement in TR focusing among the balls.

The author was involved in the design and setup of the ball scatterer experiments as well as mentoring the undergraduates as they began conducting experiments and began using ESTR. The author also conducted simulations and assisted in the development of figures and code to process the results. The author was also involved in the editing of the manuscript that resulted (this appendix).

Although the value of scatterers in subwavelength focusing was less than that of resonators, it is important to recognize that phase speed can appear to be slower than the group speed. In the

case of scatterers, that is due to an effective increase in the path length through which the waves travel through the network. In the case of path diversions, that is due to measuring the spatial response along a route that is not the same as the one in which the waves actually travel through.

This appendix is a manuscript primarily written by Emily Golightly and is currently under review.

A.1 Introduction

Time reversal (TR) is a type of signal processing that can be used to focus waves to a specific point in space [3, 5, 37]. This is accomplished by recording an impulse response (IR) at a certain location, reversing it in the time domain, and broadcasting the reversed IR from either the original source or receiver locations. The first half of this process, known as the forward step, and the second half of the process, known as the backward step, can both be performed either experimentally or numerically. Here the source and receiver are kept in the same locations in the forward and backward steps and both steps are done experimentally. Because portions of the waves travel a similar path as they did initially, both directly through the medium and indirectly via reflections, broadcasting a reversed IR enables a focus to be created at the receiver location, which is a reconstruction of the originally broadcast signal.

TR has been used in focusing large amplitude sound, for communications, and to reconstruct sources in a variety of applications. It has been used to destroy kidney stones as a form of non-invasive surgery [36, 52], locate cracks in structures [37, 53, 12, 54] find the epicenter of earthquakes and characterize their type of motion [55], and locate the place a user taps on a touch screen device [56]. One current aim of TR research is in increasing the spatial resolution of the final focus, in order to better image the original source. The goal of such research is to achieve

super resolution, which is resolution greater than the diffraction limit, commonly defined as a spatial peak in the far field narrower than one half a wavelength of the signal, or $\lambda/2$, at the full-width at half maximum (FWHM) of a intensity distribution. However, for the spatial dependence in a one-dimensional system, the FWHM diffraction limit is $\lambda/3$ (or $\lambda/4$ for a pressure quantity). Although resolution below these limits may initially appear to violate the established science behind the diffraction limit, a better explanation of this phenomenon may be that the assumptions of the diffraction limit are not met in cases where super resolution is achieved [1]. For example, focusing may occur in the near field of obstructions, rather than in an unobstructed far field. Here, super resolution means better resolution than can be achieved in a free-space medium, and thus the diffraction limit may not be technically broken [1]. Many experiments that use TR to achieve super resolution involve placing objects in the near field of a source or receiver [14, 15, 40, 41, 13]. Resonators are the objects that have most often been used in TR super resolution research. Lerosy *et al.* conducted an experiment using electromagnetic waves and copper wires that achieved resolution of 1/16 the size of the diffraction limit (or up to λ/32) [14]. While they referred to the copper wires as "resonant scatterers," the nature of electromagnetic waves inside of a wire suggests that these wires are more aptly considered resonators than scatterers. Other experiments have used the Helmholtz resonance of soda can resonators to achieve similar results with acoustic waves [15]. Other methods that have been used in achieving super resolution include using an acoustic sink [40], using experimental or numerical absorbers [41, 13], and finally a technique that amplifies near field information [42].

There are currently several explanations of how super resolution can be accomplished without breaking the diffraction limit. These explanations involve information contained only in the near field, and information lost in the transition from the near field to the far field. The near

field is the area closest to a source, often within a fraction of a wavelength. In this area, waves interfere and contort differently than they do once they reach the far field. In particular, the near field includes evanescent waves, which exponentially decay with distance from the source, and that are specific to the near-field conditions. When objects, such as resonators, are placed in the near field, it may disrupt the regular propagation of evanescent waves, enabling the information contained in these waves to be propagated into the far field, thus allowing the receiver to record a greater amount of data about the wave source than otherwise possible. With this additional information, the backwards step of TR can then reconstruct the source with better spatial resolution than it could otherwise [14]. It is also possible that measuring the near field information, and amplifying it, would enable its information to improve resolution in TR experiments [42]. The idea of an acoustic sink is to place an active source at the focal location that broadcasts opposite phase energy while energy is being focused in order to cancel out the far-field information, leaving only the near field information behind [40]. A technique known as sponge layer damping involves putting numerical absorbers around a focal location in order to suppress the converging far field information, making it easier to measure the near field information [13]. Finally, physical absorbers have been placed to surround a focal location in order to reduce the converging far-field information [41].

Another possible explanation of the super resolution phenomenon is that objects close to the source and/or receiver force the wave to travel a longer path in order to cross the same effective distance [57]. As Maznev *et al*. described it, the objects form a medium for the wave to travel through that has a lower phase speed than the wave would have traveling outside of the medium [19]. Although the actual speed of the wave remains constant, the phase of the wave modulates at a different speed than the wave speed. If this spatial modulation (wavenumber) increases then the

spatial resolution of the wave will be the same as if it was travelling through a medium with a lower wave speed. With a lower effective wave speed, the wavelength is also lowered, allowing the spatial extent of a focused signal to have a resolution smaller than the original diffraction limit.

Thus, while there are several studies that have shown super resolution can be achieved using resonators and other objects [14, 15, 40, 41, 13], and several explanations have been offered as to how super resolution is possible in these experiments [14, 40, 41, 13, 42], the use of a network of scatterers as a potential means to lower the effective wave speed to obtain super resolution has not yet been shown. Previous TR experiments using scatterers have investigated rotating scatterers between the forward and backward steps to show that this inhibits TR focusing [58], but they did not explore the potential for achieving super resolution. Scatterers can be as simple as spheres or other geometrically creative objects and may provide a useful alternative to other approaches. The purpose of this chapter is to describe experiments where path diversions were used to simulate diffraction or multiple scattering that could be used to achieve super resolution if the actual path length is not taken into consideration or measurements are not made along the propagation path. By forcing the waves to travel a longer path between measurement locations (traveling around a scatterer), the wave takes a longer time to traverse the distance it would have traveled had the scatterer not been present. The result is that the wave appears to travel at a lower speed, which leads to effectively shorter wavelengths.

A.2 Experimental Setup

Experiments were conducted inside polyvinyl chloride (PVC) pipes of 1.905 cm (3/4 inch) inner diameter (Fig. A-1). A pipe system was chosen to limit wave propagation to one dimension

(the dimensions impose a plane wave cutoff frequency of about 10.5 kHz), and thus one-dimensional propagation is guaranteed for the frequency range of interest. PVC connectors were used to create a 9.14 m (30 feet) length pipe system out of three 3.05 m (10 feet) pipes. The overall length of the pipe system was chosen to allow for several closed-closed pipe resonances (along the pipe's length) to exist within the bandwidth used. The center 3.05 m pipe had 6.35 mm (1/4 inch) diameter holes drilled into it every 12.7 cm (5 inches), for a total of 23 holes. The holes were used as measurement locations and unused holes were covered with sticky putty to prevent sound from leaking out of the pipe system. Measurements were made using a 6.35 mm (1/4 inch) GRAS (Holte, Denmark) 40BE free field microphone with a GRAS 12AX 4 channel power module. Two additional 3.05 m length pipes were connected on either end of the center pipe that did not have measurement location holes in them as part of the main trunk of the 9.14 m pipe length. The focal location (where the IRs are measured and the subsequent focusing occurs), the additional measurement locations, the extra main-trunk pipe lengths, the sources, and the amplifiers are indicated in Fig. A-1.

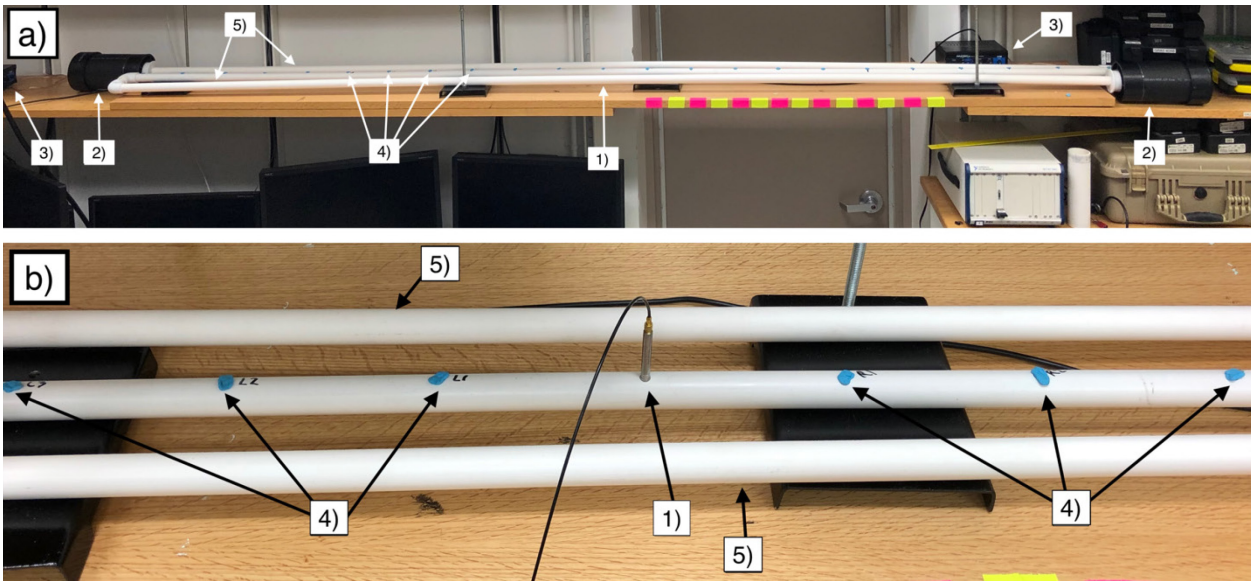

Figure A-1 (a) Photograph of the experimental setup for the control experiment, (b) Close-up photograph of the center portion of the control experiment setup. Items identified in the images: 1) Focal location, 2) Black-colored PVC pipes that house the sources, 3) Amplifiers, 4) Sampling at additional measurement locations, 5) Extra main-trunk pipe lengths.

At each end of the pipe system, a section of black-colored PVC pipe 10.2 cm (4 inch) inner diameter was attached and a Tang Band (Taipei, Taiwan) WS-881SJ loudspeaker driver was secured inside it (see Fig. A-1, location 2). Two Pyle Pro (Brooklyn, New York) PCA3 stereo power amplifiers (Fig. A-1, location 3) were used to provide power to the loudspeakers. Appropriate connectors and caps were placed on each end of the pipe system to ensure that the system had minimal sound leakage. All signals were generated and processed for TR using a custom LabVIEW™ software [34], coupled with two Spectrum (Großhansdorf, Germany) M2i.6022-exp signal generation cards and a Spectrum M2i.4931-exp digitizer card. All post-processing was handled in MATLAB™. The sampling frequency used throughout these measurements was 150 kHz.

In the forward step, the microphone was placed in the center receiver location (the previously determined focal location; see Fig. A-1, locations 1) and all remaining holes were covered with sticky putty (Fig. A-1, locations 4). A logarithmic chirp signal from 100 Hz to 500 Hz was played from a single loudspeaker, and a signal response was recorded by the microphone, as illustrated in Fig. A-2(a) and Fig. A-2(b), respectively. This chirp range was chosen due to its large wavelength, which enabled recording of the spatial extent of the time reversed focus at multiple locations within a single wavelength to compare to the diffraction limit. It should be noted that averaging was used extensively to reduce the noise found in individual trials.

The IR for the loudspeaker and microphone combination was calculated using a cross-correlation of the original chirp signal with the response recorded by the microphone when the loudspeaker plays the chirp signal [48, 59]. This process was repeated for the second loudspeaker with the microphone in the same location, and the two IRs were then reversed in time and played simultaneously from their respective loudspeakers, creating a focus at the center receiver location (focal location), as in Fig. A-2(c) and Fig. A-2(d).

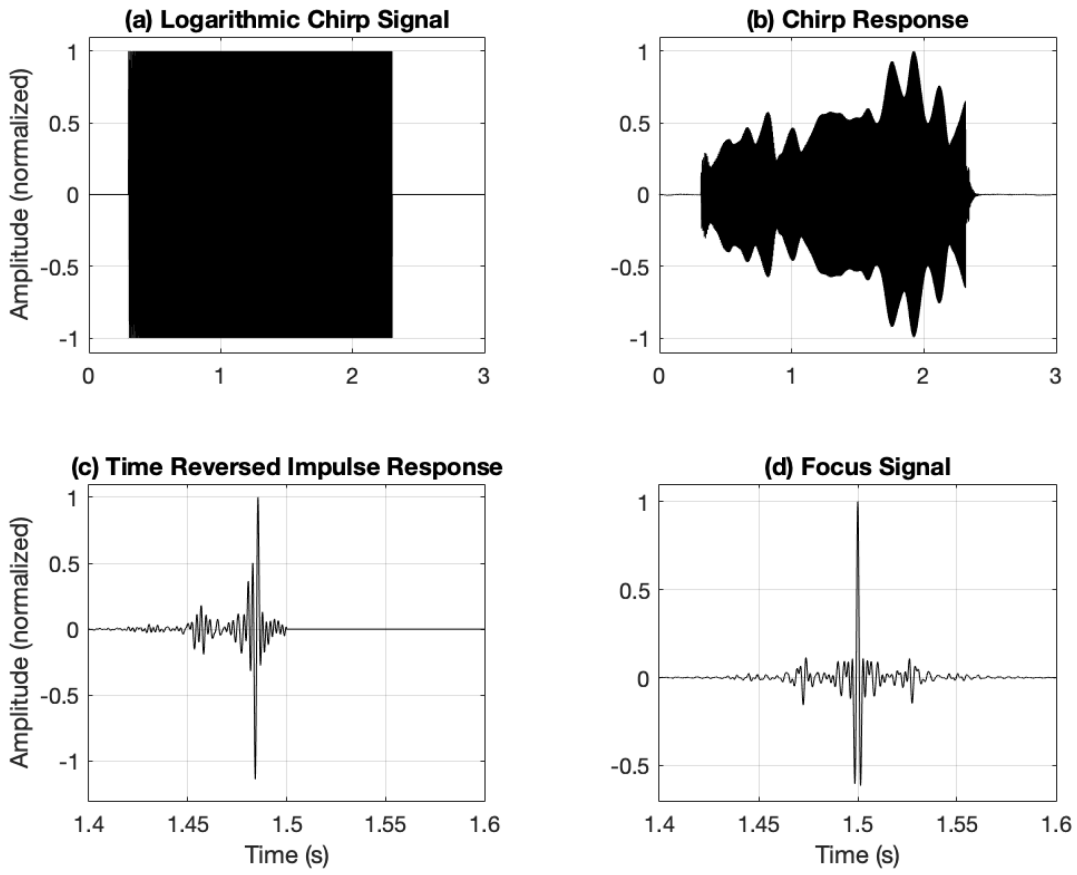

Figure A-2 Example signals for a time reversal experiment. (a) The chirp signal initially played from both loudspeakers. (b) An example chirp response recorded at the focal location. (c) A time reversed impulse response. (d) A focus signal recorded at the focal location, generated by both loudspeakers. Amplitudes in this figure were normalized.

After the focus was recorded at the focal location, the microphone was moved to another measurement location, and the two reversed IRs were played again, allowing measurement of the same focal event at a different point in space. This process was repeated for the remaining 21 measurement locations. The signal was then filtered with a lowpass, zero-phase, 6^{th}-order Butterworth filter with a 200 Hz cutoff frequency. Graphs of the spatial extent of the focus at the focus time were made in post-processing.

Once this control experiment was completed, the center 3.05 m pipe was removed from the pipe system and replaced with a pipe of the same length that included path diverting PVC pipes of 1.27 cm (1/2 inch) inner diameter, as shown in Fig. A-3. The smaller diameter in the path-diverting pipes was used to increase the amount of scattering within the pipe system. These pipes left the plane of the original pipe system and came back within a 12.7 cm space, and were placed between the middle eleven receiver locations, for a total of ten path diversions (Fig. A-3, locations 6). The pipe with the path diversions had holes drilled in the same receiver locations as the control pipe, and the same experiment was repeated with the new pipe system. A total of four different lengths of path diversions were used with an out-of-plane distance of 5.08 cm, 10.16 cm, 15.24 cm, and 30.48 cm pipes. The total path diversion is thus double the out-of-plane distance, e.g., the 5.08 cm pipes increased the total distance traveled within the pipe system between each receiver location from 12.7 cm to 22.86 cm.

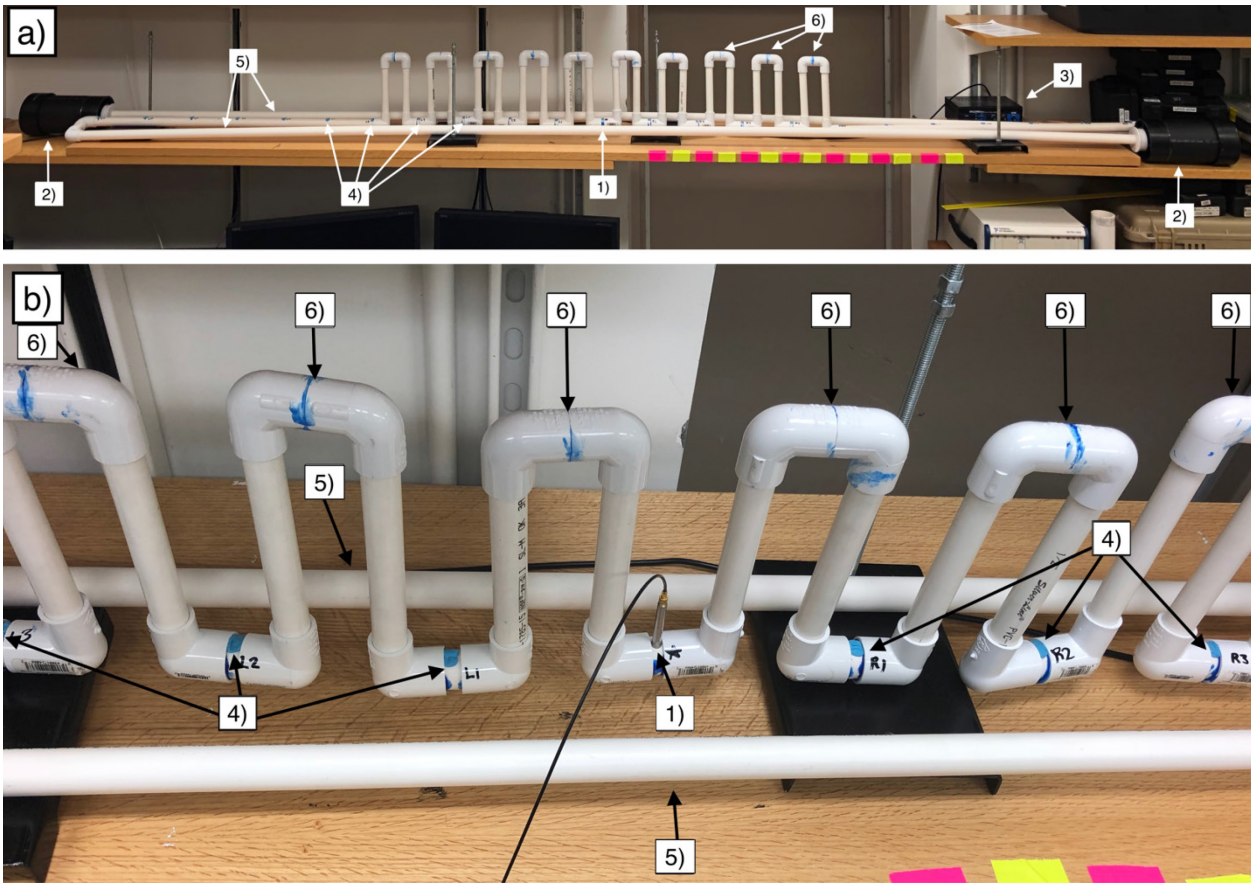

Figure A-3 (a) Photograph of the experimental setup including path-diverting scatterers, (b) Close-up photograph of the center portion of the experimental setup using path-diverting scatterers. Items identified in the images: 1) Focal location, 2) Black-colored PVC pipes that house the sources, 3) Amplifiers, 4) Sampling at additional measurement locations, 5) Extra main-trunk pipe lengths, 6) Sampling at path diversions added after control experiments were completed. This image shows the pipe system with 15.24 cm path diversions.

A.3 Results

Using these path diversions, each of the spatial foci measured showed apparent super resolution when the path diversion lengths were not accounted for. Table A-1 lists the FWHM of each length of path diversions with respect to λ and compared to the diffraction limit ($\lambda/3$ as explained previously). The frequency used for the diffraction limit was 240 Hz, which was the highest frequency in the bandwidth that had a relative amplitude of 10% compared to the highest

spectral contribution. As expected, the length of the scatterer-like path diversions affected the FWHM, with longer path diversions leading to improved resolution.

Table A-1 Length of path-diverting scatterers compared to the full-width at half maximum (FWHM) for the spatial extent of the focusing, shown with respect to smallest wavelength as well as with respect to the diffraction limit.

Length of Path-Diverting Scatterers (cm)	FWHM with Respect to Wavelength (λ)	FWHM with Respect to Diffraction Limit
0	λ/2.7	0.9 × better
5.08	λ/7.2	2.4 × better
10.16	λ/8.9	3.0 × better
15.24	λ/12.9	4.3 × better
30.48	λ/19.1	6.4 × better

Figure A-4 shows the full spatial measurements of the control experiment and the experiment with 30.48 cm path diversions, which are the two most extreme cases in this study. Even though the measurement resolution is not high enough to sample multiple points of the main peak when using the largest path diversions, the main peak is nonetheless well within the main peak of the control case. This tight focus clearly shows that using only the in-plane distance produces a significant resolution improvement.

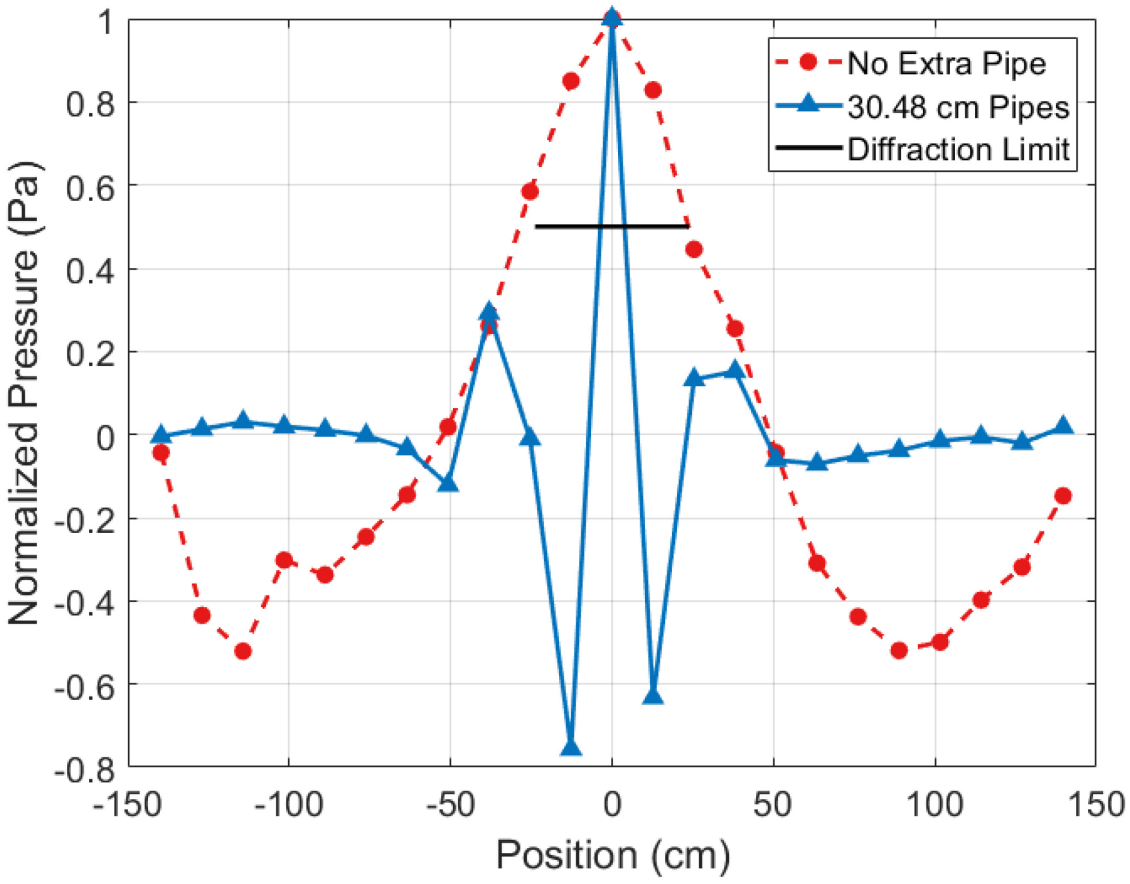

Figure A-4 Spatial plots of the pressure during time reversal focusing along the center pipe of the system, for the control experiment and the 30.48 cm path diversion experiment. The diffraction limit (λ/3) is shown for reference. The control experiment is considered diffraction limited. With the 30.48 cm path diversions, focusing is around 1/6 the diffraction limit (λ/19).

To explain the improved resolution due to the added path lengths, spectral information from the backward TR step was used to simulate the backward step. The path-diverting scatterers add length between the spatial measurement locations, and this effectively spreads out the measurement locations when path diversions are present. This spectrum of the simulation was obtained by taking the average of the magnitude of the spectra for all measurements. These average spectral amplitudes, $\overline{A_f}$, were then used to create a simulated focus spatial distribution, $y_{simulated}$, based on a superposition of cosine waves as shown in Eq. A-1.

$$y_{simulated}(x_{trunk}) = \sum_{f} \overline{A_f} \cos\left(\frac{2\pi f}{c}(x_{trunk} + N * L)\right), \quad \text{(A-1)}$$

where f is frequency, x_{trunk} is the horizontal position along the main trunk relative to the focus position, c is the speed of sound, and $N * L$ is the total length travelled through all intervening diversions, calculated by multiplying the length of an individual diversion by the number of diversions between the focus position and x_{trunk}. The cosine wave simplifies the summation by making all frequencies constructively interfere at $x = 0$.

This simulated focus spatial distribution, $y_{simulated}$, was then plotted in comparison to the experimental focus spatial distribution, and the process was repeated for each length of path-diverting scatterers. Figure A-5 shows the simulated focus in comparison to the experimental focus for the 30.48 cm path diversions.

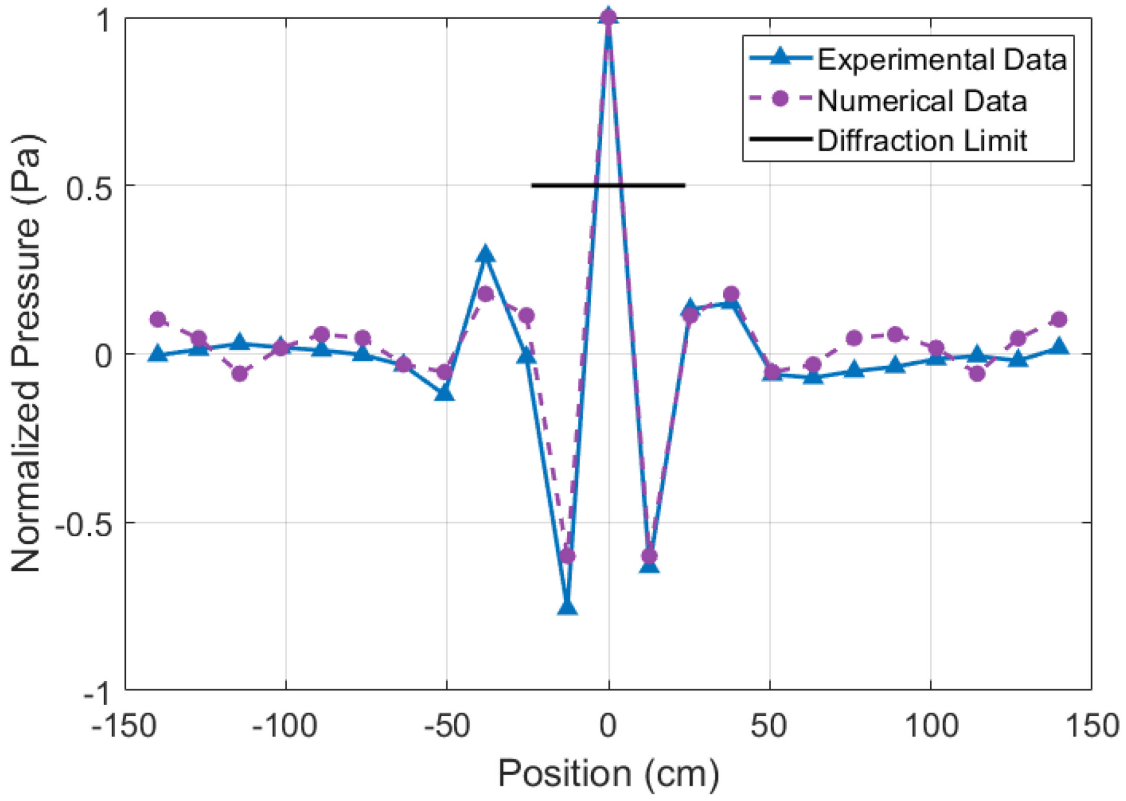

Figure A-5 Spatial focusing of 30.48 cm path-diverting scatterers, for the experimental and simulated data. The diffraction limit (λ/3) is shown for reference.

Significantly, the simulation is most accurate near the focus, where the frequency content is similar, including the size of the FWHM. This indicates that the simulation provides a reasonably accurate estimation of the experimental results that can be obtained if one were considering adding in path-diverting scatterers of a selected size. After the simulated data was created for each length of path-diverting scatterers, the FWHM was calculated for the experimental and simulated data corresponding to each length of path diversion (see Fig. A-6). As shown, all lengths of path-diverting scatterers included in the experiments and simulations provided super resolution, with the simulated data consistently having worse resolution than the experimental

data. As expected, as the path diversions are made to be longer, the effective wave speed is decreased, and this leads to a smaller FWHM.

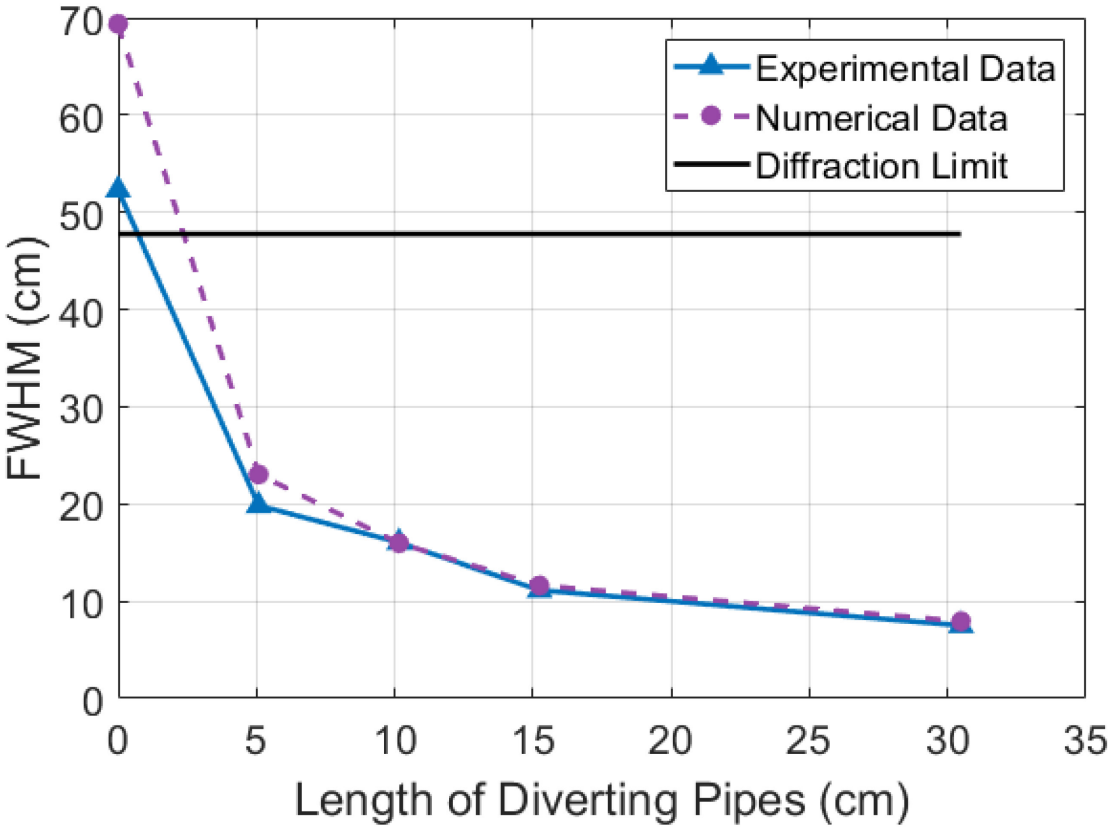

Figure A-6 Comparison of the length of diverting pipes with the FWHM measurements for both experiment and simulation data.

A.4 Scattering Network

The path diversions provided by the pipes demonstrate the proof of concept that waves may be effectively slowed down in the region of the intended TR focusing to reduce the effective wavelength of the focused waves. The pipe experiments utilize dramatic and perhaps impractical means of slowing down the waves. A network of scatterers that force incident waves to contort, diffract, and scatter around the balls to slow down the waves is one potential method to

implement this path diversion method in a 3-D scenario. From a geometrical standpoint, if the waves are treated as rays that diffract around an individual ball, they would have to travel at least halfway around the ball circumference to the other side of an individual ball instead of traveling a distance of the ball diameter, d, if the ball was not present. This means the waves might travel as most an extra path length of $\pi d/2 - d = 0.57d$ or 57% distance. However, the wavelengths employed in the experiment range from 2.7 to 35 times larger than each ball diameter so the diffracting ray approximation has limited applicability.

A network of one-thousand, 25.0 mm diameter aluminum balls (10×10×10 balls) was constructed to determine whether a resolution improvement may be obtained relative to the ball network not being present. Two common packing arrangements for the balls were considered, face-centered cubic (FCC) and hexagonal close-packing (HCP). Both achieve the highest packing density possible for a regular lattice arrangement but HCP was selected since only this packing arrangement allows for a continuous hole along one of the axes of the lattice. This hole allows for a small microphone to be dragged through the lattice and sample the acoustic field within the scattering network lattice of balls. The balls were machined to have an axial hole in them so that 10 of them could be held in a vertical line with a rod running through the axial holes in the balls. A framework was built to hold rods in the HCP arrangement and 1,000 balls were placed on 100 rods in this framework. See Fig. A-7(a) for a photograph of the ball network held together in the framework. In Fig. A-7(b) one face of the ball network is shown with an approximately 3.2 mm (1/8 inch) diameter hole through the lattice visible. A GRAS 46DE microphone, with a diameter of 3.2 mm was used to measure the sound field along one of the holes in the lattice. To prevent sound from directly entering the hole through the lattice that the

microphone would measure in, one end of the hole was plugged with putty. The microphone was placed at the end of a tube that had an inside diameter just smaller than the grid cap but just larger that the microphone housing and cable. Thus, the microphone element was at the end of a long tube, shown inserted into the lattice hole in Fig. A-7(a). This tube blocked sound from entering the lattice hole opposite to the opening blocked by the putty.

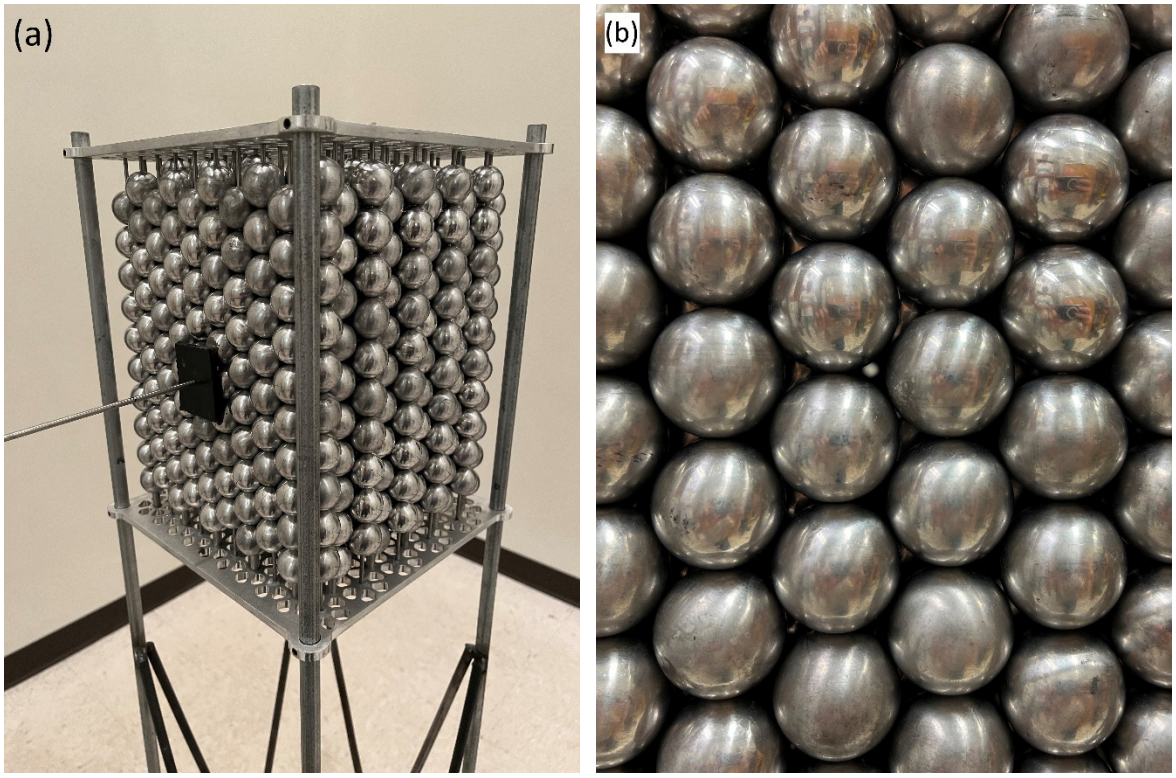

Figure A-7 Photographs of the network of 1,000 balls. (a) A tube is inserted horizontally from the left. The framework holding the balls in place is visible. (b) Close-up view of the balls from one side. A small hole all the way through the lattice is visible in the center of the photograph.

The tube holding the microphone was mounted to a translation stage positioning system. The microphone was inserted so that the microphone element was in the middle of the ball lattice. Eight Mackie HR824mk2 loudspeakers were used as sources and one by one an IR was obtained between each loudspeaker and the microphone. The loudspeakers were placed on stands

in a reverberation chamber at Brigham Young University with a volume of 204 m^3, a reverberation time of 6.9 s and a Schroeder frequency of 385 Hz. The loudspeakers were not placed near the ball lattice. The bandwidth used for these IRs was from 100 Hz to 10 kHz, but the signal to noise ratio was best (>30 dB) between 300 Hz and 5300 Hz. Once the IRs were measured and reversed in time, the reversed IRs were broadcast simultaneously from the loudspeakers, producing a TR focus in the middle of the lattice. The TR focusing was repeated many times as the microphone sampled the sound field over a 60 cm span with a 0.5 cm spacing between measurement positions. For the middle 21 cm of the span, the microphone sampled the sound field within the hole through the lattice. The entire experiment was repeated at the same locations but with the ball lattice removed such that the TR focusing would not occur near any reflecting objects.

In the post processing phase, the data was band-pass filtered in 500 Hz segments with starting frequencies of 300 Hz up to 4800 Hz (producing bandwidths of 300-800 Hz, 800-1300 Hz, 1300-1800 Hz, etc. up to the last bandwidth of 4800-5300 Hz). The spatial extent of the TR focusing for each bandwidth was plotted at the time of maximum focusing and the FWHM was determined. Figure A-8 displays the FWHM for each of the bandwidths when focusing within the ball lattice and without the ball lattice being present. The spatial extent of the focusing over the bandwidth being considered was plotted and the FWHM was determined from an interpolated version of the spatial extent plot. The FWHM extracted is then converted to a fractional number of wavelengths using the highest frequency within the given 500 Hz bandwidth. There is a clear improvement in the FWHM with the ball lattice present in that the spatial extent of the focusing is reduced when focusing inside the ball lattice.

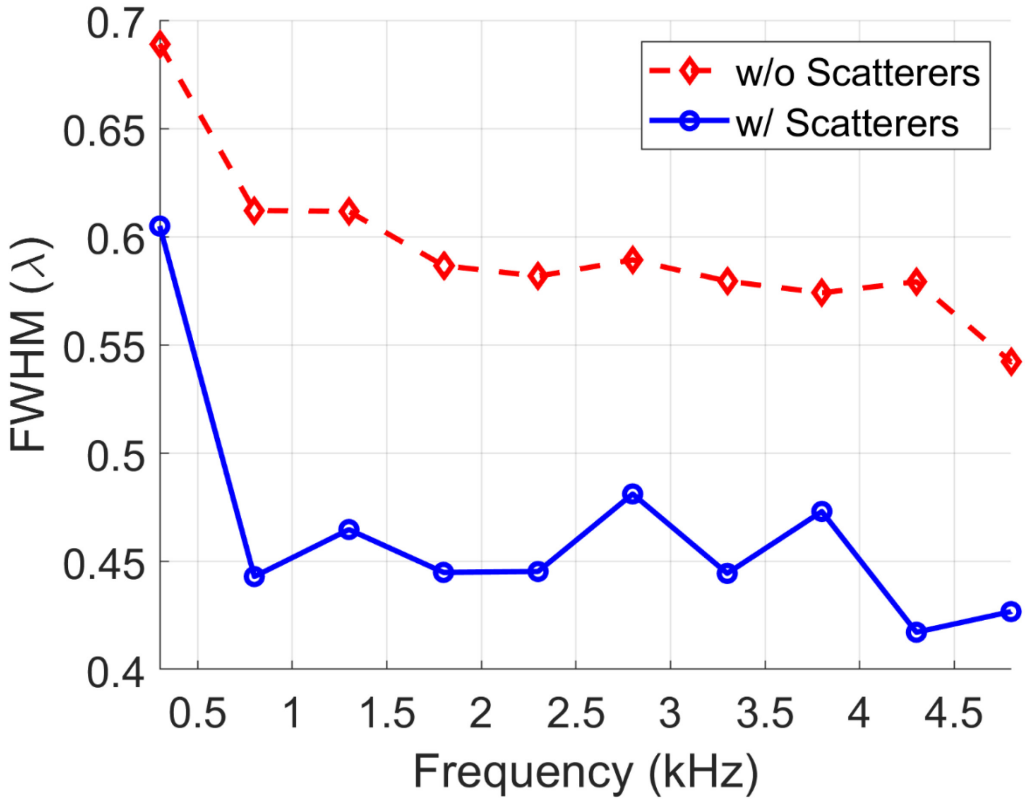

Figure A-8 Comparison of the FWHM measurements for waves focused in the room away from any reflecting boundaries and not within the ball lattice (w/o Scatterers) to waves focused within the lattice at the same location within the room (w/ Scatterers).

It is debatable whether the focusing inside the ball lattice has beaten the diffraction limit or not. Often authors claim that if the FWHM is less than a half wavelength that the diffraction limit has been broken. However, especially in the field of optics, the diffraction limit is defined in terms of the available aperture used. A FWHM of a half wavelength is only possible if a complete, perfect, aperture is available, and even then, the FWHM of the main peak in the focusing is often larger than a half wavelength due to the point spread function of the focusing. In the present case, the FWHM at 1.5 kHz and above, without the ball lattice present, is about 0.6 times the wavelength and with the number of sources used and the long length of the reversed

IRs used, the spatial extent of the focusing should be as good as it can be without doing something like introducing scatterers into the near field of the focusing. The FWHM with the ball lattice present is generally a half wavelength at 2 kHz and above and so because the FWHM is less, one may argue that the diffraction limit has been broken relative to the case with no ball lattice present. However, one may also argue that the ball lattice has changed the aperture in such a way that the focusing can really only occur along one dimension, the dimension of the hole through the lattice. The diffraction limit in one dimension is a half wavelength, so one could argue that while the ball lattice does improve the resolution with respect to not having the ball lattice present, the diffraction limit has not been broken because the aperture has changed with the ball lattice present since the focusing occurs mainly in one dimension.

A.5 Conclusion

This research has shown that super resolution can be achieved using time reversal (TR) with scatterer-like path diversions. As waves are forced to divert around scatterers, the effective wave speed in the medium decreases, resulting in smaller effective wavelengths, and therefore improved resolution. The width of the peak depends on the length of the path diversions, with a longer path diversion corresponding to a narrower focus peak. This experiment showed super resolution up to 1/6.4 the diffraction limit ($\lambda/19$ resolution), using 61 cm path diversions placed between each measurement location that were spaced 12.7 cm apart. Super resolution was also observed even with 10.1 cm path diversions, although this resolution was only 1/3 the diffraction limit ($\lambda/8.9$ resolution). Simulations were shown to agree with these data, which proves that the

path diversions simply increase the distance between measurement locations and thereby decreases the effective wave speed.

It is important to note that, although the results of this experiment show improved spatial focusing resolution, the one-dimensional nature of the experiment limits the direct application of these results in two- and three-dimension TR experiments. Further research is needed to explore these effects in multiple dimensions. This chapter has, however, shown that the concepts behind the use of scatterers to achieve super resolution via slowing down the effective wave speed as waves divert around scatterers are sound and may be a viable alternative to using resonators and other objects in the near field. If path-diverting scatterers are not possible or desirable to use, scattering objects of larger size should yield the same effects.

The results of this research suggest that it may be possible for scatterers to provide super resolution in TR. Previous research focused on the use of resonators or absorbers to enable super resolution, but it has now been demonstrated that scatterers may be used. This would be beneficial to acoustic focusing research and applications by providing another method to improve resolution, which may be a better option in some situations.

Appendix B

Design of an underwater acoustics lab

Cameron Vongsawad was a graduate student that was primary responsible for designing and testing an underwater acoustics lab being built at Brigham Young University. This author was involved in the design and creation of software for controlling the data acquisition system and robotic arms. This appendix is an article that was published as C. T. Vongsawad, T. B. Neilsen, A. D. Kingsley, J. E. Ellsworth, B. E. Anderson, K. N. Terry, C. E. Dobbs, S. E. Hollingsworth, and G. H. Fronk, "Design of an underwater acoustics lab," *Proc. Mtgs. Acoust.* **45**, 070005 (2021); https://doi.org/10.1121/2.0001540. It is reprinted in this dissertation under the terms of ASA's Transfer of Copyright Agreement, item 3. I hereby confirm that the use of this article is compliant with all publishing agreements.

Volume 45 http://acousticalsociety.org/

181st Meeting of the Acoustical Society of America

Seattle, Washington

29 November - 3 December 2021

Underwater Acoustics: Paper 2aCA10

Design of an underwater acoustics lab

Cameron T. Vongsawad, Tracianne B. Neilsen, Adam D. Kingsley, John E. Ellsworth, Brian E. Anderson, Kaylyn N. Terry, Corey E. Dobbs, Scott E. Hollingsworth and Gabriel H. Fronk

Department of Physics and Astronomy, Brigham Young University, Provo, UT, 84602; cvongsawad@gmail.com; tbn@byu.edu;tbnbyu@gmail.com; adamkingsley@gmail.com, jee@byu.edu, bea@byu.edu, knterry@gmail.com, coreydobbs205@gmail.com, scottphollingsworth@gmail.com, gherrickfronk@gmail.com

A new underwater acoustics laboratory has been created at Brigham Young University. Care was taken to design the lab that can take high precision measurements and yet provide an optimal environment for training undergraduate student researchers. The laboratory water tank is a rectangular acrylic tank of 3.6 m long by 1.2 m wide with 0.91 m as the maximum depth. This paper provides details about the custom-built water treatment and sanitizer with bubble removal column. The measurement chain for signal transmission and recording and the automated positioning system are explained. Sound absorbing tiles acquired to line the side walls are also described. The *in situ* calibration method for obtaining a through-the-sensor frequency response of the entire measurement chain is presented. Limitations are mentioned along with a discussion of how this design maintains potential for a wide variety of underwater acoustic laboratory measurements.

Published by the Acoustical Society of America

 https://doi.org/10.1121/2.0001540

1. INTRODUCTION

The Underwater Acoustics Laboratory at Brigham Young University (BYU) was designed and constructed during the years 2019-2021 to facilitate high quality research. Because of the priority on mentored undergraduate student research at BYU, each component was selected with considerations for high levels of safety, automation, and reliability. These features give students the opportunity to learn to perform effective acoustical measurements and data analysis in a mentored environment. More about the mentored environment can be found in the paper Vongsawad, *et al.*[1] submitted to The Journal of the Acoustical Society of America's Special Issue on Education in Acoustics. That paper focuses on mentoring and does not go into the details about the measurement system; the purpose of the current proceedings paper is to provide those details and a description of the through-the-sensor calibration process.

In addition to providing opportunities to train students, this lab provides a way to test algorithms that can be applied to open-water data. Obtaining large open-water data sets for underwater acoustics research and validating measurements[2–4] has high economic and temporal costs. A laboratory system saves on those costs,[5] especially for researchers without ease of access to large bodies of water.[6,7] Open-water tests are often noisy and unpredictable with ever changing environmental concerns, but the tank allows for better control of the environment.[7] Measurement automation allows data to be collected quickly and efficiently, with high precision.

This paper provides details about the water tank, water treatment and sanitizer system, anechoic panels, signal transmission and data acquisition, and the automated positioning system. The *in situ* calibration method for obtaining a through-the-sensor frequency response of the entire measurement chain is also presented. In conclusion, a few limitations of this experimental setup are mentioned along with a discussion of how this design maintains potential for a wide variety of underwater acoustic laboratory measurements.

2. EXPERIMENTAL SETUP

The open-air rectangular parallelepiped water tank, shown in Fig. 1, was made by Engineering Laboratory Design Inc. (Lake City, Minnesota, USA) and is constructed of scratch resistance acrylic panels that are solvent-welded together, with a steel frame on adjustable leveling pads. The tank material, acrylic, was also chosen for its visual transparency and non-corrosive nature. Acoustical reflections from these walls are reduced compared to tanks made of steel, concrete, or glass since the acoustic impedance of acrylic is closer to that of water than those other materials.[5] (Values for lucite are found in Kinsler & Frey on p. 256.) The tank's dimensions were chosen to allow scaled acoustical measurements, similar to work in Refs. [3–5,8–10] and designed to maximize usable laboratory space. The 3.66 m long by 1.22 m wide rectangular tank has a maximum water depth of 0.91 m, corresponding to a maximum fill volume of 4077.6 liters.

A. WATER TREATMENT

Water quality is maintained by a system that provides for filtration, sanitization, temperature control, and bubble reduction. Acoustic disturbances caused by thru wall plumbing penetrations of the tank are avoided by siphoning water out of the tank over the wall and returning it after treatment over the wall. The pickup (inlet) and return (outlet) siphon pipes are removable so the filtration system can be separated from the tank entirely. Bubble prevention is accomplished by exposing water returning to the tank to a low pressure in the vertical column. Dissolved air and small bubbles expand and float to the top of the column and are removed. Control of pumps, valves, and heating is automated using a programmable logic controller (PLC). A piping diagram of the system is shown in Fig. 2a with water components depicted in blue and air control components in green. Water flow in the diagram is left to right. A photo of the treatment system is provided in Fig. 2b with letters indicating the different parts. The system incorporates a water pump (W), a micron

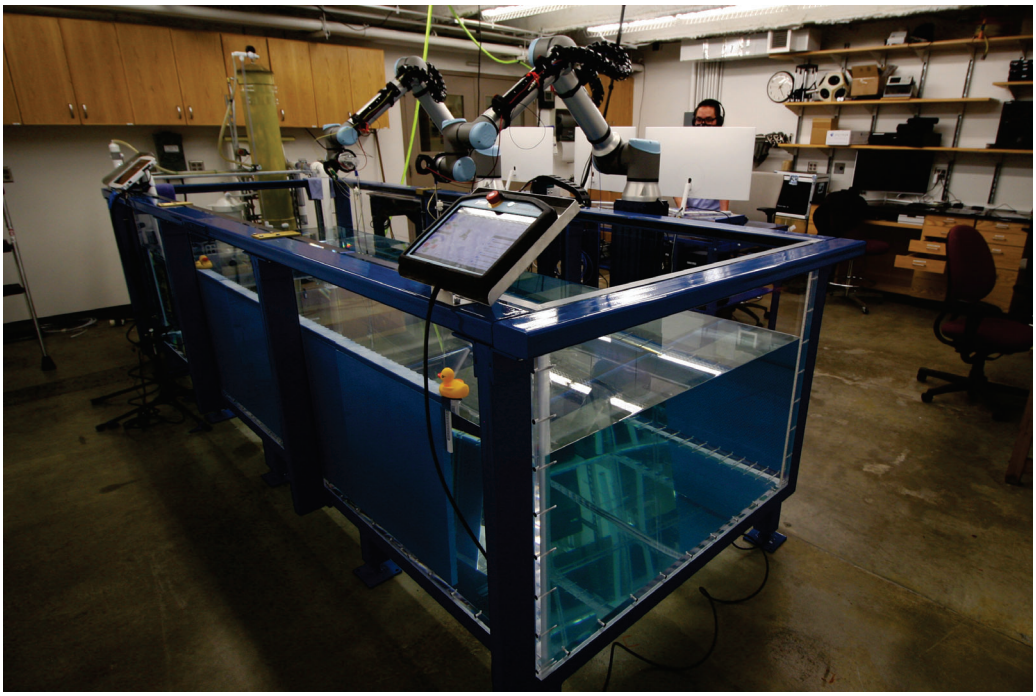

Figure 1: BYU's acrylic water tank and robotic positioning system.

bag filter (Q), a water heater, an ultraviolet light water sanitizer, an ozone generator (behind the controls cabinet V). Bubble prevention is provided by a vacuum pump (J) that removes air from all components of the water path using three solenoid valves (G and M), three manual flow rate valves (H), a check valve (I), and drain line (K). Three vent valves are provided for inputting air where needed to adjust water levels (F). Four capacitance water level detectors are used, one on each of the inlet (U) and outlet (E) sight glasses and two (C and D) on the bubble removal column (B). Temperature is monitored by a J-type thermocouple probe (S) positioned at the water inlet. Pipe unions for connecting and removing the siphon inlet (O) and return pipe are installed to be close to the tank. A sight glass (L) and a compound pressure gauge (A) are used for setting up water levels when installing the filtration system. The pressure gauge (N) is used to monitor the condition of the filter. The electronics, PLC, and control display panel (R) are housed in a watertight cabinet (V). The system is powered by three-phase 208 AC and equipped with a ground fault interrupter (T). A requisite emergency stop button (P) is provided above the control system.

To allow ease of both draining and filling, a valve is located in one corner of the bottom sheet of acrylic, with a direct line split to either a drain or water faucet. The valve can be capped with a flat acrylic insert to eliminate unnecessary scattering. The insert has an embedded iron piece for easy removal with a magnet. Tap water is used to fill the tank, with the water level replenished using distilled water as gradual evaporation occurs in order to maintain control over the water properties and thus the speed of sound. Distilled water replaces the evaporated water without introducing increased calcium hardness or other changes to water properties. Since distilled water is mineral depleted, the tank is never filled entirely with distilled water which is highly corrosive, especially to metals such as those associated with the body of some underwater transducers and the transducer mounts.

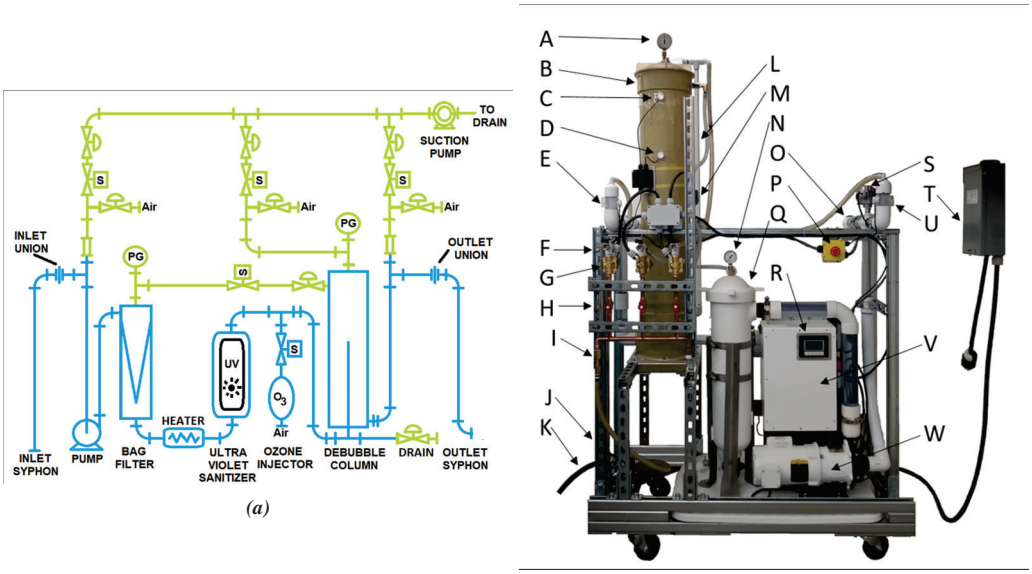

(a) *(b)*

Figure 2: (a) Piping and instrument diagram of the filter and sanitation system with water control components in blue and air control components in green. (b) Water filtration and sanitation engine, front view. See text for a description of the components corresponding with the alphabetic labels.

B. ABSORPTIVE PANELS

To reduce the reflections from the side walls, panels of attenuating material (polyurethane) are used. The attenuating material from Precision Acoustics was chosen to reduce side-wall reflections especially for ultrasonic frequencies. The 50 mm thick, 60 cm tall, square Apltile SF5048 panels, shown in Fig. 3, are optimized for 20-200 kHz and advertise an echo reduction greater than 30 dB. Initial investigations into how lining the tank walls with these panels reduces the reverberation time and the spatially averaged absorption are presented in Ch. 4 of Ref. 11.

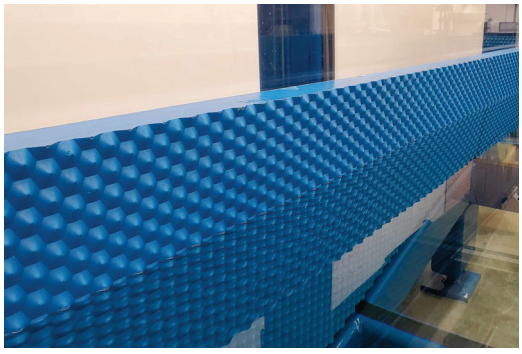

Figure 3: Apltile SF5048 anechoic panels, made by Precision Acoustics.

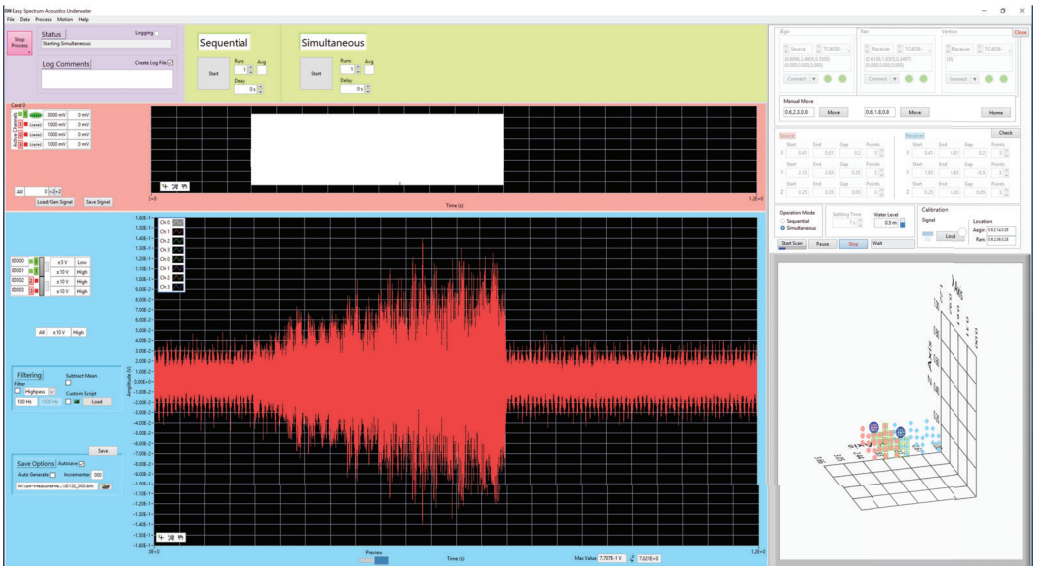

Figure 4: The ESAU interface: custom LabVIEW software used for signal generation (pink box) and data acquisition (blue box), and sensor positioning using the UR10e robotic arms (right side).

C. DATA ACQUISITION SYSTEM

Sensor positioning, signal generation, and data acquisition are controlled via custom LabVIEW software, referred to as Easy Spectrum Acoustics Underwater, or ESAU, whose interface is shown in Fig. 4. ESAU, created by author ADK, facilitates user communication with the Spectrum data acquisition cards and the UR10e robotic arms. The data acquisition cards have relatively high resolution (16-bit) and high sampling rate (40 MS/s). Using the Star-Hub module, the arbitrary waveform generator (AWG) (M2p.6546-x4) and digitizer (M2p.5932-x4) cards are accurately synchronized while housed inside an external PCIe chassis. As implemented, the shared memory allows for 128 mega samples for each of the four input and four output channels. The chassis are seen in the center of the lower shelf in Fig. 8.

D. POSITIONING SYSTEM

The three-dimensional positioning system uses two UR10e collaborative robots from Universal-Robots (universal-robots.com), with one on a Vention (vention.io) 7th axis extender track. The robots, shown in Fig. 5, were chosen for their intuitive programming language, high level of programmable safety, and 0.01 mm precision for repeatability. Each robot operates using six axes of motion and has a maximum reach of 1.3 m. Both robots are mounted level with the top of the tank: one on a simple pedestal and the other on the Vention 7th-axis extender track with a rack and pinion motor providing an additional 1.4 m reach along the length of the tank. The extender track (shown in Fig. 6) has an added positioning error of ±0.01 mm. The Universal-Robots website contains an interactive online academy which allows students to learn robot functionality, safety, and programming in a quick, simple, and thorough way.

Several sources of uncertainty arise in our positioning system. One of them is that the two robots have independent positioning systems oriented with respect to their respective bases. In selecting measurement locations, we need a single coordinate system oriented on one corner of the tank. Conversion from the robot coordinates to the tank coordinate system adds uncertainty to the UR10e 0.01 mm precision. Attachments to

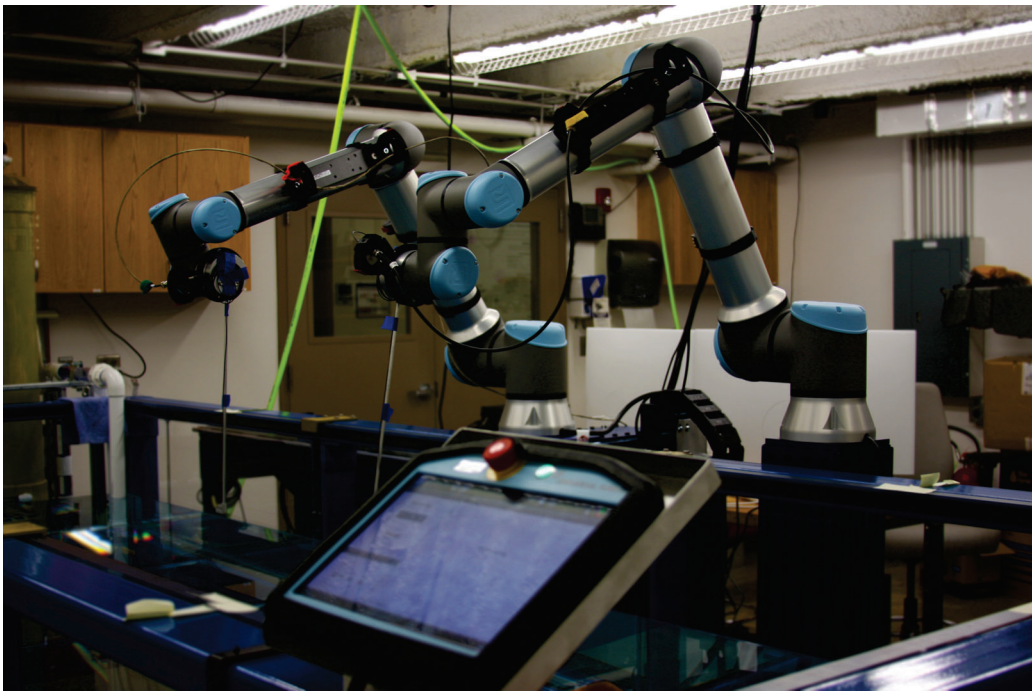

Figure 5: UR10e collaborative industrial robots for positioning sensors with teach pendant (for manual control) in the foreground.

the robotic arms also provide another source of positioning uncertainty. Because these sources of uncertainty are constant, they do not affect repeatability. For two repeated measurements, the positions are the same to ±0.01 mm. Another way this precision can be achieved is by using the distance between two positions acquired by the same robotic arm. Efforts are being made to reduce the added uncertainty in the absolute position relative to the tank coordinates as much as possible and to ensure that we properly account for the propagation of these uncertainties into measurements when necessary.

Several UR10e features are important to ensure safety, especially when new students are being trained. First, each robot has a pre-installed emergency stop button that can be pushed at any time to immediately stop and lock the robot. In addition, the robots have been wired together so that stopping one also stops the other. The desired operational range of each robot is programmed in using a teach pendant—the device used to interact directly with the robots—to define boundary planes. The robot does not exceed these boundary planes as it moves to a requested position, which is important to ensure no part of the robot hits the walls of the tank. The robots have a force tolerance that engages the brakes as well. We have added an additional safety feature to our robots to ensure that they are not accidentally moved into the water; each one has a FS25-C111 float switch from SMD Fluid Controls that will send a stop signal if the float switch touches the water. The float switch is shown in Fig. 7a approximately 7 cm below the end of the robot.

Transducers may be attached to the UR10e in any orientation via custom-designed mounts, referred to as tools. Each transducer has a custom attachment on a thin rod extended from the robot (Fig. 7a) to maintain orientation of the transducers and protect the robot from water damage. This feature allows for more flexibility than traditional two or three axis positioning systems while maintaining similar precision.[9,10]

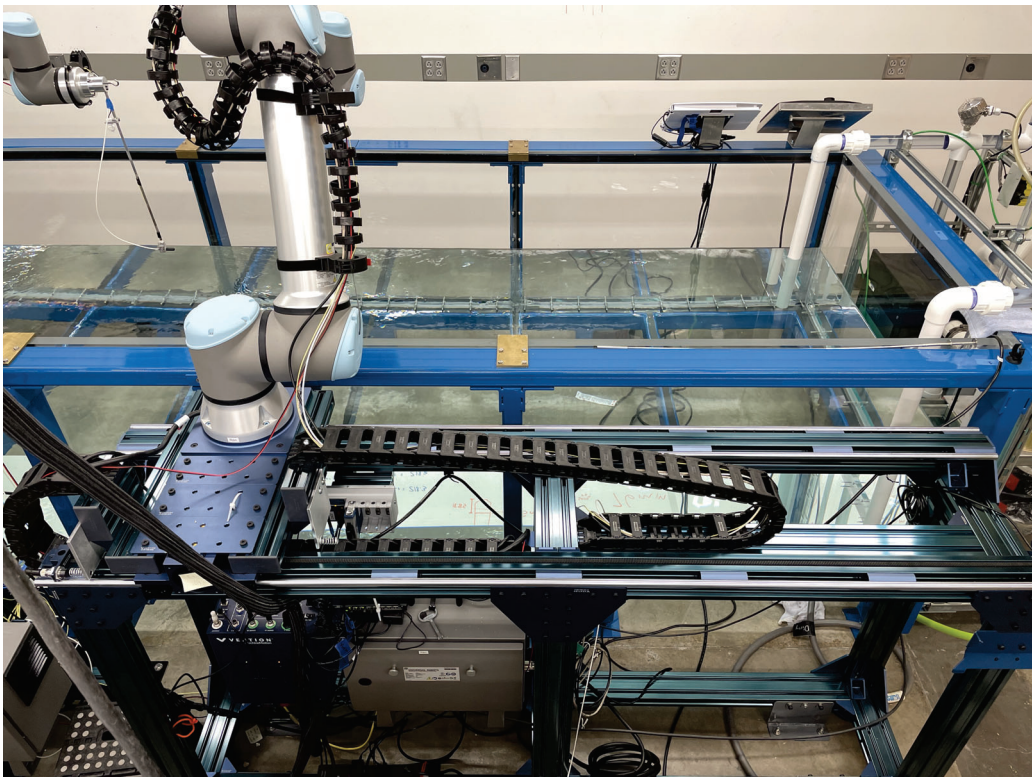

Figure 6: UR10e collaborative industrial robot on the Vention 7th axis extender

The custom transducer mounts allow for multiple configurations including an added wire PTFE/FEP Tip Probe (K-37X-T) thermocouple from ThermoWorks (shown in Fig. 7b at the end of the yellow wire) to measure temperature[2] without significant increased scattering. Conditions are also monitored with SensorsOne LMP 307T temperature and pressure/depth sensors from MCT RAM (mctram.com), rated for 0-86°F and up to 250 m depth. These sensors can be attached to the tank walls using magnets, as shown in in Fig. 7c. The output from two of these sensors are monitored continuously using an NI USB-TC01 boxes and LabVIEW software.

The automated positioning is controlled through TCP/IP by custom LabVIEW software (Fig. 4) used for the data acquisition. Users input coordinates or grids of coordinates in the LabVIEW software, ESAU; if the requested locations fit within defined safety limits, the locations are sequentially sent to the robot and a recording is made at each location. Each robot's software then interpolates between available robot arm/tool orientations to maintain consistent orientation relative to the transducer directivity.

E. MEASUREMENT CHAIN

The automated measurement system can be used with a variety of transducers for transmitting and receiving sound. The frequency range of interest is the primary factor in determining which transducers to use. Currently, we use Brüel Kjær 8103 for the 0.1 Hz - 100 kHz band and Teledyne Reson TC4038 for the 100 kHz - 500 kHz band. These sensors are used for both transmitting and receiving due to their reciprocity,

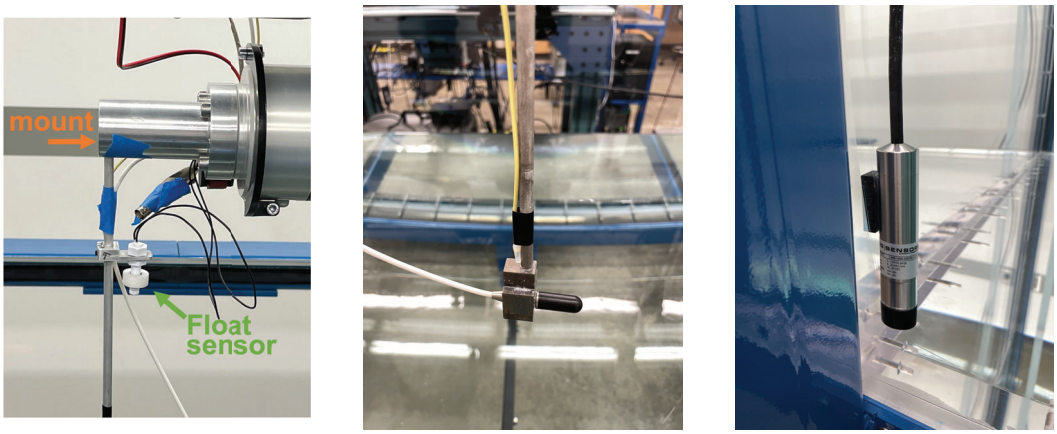

(a) *(b)* *(c)*

Figure 7: (a) Custom mount on the UR10e with a white FS25-C111 float sensor. (b) A B&K 8103 hydrophone and K-37X-T thermocouple. (c) SensorsOne LMP 307T temperature and pressure/depth sensor from MCT RAM.

omnidirectionality, and relatively flat frequency response over the specified bands.

The transmitting transducer receives the output signal from the arbitrary waveform generator (AWG) passed through a power amplifier (TEGAM Model 2350). The TEGAM allows a maximum of 4 Vpp input before clipping and provides a gain of x50. For frequencies above 10 kHz,[12] the TEGAM output is passed through a transformer fabricated to address the impedance mismatch often found between an amplifier and a piezoelectric source.[7] Two of these TEGAM power amplifiers are shown on the left side of the lower shelf in Fig. 8.

The receiving transducers are connected to a conditioner. Signals from the B&K 8103 are passed through a B&K signal conditioner. Signals from the TC4038 are passed through Teledyne Marine Reson VP2000 EC6081 mk2 preamplifiers, as described in Ref. [13]. These signal conditioners sit on the main desk in Fig. 8, under the monitors. The conditioned voltage signals are then sent to the Spectrum digitizer cards, described above.

The cables connecting transducers to the data acquisition system run along the length of the robotic arms and require special consideration of shielding to reduce the potential for induced noise from robot motors and brakes. These cables are contained in a cable management system to prevent cables from entering the water or becoming entangled. All of these cables and electrical equipment are kept on one side of the tank to provide organization and maintain a clear location for maintenance to be completed while minimizing potential water damage, as described in Appendix C of Ref. [11].

3. THROUGH-THE-SENSOR CALIBRATION

Because each component of the measurement chain has a different frequency response, a through-the-sensor calibration method is used. Using a closely spaced transmitter and receiver pair, a recorded chirp is processed via cross correlation to obtain the impulse response of the system.[14,15] The procedure used here uses techniques in room acoustics and is similar to the procedure in Ref. 16, except that they were doing source characterization and we are obtaining the frequency response of the measurement chain with minimal propagation effects.

In practice, the frequency response of the measurement chain includes the effects of the response of the

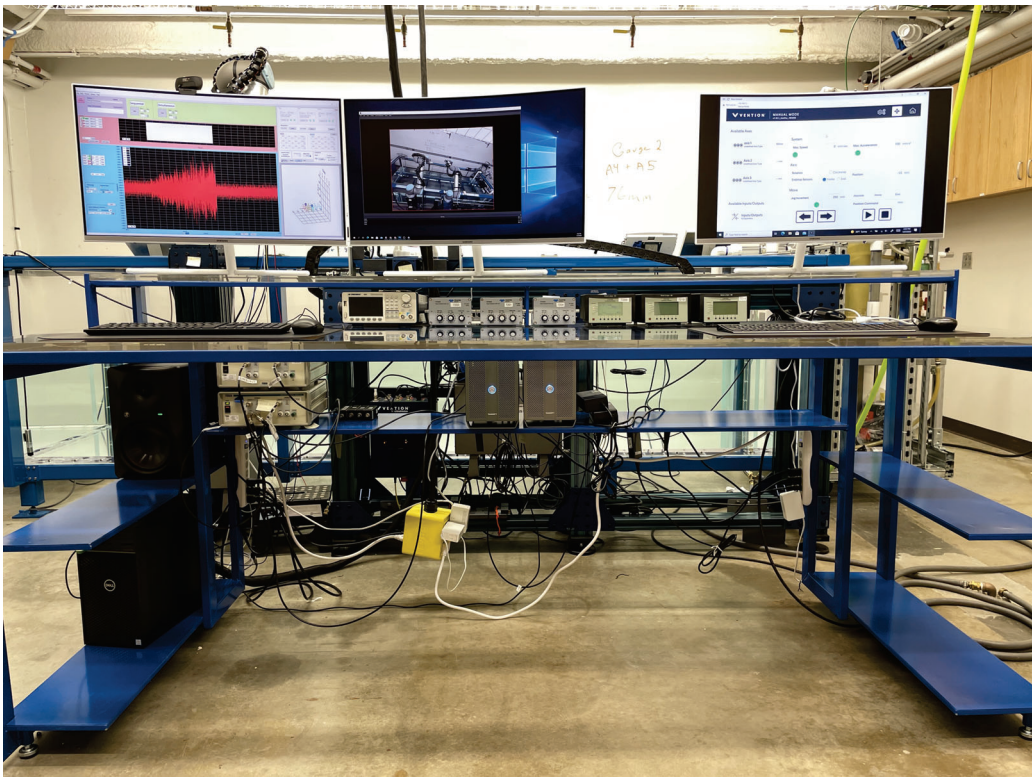

Figure 8: Computers and transducers used in the measurement chain. The ESAU interface is on the left screen; video feed from cameras in the lab are on the middle screen; and the interface for manual control of the Vention 7th axis-extender is on the right screen. Under the monitors but on top of the desk are the pre-amplifiers and signal conditioners. On the shelf below the desk, two TEGAM power amplifiers are on the left, next to the speaker, and the two chassis holding the Spectrum input and output cards are on the right.

transducers, including Digital to Analog (D-A) and Analog to Digital (A-D) components on the signal. The contribution of these components to the frequency response can ideally be accounted for by application of individual calibrated responses of each component of the measurement chain (shown in Fig. 8). Alternately, the contribution of all components may be accounted for by understanding the total through-the-sensor (TTS) response.[6,9,17–19] The technique for obtaining the TTS response relies on an *in situ* calibration to obtain the impulse response for the measurement system. This TTS response, $h_{\mathrm{TTS}}(t)$, can be obtained from the calibration measurement via the deconvolution method and then used as a filter (in deconvolution) on subsequent measurements to remove $h_{\mathrm{TTS}}(t)$ and obtain the impulse response, $h(t)$, corresponding to sound propagation in the water tank.[16]

The first step to obtaining the TTS response is taking a calibration measurement, where source and receiver are positioned close enough that transmission losses due to sound propagation are reduced significantly and reflections are easily removed. The small transmission losses during these calibration measurements are assumed negligible in this study; however, a phase adjustment accounting for the small propagation distance is applied. The small distance must be chosen with care and large compared to a wavelength for the frequency bandwidth of interest. Otherwise, potential near-field effects must be noted.

The calibration signal is a swept-sine signal, spanning the bandwidth of interest, which is broadcast and recorded. A chirp, spanning the frequencies of interest, is used as the calibration signal because long-duration swept-sine signals (chirps) provide the best signal-to-noise ratio for broadband measurements[6, 10, 16–18] compared with white noise, pulses,[20] or short swept-sine signals with averaging. This calibration measurement is interpreted through the deconvolution method (described below), and the resulting impulse response is time-gated for removal of all reflections in order to estimate the response of the measurement chain. This TTS calibration thus incorporates the unit-less sensitivities of all unknown components.[6, 10, 16] Application of this response to a subsequent measurement yields a calibrated measured response in Volts (which may be converted to μPa when a transducer sensitivity is applied in the preamplifier settings or directly to the data).

The impulse response obtained through frequency deconvolution[6, 17, 18] of the calibration measurement is time-gated using a half-Hanning window, with the time chosen to remove all reflections. The whole D-A and A-D measurement chain frequency response $H_{\mathrm{TTS}}(f)$ can then be obtained by applying a fast Fourier transform (FFT) on the windowed, time-gated response $h_{\mathrm{TTS}}(t)$.

After the TTS response $h_{\mathrm{TTS}}(t)$ is obtained from the calibration measurement, it can be applied to the received signal $r(t)$ to estimate the impulse response of the sound propagation in the environment, $h(t)$, may be found for subsequent measurements. For a generated signal, $g(t)$, the received signal, $r(t)$, is

$$r(t) = h(t) * h_{\mathrm{TTS}}(t) * g(t), \tag{1}$$

where h_{TTS} is the TTS response applied as a filter.[18] After a Fourier transform and rearranging, the frequency response (also referred to as the transfer function) associated with sound propagation in the tank is

$$H(f) = \frac{R(f)}{H_{\mathrm{TTS}}(f)G(f)}, \tag{2}$$

or by applying Wiener deconvolution to prevent division by zero:

$$H(f) = \frac{[H_{\mathrm{TTS}}(f)G(f)]^* R(f)}{[H_{\mathrm{TTS}}(f)G(f)]^2 + \sigma^2}. \tag{3}$$

An IFFT then yields the impulse response associated with the transfer function of the sound propagation independent of the frequency response of all the components in the measurement chain:

$$h(t) = \mathcal{F}^{-1}[H(f)]. \tag{4}$$

Thus, the frequency-dependent calibrated water-tank response can be obtained *in situ* for any source-receiver position under any propagation conditions. Since acoustic propagation models must adjust for varying conditions such as water temperature gradients,[2] this *in situ* calibration and measurement method provides the ability to obtain large data sets with full acoustic characterization.

4. LIMITATIONS AND IMPROVEMENTS

An open-air water tank of this size has numerous potential applications, however, limitations exist. The side walls, maximum depth and general dimensions limit the source-receiver range of potential scaled experiments.[3, 9, 10] Potential regimes for scaled experiments are also limited by the frequency response of the transducers. The size of transducers, mounts, etc. must be considered when designing the experiment as anything large relative to the wavelengths in the signals of interest have the potential to scatter the sound.

The selected attenuating material, the Apltile SF5048 panels, increases efficiency by reducing the reverberation time and, thus, the needed delay for repeatability between consecutive measurements. The panels,

however, are not 100% anechoic. Though other attenuating treatment options are available for different bandwidths,[3,5,9,10,13,20,21] passive underwater attenuating lining is often optimized for ultrasonic measurements and can be very costly. Multi-layered treatments, wider tanks, and active acoustic absorbers could improve the anechoic nature of the tank but also increase costs. Efforts to quantify the attenuating properties of the panel are ongoing.[11,22]

The positioning system utilizes UR10e robots to effectively scan the majority of the tank with any transducer orientation. A larger tank would allow for longer wavelengths and increased potential applications but require an even more creative solution to the positioning system[6,7] and larger lab space. The positioning could also be improved by having both robots on 7th axis extender tracks or even mounting the robots to a 7th axis extender gantry above the tank to fully reach any position in the tank. The robots also introduce electrical noise as mentioned above, and cabling requires a level of shielding that may be unnecessary with different systems or with lower desired bandwidths.

5. SUMMARY

An underwater acoustics research laboratory has been described with the goals of measuring large datasets efficiently for new research and helping students learn effective experimentation techniques. High priority has been given to measurement systems that are reliable, easy to use, and safe. Considerations that guided the design included the dimensions and materials of the tank, the capabilities of the data acquisition system, and the positioning systems precision. Underwater acoustic attenuating materials (such as the Apltile SF5048) are not likely to be truly anechoic, as defined in airborne anechoic chambers, but can significantly reduce reverberation time. Ultrasonic bandwidths require data acquisition systems that can handle high sampling rates, as well as care for dealing with potential sources of electrical noise in the cables. Robotic arms offer an alternative solution to traditional Cartesian positioning systems with high precision and variability in transducer orientation. Many transducers are available for tank measurements but require consideration of their physical size, as well as bandwidth and potential for needed impedance matching with amplification. To account for the frequency response of the measurement chain a through-the-sensor calibration method is employed. The combination of all of these tasks has opened the way for future underwater acoustics experiments at BYU.

6. ACKNOWLEDGEMENTS

We wish to acknowledge funding for the primary lab equipment from the Office Naval Research, Defense University Research Instrumentation Program N00014-18-S-F007, Grant 12671398.

REFERENCES

[1] C. T. Vongsawad, T. B. Neilsen, K. N. Terry, S. P. Hollingsworth, C. E. Dobbs, and G. H. Fronk, "Creating a mentored research environment in an underwater acoustics lab," The Journal of the Acoustical Society of America **150**(4), A292–A292 (2021) https://doi.org/10.1121/10.0008330 10.1121/10.0008330.

[2] L. T. Rauchenstein, A. Vishnu, X. Li, and Z. D. Deng, "Improving underwater localization accuracy with machine learning," Review of Scientific Instruments **89**(7) (2018) http://dx.doi.org/10.1063/1.5012687 10.1063/1.5012687.

[3] P. Papadakis, M. Taroudakis, F. Sturm, P. Sanchez, and J. P. Sessarego, "Scaled laboratory experiments of shallow water acoustic propagation: Calibration phase," Acta Acustica united with Acustica **94**(5), 676–684 (2008) 10.3813/AAA.918081.

[4] R. A. Hazelwood and S. P. Robinson, "Underwater acoustic power measurements in reverberant fields," in *Oceans 2007 - Europe*, IEEE, Aberdeen (2007), pp. 1–6, https://ieeexplore.ieee.org/document/4302295, 10.1109/OCEANSE.2007.4302295.

[5] D. C. Baumann, J. M. Brendly, D. B. Lafleur, P. L. Kelley, R. L. Hildebrand, and E. I. Sarda, "Techniques for Scaled Underwater Reverberation Measurements," in *Oceans 2019 MTS/IEEE SEATTLE*, IEEE, Seattle, WA, USA (2019), pp. 1–5, https://ieeexplore.ieee.org/document/8962732, 10.23919/OCEANS40490.2019.8962732.

[6] J. L. Kennedy, T. M. Marston, K. Lee, J. L. Lopes, and R. Lim, "A rail system for circular synthetic aperture sonar imaging and acoustic target strength measurements: Design/operation/preliminary results," Review of Scientific Instruments **85**(1) (2014) 10.1063/1.4861353.

[7] N. L. Weinberg and W. G. Grantham, "Development of an Underwater Acoustics Laboratory Course Development of an Underwater Acoustics Laboratory Course *," The Journal of the Acoustical Society of America **49**(3), 697–705 (1971) https://asa.scitation.org/doi/abs/10.1121/1.1912405 10.1121/1.1912405.

[8] L. Zhang and H. L. Swinney, "Sound propagation in a continuously stratified laboratory ocean model," The Journal of the Acoustical Society of America **141**(5), 3186–3189 (2017) http://dx.doi.org/10.1121/1.4983123 10.1121/1.4983123.

[9] J. D. Sagers, "Results from a scale model acoustic propagation experiment over a translationally invariant wedge," Proceedings of Meetings on Acoustics **22**(1) (2015) 10.1121/2.0000003.

[10] J. D. Sagers and M. S. Ballard, "Testing and verification of a scale-model acoustic propagation system," The Journal of the Acoustical Society of America **138**(6), 3576–3585 (2015) 10.1121/1.4936950.

[11] C. T. Vongsawad, "Development and characterization of an underwater acoustics laboratory via *in situ* impedance boundary measurements," Master's thesis, Brigham Young University (2021).

[12] C. B. Wallace and B. E. Anderson, "High-amplitude time reversal focusing of airborne ultrasound to generate a focused nonlinear difference frequency," The Journal of the Acoustical Society of America **150**(2), 1411–1423 (2021).

[13] Z. Deng, M. Weiland, T. Carlson, and M. Brad Eppard, "Design and instrumentation of a measurement and calibration system for an acoustic telemetry system," Sensors **10**(4), 3090–3099 (2010) 10.3390/s100403090.

[14] B. Van Damme, K. Van Den Abeele, Y. Li, and O. B. Matar, "Time reversed acoustics techniques for elastic imaging in reverberant and nonreverberant media: An experimental study of the chaotic cavity transducer concept," Journal of Applied Physics **109**(10) (2011) 10.1063/1.3590163.

[15] B. E. Anderson, M. Clemens, and M. L. Willardson, "The effect of transducer directivity on time reversal focusing," The Journal of the Acoustical Society of America **142**(1), EL95–EL101 (2017) http://dx.doi.org/10.1121/1.4994688 10.1121/1.4994688.

[16] K. L. Gemba and E.-M. Nosal, "Source characterization using recordings made in a reverberant underwater channel," Applied Acoustics **105**, 24–34 (2016).

[17] A. J. Berkhout, D. de Vries, and M. M. Boone, "A new method to acquire impulse responses in concert halls," Journal of the Acoustical Society of America **68**(1), 179–183 (1980) 10.1121/1.384618.

[18] A. Farina, "Advancements in impulse response measurements by sine sweeps," in *Audio Engineering Society - 122nd Audio Engineering Society Convention 2007*, May 2007, Audio Engineering Society, Vienna, Austria (2007).

[19] G. D. Curtis, "Wide-frequency response of type J-9 underwater sound projector in a typical experimental tank," Journal of the Acoustical Society of America **65**(3), 826–829 (1979) 10.1121/1.382504.

[20] P. R. Molina, J. S. Rebull, C. O. Anglés, and N. Ortega, "Method for the Acoustic Characterization of Underwater Sources in Anechoic Tanks Based on Simulated Free-Field Scenario," Instrumentation viewpoint; SIXTH INTERNATIONAL WORKSHOP ON MARINE TECHNOLOGY, Martech 2015 70–73 (2015) http://hdl.handle.net/2117/77608.

[21] V. G. Jayakumari, R. K. Shamsudeen, R. Ramesh, and T. Mukundan, "Modeling and validation of polyurethane based passive underwater acoustic absorber," The Journal of the Acoustical Society of America **130**(2), 724–730 (2011) 10.1121/1.3605670.

[22] C. E. Dobbs, G. H. Fronk, T. B. Neilsen, and C. T. Vongsawad, "Underwater acoustic intensity characterization of anechoic panels in laboratory tank," The Journal of the Acoustical Society of America **150**(4), A196–A196 (2021) https://doi.org/10.1121/10.0008109 10.1121/10.0008109.

[23] N. Cochard, J. L. Lacoume, P. Arzeliès, and Y. Gabillet, "Underwater Acoustic Noise Measurement in Test Tanks," IEEE Journal of Oceanic Engineering **25**(4), 516–522 (2000).

Appendix C

The impact of room location on time reversal focusing amplitudes

Brian Patchett was a graduate student researching nonlinear focusing using time reversal. As part of that work, a numerical study was performed using a modal summation approach. This author assisted in the design and implementation of the simulation algorithms. This appendix is an article published as B. D. Patchett, B. E. Anderson, and A. D. Kingsley, "The impact of room location on time reversal focusing amplitudes," *J. Acoust. Soc. Am.* **150**(2), 1424 (2021); https://doi.org/10.1121/10.0005913. It is reprinted in this dissertation under the terms of ASA's Transfer of Copyright Agreement, item 3. I hereby confirm that the use of this article is compliant with all publishing agreements.

JASA ARTICLE

The impact of room location on time reversal focusing amplitudes

Brian D. Patchett, Brian E. Anderson,[a] and Adam D. Kingsley
Acoustics Research Group, Department of Physics and Astronomy, Brigham Young University, Provo, Utah 84602, USA

ABSTRACT:
Time reversal (TR) is a signal processing technique often used to generate focusing at selected positions within reverberant environments. This study investigates the effect of the location of the focusing, with respect to the room wall boundaries, on the amplitude of the focusing and the uniformity of this amplitude when focusing at various room locations. This is done experimentally with eight sources and two reverberation chambers. The chambers are of differing dimensions and were chosen to verify the findings in different volume environments. Multiple spatial positions for the TR focusing are explored within the rooms' diffuse field, against a single wall, along a two-wall edge, and in the corners (three walls). Measurements of TR focusing at various locations within the room show that for each region of study, the peak amplitude of the focusing is quite uniform, and there is a notable and consistent increase in amplitude for each additional wall that is adjacent to the focal location. A numerical model was created to simulate the TR process in the larger reverberation chamber. This model returned results similar to those of the experiments, with spatial uniformity of focusing within the room and increases when the focusing is near adjacent walls. https://doi.org/10.1121/10.0005913

(Received 27 April 2021; revised 24 June 2021; accepted 30 July 2021; published online 25 August 2021)

[Editor: Julien de Rosny] Pages: 1424–1433

I. INTRODUCTION

Time reversal (TR) is a signal processing technique that relies on the principle of reciprocity in a given environment to generate a focused signal at a location within that environment.[1,2] This technique benefits from being performed in a reverberant environment and is often performed in one. It began as a method called matched signal processing for underwater communication[3–5] and has since branched to multiple scientific fields such as medicine,[6,7] nondestructive evaluation of materials (NDE),[8–10] and source event localization in geophysics.[11] TR has also been explored with sound in the audible range as a method of communication in complex reverberant environments[12,13] as well as common room situations.[14] Recently, TR of high-amplitude ultrasound in air was used to generate a difference frequency.[15] The focusing process is comprised of two steps, an initial forward step in which the impulse response (IR) of the environment is calculated and a backward step where the IR is reversed in time and broadcast from the initial source position [the so called reciprocal TR (Ref. 2) process]. This time reversed impulse response (TRIR) signal is then broadcast, causing energy to converge on the receiver position, resulting in impulsive focusing.

To achieve the forward step of TR, multiple sources and a single receiver are placed in a reverberation chamber. A chirp signal is broadcast from each of the source locations individually, and the chirp response (CR) of each broadcast is recorded at the receiver position. Because the IR is spatially unique for each individual source/receiver system, this step is performed consecutively for each of the eight sources alone. If the IRs were not captured consecutively, then the signal recorded at the receiver would be a mix of all eight IRs together, and they could not be separated for the backward step performed later. This also produces individual IRs with better resolution and signal-to-noise ratio than if they were all collected simultaneously. The CR is described mathematically as the convolution of the chirp signal with the IR of the reverberation chamber. Once the CRs have been recorded, the IR for each can also be calculated. Once obtained, the IR is reversed on the time axis, creating the TRIR. Each of the TRIRs is then broadcast from all sources simultaneously. Due to the reciprocal nature of the system, the emissions from the TRIRs from each source trace the same paths back through the reverberation chamber to the receiver. The result is a convergence of the signals on the receiver, generating a focus. The location of this focusing will be termed the focal location. The converging acoustic waves behave in such a way that the eight simultaneous broadcasts overlap constructively and add collectively to the focusing amplitude. The amplitudes are such that linearity can be assumed in each individual chirp broadcast, but during the backward step the amplitude of the converging waves near the focal location is large enough that nonlinear phenomena occur. In the medical field, a similar TR technique is employed to both locate and destroy kidney stones in a technique known as lithotripsy.[7,16] Scientists studying NDE have employed this method of TR in solids to evaluate damage to a material through vibrational excitation of the material using a TR generated focus in this same way.[9,10]

The first studies applying TR to room acoustics focused primarily on communication in reverberant environments

[a]Electronic mail: bea@byu.edu, ORCID: 0000-0003-0089-1715.

https://doi.org/10.1121/10.0005913

with complex structures. Candy *et al.*[12,13] studied the application of TR communication in highly reverberant environments. They found that communication quality could be improved through the use of multiple sources and a linear equalization filter. In a subsequent study, Ribay *et al.*[17] applied a room acoustics model, based on work by Draeger and Fink[18] and Derode *et al.*[19] using TR in solid materials, to show that focal amplitudes are dependent upon the number of sources present, the reverberation time (RT_{60}) of the environment, and the bandwidth of the IR. Additionally, Yon *et al.*[14] performed an experimental study in a standard room (non-reverberation/non-anechoic), finding that TR produces temporal and spatial focusing that is better than time-delay beamforming. This is due to multiple sound paths between the sound sources and focus location. It was also found that increasing the number of sources while simultaneously increasing the bandwidth of the IR decreases the level of the side lobes, resulting in improved focusing. Those experiments were done with a linear 20-loudspeaker array and a single microphone mounted to a liner scanning system. This allowed the group to measure the focus both spatially and temporally. A numerical and experimental study recently conducted by Denison and Anderson[20,21] was able to show through similar modeling techniques that changes in RT_{60} due to changes in the volume of the room affect the amplitude of the focus differently than do changes to absorption. Increasing the volume of a reverberant environment (thereby increasing RT_{60}) with similar boundary conditions (wall absorption) leads to a decrease in peak focal amplitudes when all other variables remain constant. They were also able to show a direct connection between the RT_{60} of a room and the performance of the TR focusing, demonstrating that a longer RT_{60} reduced the spatial side lobes that are characteristic to TR focusing. Their experimental work was done in a reverberation chamber, where absorbers were used to tailor the RT_{60} to study the effect on the focus signal. Ribay *et al.*[17] limited their study to changes in RT_{60} due to changes in absorption (they did not explore the impact of room volume). Denison and Anderson verified the work of Ribay *et al.*, while also studying the impact of a changing volume. However, Denison and Andersons' experimental verifications of the increased volume effect were limited to non-ideal environments. These effects have not been studied or verified in reverberation chambers until now. Experimental work performed by Ma *et al.*[22] found that when using metamaterial objects known as acoustic prisons, they were able to increase the peak focus intensity when additional reverberating surfaces were included inside of the prison objects. Additional work by Ma *et al.*[23] used a set of loudspeakers with a microphone and reported findings similar to those discussed above, primarily that chirp bandwidth, chirp time duration, and RT_{60} all affect the focus in a meaningful way.

Previous studies have not explored the impact of the TR focal location's position within a room (i.e., near walls or away from walls and what level of consistency is found when away from walls) on the TR focusing amplitude. The purpose of this paper is to apply the TR process experimentally in two different reverberation chambers, along with numerical modeling of TR in a reverberation chamber, to show how the TR focusing amplitude depends on the focal location within a room. Reliable prediction of an expected focus amplitude at a given position within the environment relative to reflecting surfaces is necessary when applications involve using TR to deliver energy to that position. Resulting data show that the amplitude increases by moving the focal location from a diffuse field position (away from all walls/surfaces) to a position adjacent to one reflecting wall by approximately 3 dB. In this paper, the word "wall" will be used to refer to any of the four walls, the ceiling, or the floor. It increases again near a two-wall edge and again in the corner of the room where three walls are adjacent to the focal location. The increase in amplitude for diffuse sound in a room is well known to be a 6 dB increase with each additional reflecting surface. A mathematical description of the TR process is performed in Sec. V, confirming that the resulting increases should also be on the order of 6 dB, and a reason why they are not that high in both the experiment and the model is given. The amplitude of the focusing is also quite uniform when the focal location is placed anywhere within the diffuse field of the room. This is in contrast to the expected outcome for diffuse sound fields in rooms, where one standard deviation away from the mean of the level can be expected to vary by as much as +5/–6 dB.[24] The volume of the room has a significant effect on the amplitude as well, confirming the results obtained by Denison *et al.*[20] The measurements taken in the small reverberation chamber (SRC) were consistently higher than those taken in the large reverberation chamber (LRC) when using the same configuration and output settings.

It is worth noting that the peak sound pressure levels (SPLs) attained in the experiments presented here were on the order of 150–160 dB. These are only peak levels of a short duration focal event, but these levels are considerably high. Applications for these levels include the investigation of high amplitude sound acting on rigid bodies, testing of hearing protection at high amplitudes, and use as a tool to study nonlinear sound propagation. The work of Willardson *et al.*[25] showed that nonlinear effects can begin to cause distortion in the TR focusing when the peak levels exceed about 160 dB. Thus, we assume that the peak levels reported here are within the linear regime.

II. EXPERIMENTAL DETAILS

A. Setup

The experiments were conducted in two separate reverberation chambers. The two chambers were chosen because they differ in volume but have similar construction. The walls, floors, and ceilings are composed of the same materials and treatment from one chamber to the next. And there are diffuser panels of similar material suspended in each. Dimensions of the SRC are 5.70 m × 4.30 m × 2.50 m, with a volume of 61.3 m^3. The SRC has an overall RT_{60} of 4.2 s,

with a Schroeder frequency of 522 Hz. The LRC measures 4.96 m × 5.89 m × 6.98 m, with a volume of 204 m^3, an overall RT_{60} of 7.6 s averaged across the frequency spectrum of the input signal,[26] and a Schroeder frequency of 410 Hz.[27] A GRAS (Holte, Denmark) 40BE free-field microphone with a 26CB preamplifier is used as the receiver (referred to as a microphone in this section) with a GRAS 12AX power module. BMS (Hannover, Germany) 4590 dual diaphragm high output loudspeakers fitted with original equipment manufacturer (OEM) crossovers and horns are utilized as the sources (referred to as loudspeakers in this section). It was found by Anderson *et al*. that directionality of sources has a destructive effect on the focus amplitude when the sources are pointed at the focal location and that facing the sources away from the focal location serves to increase the focus amplitude.[28] As such, these loudspeakers are placed near the walls in the room and oriented in such a way as to be facing away from the focal location (microphone position) (see Fig. 1). Two four-channel Crown (Stamford, CT) CT4150 amplifiers are used to provide power to the loudspeakers. All signals are generated and processed for TR using a custom in-house LabVIEW™ interface, coupled with two Spectrum (Grosshansdorf, Germany) M2i.6022 signal generation cards and an M2i.4931 digitizer card. All post-processing is handled in MATLAB™.

To begin, a logarithmic chirp signal with a bandwidth of 500–15 000 Hz is broadcast from a single loudspeaker, and the CR is recorded at the microphone position. In initial trials, the use of a logarithmically swept chirp signal produced a higher amplitude focus than a linear chirp signal. It was found by Willardson *et al*. that extending the bandwidth beyond 500–7500 Hz had a negligible effect on the peak amplitude of the focus in the LRC environment.[25] However, the Willardson study was limited in that the equipment only had the capability of reaching 9500 Hz. The drivers used in the current study have been upgraded with OEM crossovers, allowing for frequencies up to 15 000 Hz. Since the objective of this study, in part, is to produce a focus with a high signal-to-noise ratio, the decision to extend the bandwidth to the full flat frequency response capability of the driver (500–15 000 Hz) was made in order to capture the most possible energy from the focusing sound field.

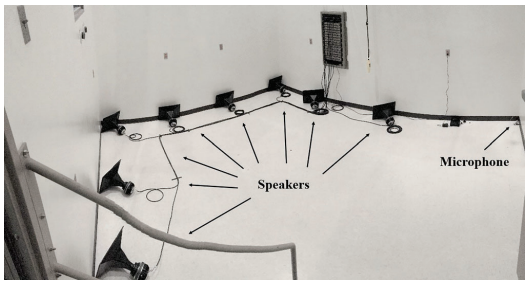

FIG. 1. (Color online) Photograph of the experimental layout in the LRC. The room is a rectangular room with parallel walls, along with reflecting panels (not shown in the image) intended to make the sound field more diffuse. Distortion in the image is due to the panoramic nature of the photograph.

An IR for this loudspeaker and microphone combination is then calculated using a cross correlation of the chirp with the CR[28,29] and stored for that loudspeaker channel. This is repeated for each loudspeaker-microphone combination to acquire eight individual IRs. The IRs are then reversed in time to create a set of eight TRIRs, at which point TRIRs are broadcast simultaneously from each of their respective loudspeakers (see Fig. 2). Each IR has a sampling frequency of 250 kHz for the entire process. The high sampling frequency ensures that the peak amplitude of the focusing is captured with high accuracy.

The TR process time aligns the convergence of multiple arrivals of sound to achieve constructive interference in the form of high amplitude focusing of sound at the microphone location. The use of software synchronization of the broadcasts from multiple loudspeakers generates a higher amplitude focus than a single loudspeaker would when used alone. This full TR process is repeated at various spatial positions within the room in this study to explore the dependence of the TR focusing amplitude with respect to the spatial location of that focusing within the room. All measurements are made assuming linearity both acoustically and in terms of the operating limits of the equipment used. Even though the focus amplitude peaks have levels of around 150 dB, linear scaling of the focusing is observed using different amplification levels.[24]

B. Spatial position measurements

One aim of creating a diffuse field in room acoustics is to provide uniform SPLs measured at any location within that diffuse field. However, in Fig. 2.17(a) of Kleiner and Tichy[24] and in Fig. 3.8 of Kuttruff,[30] it is demonstrated that the pressure values measured across a diffuse field in a reverberant room can vary by greater than ±10 dB for a given frequency as a measurement receiver is moved across the space. Kleiner and Tichy quantified the variation by stating, "The logarithmic representation of twice the variance that contains 70% of the sound amplitudes is (nonsymmetrically) within 11 dB…".[24] In other words, 70% of the pressure fluctuations can be within +5 or –6 dB above and below the mean value (one standard deviation above and below the mean).

This variation is due to modal overlapping throughout the space, even though the frequency range may be above the Schroeder frequency.[31] It is therefore interesting to investigate how the amplitude of TR focusing varies across the diffuse field region of a room and how the proximity of the focal location to walls impacts the amplitude of the focusing. It may be of interest to know how much uncertainty in the focusing amplitude one might expect when using TR to focus sound to a given location within a room. Throughout these measurements, it is useful to keep in mind that the focal location is changed by moving the microphone to different locations in the room, while keeping the

https://doi.org/10.1121/10.0005913

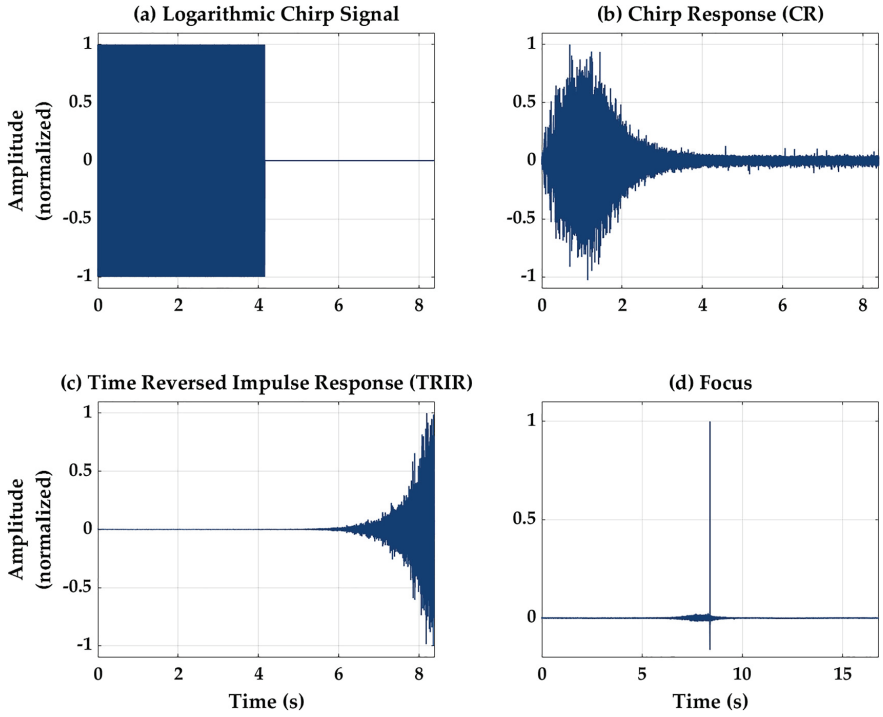

FIG. 2. (Color online) example signals used in the TR experiments. (a) The logarithmic chirp signal, 4.16 s in length. (b) The CR recorded in the forward process at the microphone. (c) The normalized TRIR. (d) Focus generated by simultaneous broadcast of eight loudspeakers. All amplitudes in this figure are normalized for clarity in display.

loudspeakers' locations fixed, and redoing a full TR experiment at the new microphone location (both forward and backward steps).

The various focal locations explored here include four different types of locations, with focal locations of similar types being referred to as regions: the open space (diffuse field region) of the room, against one of the reflecting walls (wall region), against two of the reflecting walls (edge region), and against three walls of the room (corner region). The diffuse field position measurements are made in accordance with the ISO standard,[32] where a diffuse field is defined as occurring at least 1 m from any reflecting wall. A total of 20 diffuse field focal locations are chosen at random, while ensuring that the focal location is at least 1 m from any of the reflecting walls in the room (see Fig. 3). The single wall measurements are made at six random positions against one of the reflecting walls in the room. Care is taken to ensure that the focal location remains more than 1 m from any other adjacent wall. The edge region measurements are made at six locations in the room. Again, care is taken to keep the focal location at least 1 m away from the corners of the room. For practical purposes, only four corner measurements are made due to the geometry of the rooms and the difficulty in reaching the upper corners reliably with the microphone. In the one- and two-wall region measurements,

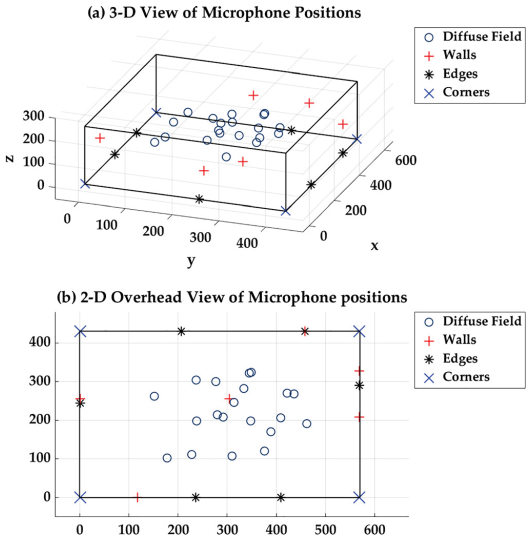

FIG. 3. (Color online) Microphone positions in the SRC. Each position region is denoted with a unique character. (a) Three-dimensional (3-D) representation of positions. (b) Top-down view of the chamber in two dimensions (2-D).

the microphone is placed 1 cm from any wall for consistency in positioning. The body of the microphone is oriented so that it is parallel to the walls. In the case of the corner measurements, the microphone is pointed directly into the corner, 1 cm from its apex, with an equal angular alignment from each wall. Measurements are performed in both the SRC and LRC to compare results for both environments.

Figure 4 illustrates the focal amplitude measurements with a bar graph in decibels (peak SPLs). This figure shows clearly that the position of the focal location in proximity to additional walls has a consistent effect of increasing the focusing amplitude. It is also worth noting that the focusing amplitude in each particular region has very little variance from the mean SPL. This indicates that there is a fair amount of uniformity of the focusing amplitude at various focal locations within the same region, especially when compared to the greater than ±10 dB fluctuations that can be expected when moving a microphone to various locations within a diffuse field without using TR. This means that one can reliably expect a certain focal amplitude irrespective of where they choose to focus sound with TR within a given region of the room.

The mean values in Fig. 4 were calculated using the squared pressure values, as this accurately represents the energy relation to the peak focal amplitude values in the sound field. Standard deviations were measured as 150.5 dB (+0.5/–0.5 dB) in the diffuse field, 153.6 dB (+0.8/–1.0 dB) against one wall, 155.7 dB (+0.9/–1.0 dB) against an edge (two walls), and 158.7 dB (+0.7/–0.8 dB) for the corners (three walls), where the values in the parentheses represent one deviation above and below the mean pressure value. As is evident in the mean values reported, the average focusing amplitude for a focal location near a wall increases by 3.1 dB (+0.6/–0.7 dB) from the diffuse field focal locations. The average increases again by 2.1 dB (+0.7/–0.8 dB) when the focal location is placed near an edge (two walls) compared to one-wall focal locations. Corner locations (three walls) again increase the focusing amplitudes by 3.0 dB (+0.6/–0.7 dB) relative to an edge (two walls).

The variation of the focal locations for TR experiments conducted in the SRC is now similarly conducted in the LRC. All signal settings, gain values, and signal processing are identical to those used in the SRC experiments to ensure a direct comparison between the two rooms of different volumes. The set of measurements made in the LRC also serves to confirm that the results from the SRC may be expected in other similar rooms and allows for comparison of the focusing amplitudes in two similar rooms of different volumes. Figure 5 shows the microphone positions used to measure peak focal amplitudes in the LRC, while Fig. 6 shows a similar bar graph as Fig. 4, but now for values measured in the LRC.

A similar uniformity is observed in the LRC measurements as was observed in the SRC measurements for each region of locations. The mean value (and one standard deviation above/below the mean) was measured to be 147.7 dB (+1.0/–1.4 dB) in the diffuse field, 151.5 dB (+0.4/–0.5 dB) against one wall, 153.7 dB (+0.7/–0.8 dB) against an edge (two walls), and 156.1 dB (+0.5/–0.6 dB) for the corners (three walls). Here, the mean diffuse field peak focal amplitude increases by 3.8 dB (+1.0/–1.2 dB). Moving to an edge, the mean increases by 2.2 dB (+1.0/–1.2 dB). Moving from an edge to a corner, the mean increases by 2.4 dB (+0.9/–1.1 dB). According to the experimental data, the SRC consistently yields higher focusing amplitudes regardless of the type of location within the room. For example, the focusing amplitude at SRC diffuse field focal locations is consistently higher than the focusing amplitude at LRC diffuse field focal locations. This agrees with the finding of Denison *et al.*[20] that, when all other experimental characteristics are kept the same, the smaller volume room will have a higher TR focusing amplitude. Figure 7 shows a comparison of the

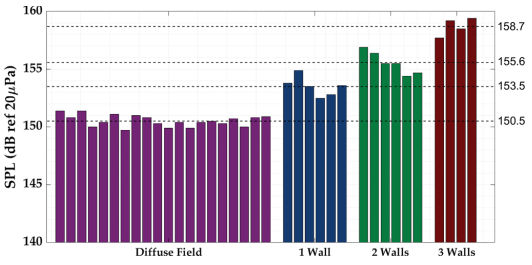

FIG. 4. (Color online) Bar graph display of measured peak SPL for various TR experiments done at the locations specified in Fig. 3 for the SRC. The mean of the peak SPL values for each region is displayed as a dashed line with mean value label to the right.

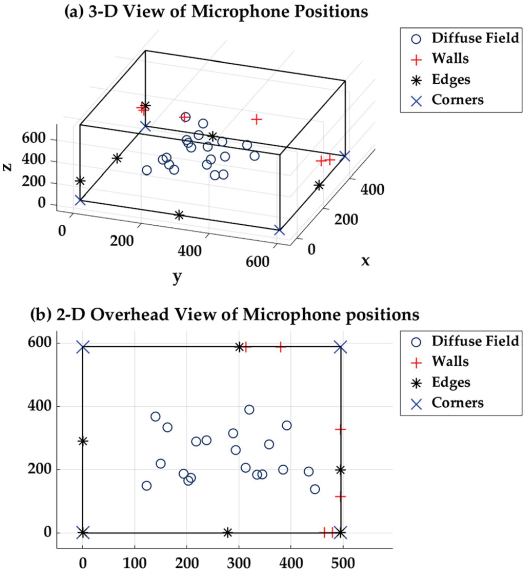

FIG. 5. (Color online) Microphone positions in the LRC. Each position region is denoted with a unique character. (a) 3-D representation of positions. (b) Top-down view of the chamber in 2-D.

https://doi.org/10.1121/10.0005913

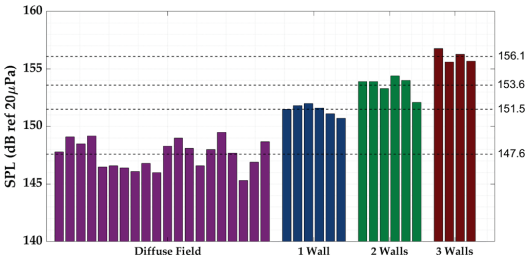

FIG. 6. (Color online) Bar graph display of measured peak SPL for various TR experiments done at the locations specified in Fig. 5 for the LRC. The mean of the peak SPL values for each region is displayed as a dashed line with mean value label to the right.

averaged focal signals measured at the focal locations in the SRC and LRC (averaged across the focal locations within a given region for a given room). This illustrates that the increase in peak focal amplitudes is consistent for the measurements performed in the SRC versus the LRC.

III. NUMERICAL MODEL OF EXPERIMENT

A numerical model was generated to compare the experimental results obtained in the LRC to theory. The model is based on a modal summation equation given by Kleiner and Tichy.[24] This form of modal summation as a way to model TR differs from both Denison and Anderson[20,21] and Ribay *et al.*,[17] who each used models based on geometric ray tracing and image sources. Denison and Anderson[20] used an image source model of TR in a room, and though they did not report this in their paper, they did not observe an increase in TR focusing amplitude when focusing near walls in their model. As such, a new method that incorporated the summation of pressure contributions from each excited mode in the reverberation chamber was deemed appropriate in an attempt to match observed experimental results. The model here assumes a rectangular room with parallel walls. The presence of diffusors is not factored into the calculation, though they are present in the experimental reverberation chambers.

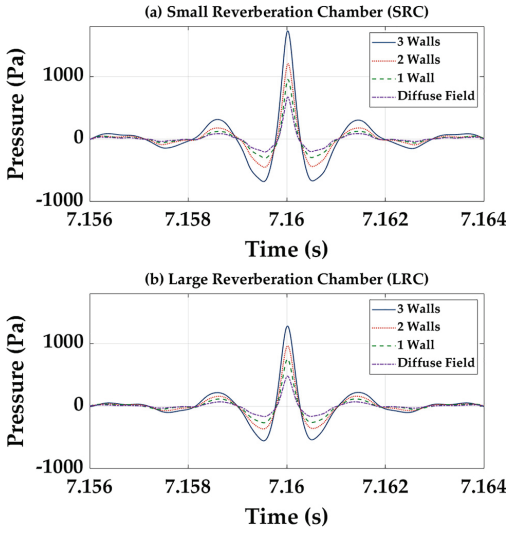

FIG. 7. (Color online) Average focal signals shown zoomed in on the time axis. (a) Comparison of the mean focal signals for each region in the SRC; (b) the same for the LRC.

The equation describes the pressure, $\hat{p}$, at receiver position (x, y, z) due to any given source position, (x_0, y_0, z_0), as a function of frequency or wavenumber, k, in a 3-D environment. It is a frequency response between the source and receiver locations,

$$\hat{p}(x,y,z,k) = -4\pi \frac{A}{V} \sum_{n=0}^{\infty} \frac{\Psi_n(x_0,y_0,z_0)\Psi_n(x,y,z)}{\left(k^2 - k_n^2 - j2k_n\frac{\delta_n}{c}\right)\Lambda_n}, \quad (1)$$

where A is the monopole amplitude related to the source strength (or volume velocity), Q, used in the original equation through the relationship,

$$A = \frac{j\rho_0 ckQ}{4\pi}, \quad (2)$$

V is the room volume $(204\,\mathrm{m}^3)$, n is the mode number, Ψ_n is the spatial dependence of the n th mode, k_n is the wavenumber for the n th mode, and δ_n is the damping factor. Λ_n is the function that accounts for orthogonality such that

$$\Lambda_n = \frac{1}{\varepsilon_{n_x}\varepsilon_{n_y}\varepsilon_{n_z}} \quad \text{and} \quad \varepsilon_{n_x,n_y,n_z} = \begin{Bmatrix} 1, \text{ for } n_x, n_y, n_z = 0 \\ 2, \text{ for } n_x, n_y, n_z = 1 \end{Bmatrix}, \quad (3)$$

where $\varepsilon_{n_x,n_y,n_z}$ represents the Neumann orthogonality factor for the three Cartesian spatial dimensions. Λ_n can have values of $1/2$ (for axial modes), $1/4$ (for tangential modes), and $1/8$ (for oblique modes). Since the primary purpose of this analysis was the comparison of focal amplitudes obtained at different regions of the room, the amplitude, A, of the source was set to a value of 1 in Eq. (1), resulting in a Green's function. The source output levels can be arbitrary in magnitude since linearity is assumed and only relative increases in focal amplitudes are of interest as they pertain to the focal location region in which they are calculated (diffuse field, wall region, etc.).

The model implies that for a given k, the modal response due to the source position, $\Psi_n(x_0, y_0, z_0)$, and due to the receiver position, $\Psi_n(x, y, z)$, is determined from a summation of an infinite number of normal modes of the room. For the rigid walled room being modeled, with dimensions $L_x = 4.96\,\mathrm{m}$, $L_y = 5.89\,\mathrm{m}$, $L_z = 6.98\,\mathrm{m}$, the eigenfunction can be written as $\Psi_n(x,y,z) = \cos(n_x\pi x/L_x)\cos(n_y\pi y/L_y)\cos(n_z\pi z/L_z)$. As an infinite number of modes would lead to an infinite computation time, only modes whose modal frequencies lie within the bandwidth of 500–15 000 Hz were used, as this is the same bandwidth of

the chirp used in the experimental data. The modal frequency bandwidth, $\Delta f = 2.2/\mathrm{RT}_{60}$ [see Eq. (3.43) of Ref. 30], was calculated for the lowest frequency of the chirp (with the longest RT_{60}) and determined to be 0.44 Hz. Thus, a spacing less than that of $\Delta f = 0.44$ Hz was selected to make sure that every mode would be sampled at this frequency resolution. This means that the calculation for the pressure at each position used a wavenumber value of $k = 2\pi f/c$, where k ranged from $f = 500.25$ Hz to $f = 15\,000$ Hz in steps of 0.25 Hz. This resulted in 60 000 values of k for each spatial position. Given the maximum frequency used, the number of modes summed for each value of k is approximately 7.1×10^7. While it is possible to limit the number of modes in the summation by including only those with a significant contribution to the pressure amplitude (such as only summing the modes within a certain number of modal bandwidths of a given k), this calculation included all available modes. The damping factor,

$$\delta_n = \frac{6.91}{(\mathrm{RT}_{60})_{f_n}}, \tag{4}$$

is calculated from frequency-dependent, experimentally obtained RT_{60} values.[30] The frequency-dependent $(\mathrm{RT}_{60})_{f_n}$ is calculated using reverse Schroeder integration (RSI) on the IRs measured in the LRC.[33] This ensures that the model has a RT_{60} (and a subsequent δ_n) that matches the experimental values as closely as possible. Before applying the RSI, each IR was filtered using a one-third octave band filter to find the RT_{60} as a function of frequency. The one-third octave values were then linearly interpolated to represent an approximation of the RT_{60} over all discrete frequencies at a resolution of 0.25 Hz, which is the frequency spacing of the model variable f_n. The δ_n values are computed from the extracted values of $(\mathrm{RT}_{60})_{f_n}$. This 0.25 Hz resolution was empirically determined to be sufficient. During post-processing, $(\mathrm{RT}_{60})_{f_n}$ values were extracted from numerically generated IRs using the RSI method again. This analysis returned $(\mathrm{RT}_{60})_{f_n}$ values matching the input $(\mathrm{RT}_{60})_{f_n}$ values, indicating that Eq. (4) generates a numerical IR that closely matches the experimentally measured IR.

Due to the quantity of the calculations required for this modeling approach and the size of the data stored in random access memory (RAM) as the pressure is calculated, Eq. (1) is computationally broken down into several pieces and then reassembled for a final calculation (parallelization of the code). This method reduces computation time to one-third of the original time as compared to a non-parallelized version of the code. The k_n^2 and k_n values in the denominator are calculated in a standard "for" loop nested for each physical dimension. Then the product of the eigenfunctions in the numerator is calculated in a parallelized "for" loop (parfor function in MATLAB™) for each index value of x, y, and z. Finally, all of the pieces are brought together into the final form of Eq. (1). The solution for each n value and the summation is computed using the graphical processing unit. The array of pressures at each mode is then summed for each k value and saved as a pressure versus frequency spectrum. This is repeated for each receiver position, $\Psi_n(x, y, z)$, of interest.

A post-processing modification to the output pressures of the model is used to simulate the experimental use of a logarithmic chirp weighting to the input signal. The weighting was determined by applying a low pass filter with a logarithmic frequency roll-off for the 500–15 000 Hz frequency bandwidth and then determining the appropriate filter values through a curve fit. To simulate a TR focusing of energy, an inverse fast Fourier transform is calculated with the pressure versus frequency vector output from Eq. (1), producing an IR from the numerical model. An autocorrelation of the numerical IR is used to produce a focal signal like that found using standard experimental TR for the given pressure spectrum at that position.[34] The application of autocorrelation on the numerical IR ensures that a central data point is always at the exact time for peak of the focus signal, producing a highly accurate value of peak focal amplitude. Because the maximum frequency is 15 kHz, a sampling frequency of 30 kHz is assumed for all focus generation with the numerical data. Example spectra and signals at each step in this simulation of TR can be seen in Fig. 8.

It is worth pointing out that Eq. (1) is the same equation used by Kleiner and Tichy[24] to determine the fluctuations in pressure found within a diffuse field. Due to the computational nature of this work, many more focal locations were included in this numerical analysis than were used experimentally. A total of 18 randomized focal locations in each region were selected except for the corners, where seven focal locations were selected. A single source was used in the model for simplicity and economical use of computation time. Its location was chosen to be the lower corner of the numerical "room," opposite the majority of the measurement locations. Figure 9 depicts the source and receiver positions used as focal locations in the numerical

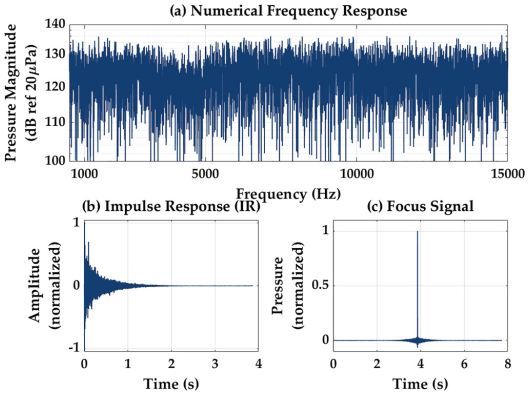

FIG. 8. (Color online) (a) An example frequency response output from the numerical model based on Eq. (1); (b) the IR found by taking an inverse fast Fourier transform of (a); (c) the focal signal generated by an autocorrelation of the IR in (b).

https://doi.org/10.1121/10.0005913

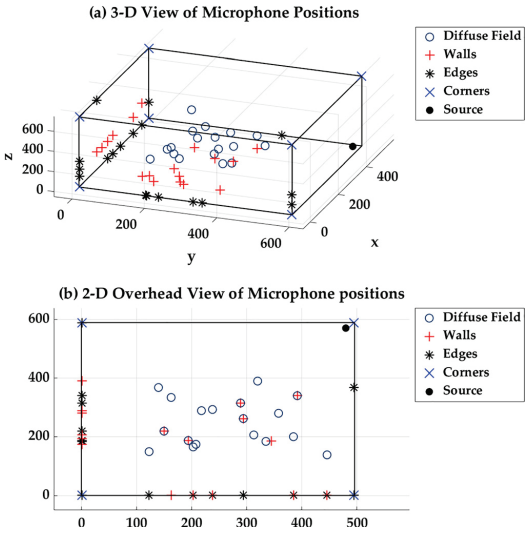

FIG. 9. (Color online) Receiver positions used in the numerical modeling. Each position region is denoted with a unique character. (a) 3-D representation of positions. (b) Top-down view of the chamber in 2-D.

calculations, and Fig. 10 shows the peak focal amplitudes obtained from the numerical model with a mean value for each region. The significance of the focal amplitude values lies in the uniformity of the focal amplitudes in each region and the difference in amplitudes from one region of focal locations to the next, as was investigated experimentally. The mean value (and one standard deviation above/below the mean) was measured to be 152.7 dB (+0.4/–0.5 dB) in the diffuse field, 155.7 dB (+0.4/–0.4 dB) against one wall, 159.1 dB (+0.2/–0.2 dB) against an edge (two walls), and 163.1 dB (+0.5/–0.6 dB) for the corners (three walls). The mean values increase by 3.0 dB (+0.3/–0.3 dB) when moving from the diffuse field to one wall, 3.4 dB (+0.2/–0.2 dB) when moving from one wall to an edge, and 4.0 dB (+0.4/–0.4 dB) when moving from the edge into a corner. The general trend of an increase in focal amplitude with the proximity to additional walls matches that seen experimentally.

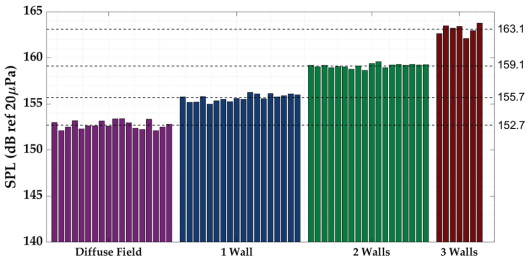

FIG. 10. (Color online) Bar graph display of measured peak SPL for various TR experiments done at the locations specified in Fig. 9 for the numerically modeled reverberation chamber. The mean of the peak SPL values for each region is displayed as a dashed line with mean value label to the right.

Numerical modeling was also conducted without using the previously mentioned filter that simulates the use of logarithmic chirp to see if this filter impacts the modeling results. The use of this filter to simulate the logarithmic chirp showed no significant change in the peak focal amplitudes generated by the model.

IV. COMPARISON OF NUMERICAL TO EXPERIMENTAL RESULTS

Table I provides a comparison summary of the two sets of experimental results in the SRC and in the LRC along with numerical results in the LRC. The comparison clearly shows that increasing the number of reflecting surfaces (walls) near the focal location consistently raises the value of the focus amplitude near an average of ≈3 dB per additional surface (to within the given standard deviation of each region). It is especially worth noting the overall uniformity of each region. Both of the experimental cases as well as the numerical case showed uniformity to within a very small deviation from the mean. This deviation was smallest in the numerical model, which is to be expected given the idealization of the algorithm's "environment" (virtual space generated for calculation) when compared to the potential for systematic and random error in real world experimentation.

Variation in the increases (meaning comparing the 3.8 dB increase in the experimental LRC results to the 3.1 dB increase in the experimental SRC results to the 3.0 dB increase observed in the numerical LRC results when moving from the diffuse field region to the one-wall region) in average focal amplitude value from one focal location region to the next could be caused by multiple things. The loudspeakers used in the experiments are placed near walls, with the horn openings facing the wall, close enough that there could be a frequency-dependent change in the radiation from the source that is not seen in the numerical model (the model assumes sources with flat frequency responses). It is also worth noting that omnidirectional sources are assumed in the numerical model, whereas the experimental ones are directional. Because the experimental loudspeakers are directional, they were pointed away from the receiver to avoid the large direct path arrival relative to the other arrivals in the IR as suggested by Anderson *et al.*[26] The rooms used for experiments also had diffusor panels hung in them, whereas the numerical model assumed an empty rectangular room. Also, the number of sources used in the modeling was decreased to one to simplify the calculation. These exceptions aside, the increasing nature of the focal amplitude in each focal location region is consistent, and similar trends are seen in the experimental results and the numerical simulations.

V. THEORETICAL IMPACT OF WALL PROXIMITY ON FOCAL AMPLITUDE

Recall from Sec. III that traditional TR can be modeled as an autocorrelation of the IR. This is the equivalent to multiplying Eq. (1) by its complex conjugate to compute the auto-spectrum. The equation can be simplified by

TABLE I. Comparison of the average results for the increase in focal amplitude when the focal location is moved from one focal location region to the next (adding a wall each time) in each of the reverberation chambers as well as the numerical results. Values shown represent peak SPLs in decibels (ref 20 μPa). The average values for one-wall locations are given relative to the average diffuse field location values. The values for edge locations are given relative to the average one-wall values. The values for corner locations are given relative to the average edge location values. Values in parentheses represent one standard deviation above and below the mean pressure value given.

Focal location	Experimental LRC	Experimental SRC	Numerical LRC
Diffuse field	0.0 dB (+1.0/−1.4 dB)	0.0 dB (+0.5/−0.5 dB)	0.0 dB (+0.4/−0.5 dB)
Wall	+3.8 dB (+1.0/−1.2 dB)	+3.1 dB (+0.6/−0.7 dB)	+3.0 dB (+0.3/−0.3 dB)
Edge	+2.2 dB (+1.0/−1.2 dB)	+2.1 dB (+0.7/−0.8 dB)	+3.4 dB (+0.2/−0.2 dB)
Corner	+2.4 dB (+0.9/−1.1 dB)	+3.0 dB (+0.6/−0.7 dB)	+4.0 dB (+0.4/−0.4 dB)

condensing all of the terms not associated with the eigenfunctions into a single variable A_n,

$$A_n = \frac{\left(k^2 - k_n^2 - j2k_n\frac{\delta_n}{c}\right)\Lambda_n}{-jk\rho_0 cQ/V}. \tag{5}$$

An auto-spectrum can then be represented by the product of the original summation with its complex conjugate,

$$y(r_0, r, k) = \sum_{n=0}^{\infty}\frac{G_n(r_0, r)}{A_n}\cdot\sum_{n=0}^{\infty}\frac{G_n(r_0, r)}{A_n^*}, \tag{6}$$

where $G_n(r_0, r)$ represents the product of the eigenfunctions $\Psi_n(x_0, y_0, z_0)\Psi_n(x, y, z)$ and in the case of a rigid walled room is a real quantity. This product of summations can then be expanded as

$$\begin{aligned} y(r_0,r,k) = &\left(\cdots + \frac{G_{n-1}(r_0,r)}{A_{n-1}} + \frac{G_n(r_0,r)}{A_n}\right.\\ &\left. + \frac{G_{n+1}(r_0,r)}{A_{n+1}} + \cdots\right)\cdot\left(\cdots + \frac{G_{n-1}(r_0,r)}{A_{n-1}^*}\right.\\ &\left. + \frac{G_n(r_0,r)}{A_n^*} + \frac{G_{n+1}(r_0,r)}{A_{n+1}^*} + \cdots\right). \end{aligned} \tag{7}$$

A careful analysis of the product of the summations allows them to be rewritten as the sum of same-indexed terms and a sum of cross-terms (where the indices are different),

$$\begin{aligned} y(r_0, r, k) = &\sum_{n=0}^{\infty}\frac{G_n(r_0, r)^2}{|A_n|^2}\\ &+ \sum_{l\neq m=0}^{\infty}\sum_{m\neq l=0}^{\infty}\frac{G_l(r_0, r)G_m(r_0, r)}{A_l A_m^*}. \end{aligned} \tag{8}$$

The pressure contribution from a single mode can be evaluated as a fixed source while the receiver is moved throughout the space. Thus, the impact on the response from each mode when having the receiver against one or more walls may be determined. For any given mode, the first summation term in Eq. (8) yields an average increase in 6 dB when the receiver position is moved from the diffuse field region to up against one wall. Another 6 dB is gained when the receiver position is placed at an edge. And again, there is another 6 dB increase when the receiver position is in the corner. The second summation term yields no average increase whether the receiver is in the diffuse field or up against any walls. Thus, when summing many modes in Eq. (8), the overall result is that a 6 dB increase should be expected when the receiver is placed exactly against each additional wall.

This analysis suggests a higher increase at the surface regions than is found both experimentally and numerically. This is likely due to the positions of the microphones being 0.01 m from the walls in both the experiments and the numerical simulation. Experimentally, this was done to avoid direct contact with the surfaces, so that mechanical vibration between the walls and the microphone would be avoided. Also, placing the microphones exactly in the corner or at an edge of a room is not possible due to the practical, finite size of microphones. The microphone positions used in the numerical calculation were mostly the same as in experiments in order to replicate the experiment as closely as possible with the numerical simulation. However, when the microphone positions are moved exactly against the walls in the simulation, the increase is 6 dB for each wall added, just as the mathematics in this section suggests.

VI. CONCLUSIONS

The results presented in this paper have shown that, using the TR process, a relative uniformity of the peak focal amplitude may be expected within a diffuse field (or when against one wall, against two walls, or against three walls). The standard deviation of the obtained focal amplitudes across each type of focal amplitude region is small. This indicates that no matter where a receiver is placed within a specific region (diffuse field, single wall, etc.), the amplitude may not fluctuate more than 1 dB. As described in Sec. II B, diffuse field theory predicts a deviation in SPL for any given frequency of up to 11 dB (+5/–6 dB above and below the mean) across a reverberant space.[23] The TR technique provides a peak focal amplitude that varies far less across a reverberant space, having a deviation of up to 1 dB (+0.5/–0.5 above and below the mean) experimentally and 0.9 dB (+0.4/–0.5 above and below the mean) in the modeling results.

The proximity of the focal location with respect to adjacent walls has a significant effect on the amplitude of a generated focus. The increase in amplitude expected when the focal location is placed exactly against each additional wall

is 6 dB. However, according to the presented experimental results, an increase in amplitude on the order of ≈3 dB per wall can be seen as the focal location is made to be adjacent to each additional wall, likely due to the practical inability to place a microphone exactly against a wall, edge, or corner of a room. This indicates that placement near three walls (in a corner of a room) produces the highest possible TR focal amplitude, approximately 9 dB higher than focal amplitudes obtained in the diffuse field. These experimental results are verified with a numerical model. This knowledge is important for the use of TR in reverberant environments.

These conclusions are based on experiments conducted in a SRC (volume 61 m^3) and in a LRC (volume 204 m^3). The full TR process (both forward and backward steps) was conducted for several different focal locations within these rooms while keeping the loudspeaker locations fixed. The focal locations included many positions away from walls in the diffuse field, near one wall, near two walls (edges of the room), and near three walls (corners of the room). A numerical model of the LRC was constructed to simulate TR in a rectangular room. The model was based on normal mode summation theory.

The size of a room also has an effect on the amplitude of the TR focusing. The facilities used in this study differed in volume by approximately a 3:1 ratio. The smaller of the two chambers produces focal amplitudes that average 2.4 dB higher for each type of focal location region. This agrees with the finding by Denison and Anderson[20] that a smaller volume room can contribute to the generation of a higher focal amplitude than a larger volume room.

ACKNOWLEDGMENTS

Funding provided by internal support from the Brigham Young University College of Physical and Mathematical Sciences is gratefully acknowledged. We thank Kevin Leete and Mylan Cook for their insight into mean and standard deviation calculations of pressure magnitudes.

[1]M. Fink, "Time reversed acoustics," Phys. Today **50**(3), 34–40 (1997).
[2]B. E. Anderson, M. Griffa, C. Larmat, T. J. Ulrich, and P. A. Johnson, "Time reversal," Acoust. Today **4**(1), 5–16 (2008).
[3]C. S. Clay and B. Anderson, "Matched signals: The beginnings of time reversal," Proc. Meet. Acoust. **12**(1), 055001 (2011).
[4]A. Parvulescu and C. S. Clay, "Reproducibility of signal transmissions in the ocean," Radio Electron. Eng. **29**(4), 223–228 (1965).
[5]H.-C. Song, "An overview of underwater time-reversal communication," IEEE J. Ocean. Eng. **41**(3), 644–655 (2016).
[6]A. Sutin and H. Salloum, "Prospective medical applications of nonlinear time reversal acoustics," Proc. Meet. Acoust. **34**(1), 020003 (2018).
[7]G. Montaldo, P. Roux, A. Derode, C. Negreira, and M. Fink, "Ultrasound shock wave generator with one-bit time reversal in a dispersive medium, application to lithotripsy," Appl. Phys. Lett. **80**, 897–899 (2002).
[8]B. E. Anderson, M. Griffa, T. J. Ulrich, P.-Y. L. Bas, R. A. Guyer, and P. A. Johnson, "Crack localization and characterization in solid media using time reversal techniques," in *Proceedings of the 44th U.S. Rock Mechanics Symposium and 5th U.S.-Canada Rock Mechanics Symposium*, Salt Lake City, UT (June 27–30, 2010), ARMA-10-154.
[9]S. M. Young, B. E. Anderson, S. M. Hogg, P.-Y. L. Bas, and M. C. Remillieux, "Nonlinearity from stress corrosion cracking as a function of chloride exposure time using the time reversed elastic nonlinearity diagnostic," J. Acoust. Soc. Am. **145**(1), 382–391 (2019).
[10]B. E. Anderson, L. Pieczonka, M. C. Remillieux, T. J. Ulrich, and P.-Y. L. Bas, "Stress corrosion crack depth investigation using the time reversed elastic nonlinearity diagnostic," J. Acoust. Soc. Am. **141**(1), EL76–EL81 (2017).
[11]C. S. Larmat, R. A. Guyer, and P. A. Johnson, "Time-reversal methods in geophysics," Phys. Today **63**(8), 31–35 (2010).
[12]J. V. Candy, D. H. Chambers, C. L. Robbins, B. L. Guidry, A. J. Poggio, F. Dowla, and C. A. Hertzog, "Wideband multichannel time-reversal processing for acoustic communications in highly reverberant environments," J. Acoust. Soc. Am. **120**(2), 838–851 (2006).
[13]J. V. Candy, A. W. Meyer, A. J. Poggio, and B. L. Guidry, "Time-reversal processing for an acoustic communications experiment in a highly reverberant environment," J. Acoust. Soc. Am. **115**(4), 1621–1631 (2004).
[14]S. Yon, M. Tanter, and M. Fink, "Sound focusing in rooms: The time-reversal approach," J. Acoust. Soc. Am. **113**(3), 1533–1543 (2003).
[15]C. B. Wallace and B. E. Anderson, "High-amplitude time reversal focusing of airborne ultrasound to generate a focused nonlinear difference frequency," J. Acoust. Soc. Am. **150**(2), 1411–1423 (2021).
[16]J.-L. Thomas, F. Wu, and M. M. Fink, "Time reversal focusing applied to lithotripsy," Ultrason. Imaging **18**(2), 106–121 (1996).
[17]G. Ribay, J. de Rosny, and M. Fink, "Time reversal of noise sources in a reverberation room," J. Acoust. Soc. Am. **117**(5), 2866–2872 (2005).
[18]C. Draeger and M. Fink, "One-channel time-reversal in chaotic cavities: Theoretical limits," J. Acoust. Soc. Am. **105**(2), 611–617 (1999).
[19]A. Derode, A. Tourin, and M. Fink, "Limits of time-reversal focusing through multiple scattering: Long-range correlation," J. Acoust. Soc. Am. **107**(6), 2987–2998 (2000).
[20]M. H. Denison and B. E. Anderson, "Time reversal acoustics applied to rooms of various reverberation times," J. Acoust. Soc. Am. **144**(6), 3055–3066 (2018).
[21]J. B. Allen and D. A. Berkley, "Image method for efficiently simulating small-room acoustics," J. Acoust. Soc. Am. **65**(4), 943–950 (1979).
[22]F. Ma, J. Chen, J. H. Wu, and H. Jia, "Realizing broadband sub-wavelength focusing and a high intensity enhancement with a spacetime synergetic modulated acoustic prison," J. Mater. Chem. C **8**(28), 9511–9519 (2020).
[23]F. Ma, J. Chen, and J. H. Wu, "Experimental study on performance of time reversal focusing," J. Phys. D Appl. Phys. **53**(5), 055302 (2020).
[24]M. Kleiner and J. Tichy, *Acoustics of Small Rooms* (CRC, New York, 2017), pp. 37–99.
[25]M. L. Willardson, B. E. Anderson, S. M. Young, M. H. Denison, and B. D. Patchett, "Time reversal focusing of high amplitude sound in a reverberation chamber," J. Acoust. Soc. Am. **143**(2), 696–705 (2018).
[26]M. K. Rollins, T. W. Leishman, J. K. Whiting, E. J. Hunter, and D. J. Eggett, "Effects of added absorption on the vocal exertions of talkers in a reverberant room," J. Acoust. Soc. Am. **145**(2), 775–783 (2019).
[27]M. R. Schroeder, "The 'Schroeder frequency' revisited," J. Acoust. Soc. Am. **99**(5), 3240–3241 (1996).
[28]B. E. Anderson, M. Clemens, and M. L. Willardson, "The effect of transducer directivity on properties of time reversal focusing," J. Acoust. Soc. Am. **139**(4), 2083–2083 (2016).
[29]B. Van Damme, K. Van Den Abeele, Y. Li, and O. Bou Matar, "Time reversed acoustics techniques for elastic imaging in reverberant and non-reverberant media: An experimental study of the chaotic cavity transducer concept," J. Appl. Phys. **109**, 104910 (2011).
[30]H. Kuttruff, *Room Acoustics*, 6th ed. (CRC, Boca Raton, FL, 2017), pp. 66–69.
[31]M. R. Schroeder and K. H. Kuttruff, "On frequency response curves in rooms: Comparison of experimental, theoretical, and Monte Carlo results for the average frequency spacing between maxima," J. Acoust. Soc. Am. **34**(1), 76–80 (1962).
[32]ISO 3741:2010, "Sound power and energy in reverberant environments" (International Organization for Standardization, Geneva, Switzerland, 2010).
[33]M. R. Schroeder, "New method of measuring reverberation time," J. Acoust. Soc. Am. **37**(3), 409–412 (1965).
[34]M. Tanter, J. Thomas, and M. Fink, "Time reversal and the inverse filter," J. Acoust. Soc. Am. **108**(1), 223–234 (2000).

Appendix D

The physics of knocking over LEGO minifigures with time reversal focused vibrations for use in a museum exhibit

Lucas Barnes was an undergraduate researcher developing an exhibit of time reversal focusing that was successfully assembled as an exhibit in a museum about waves in Switzerland. This author assisted in testing the experimental setup as well as developing the tools within the time reversal software to test a variety of configurations. This appendix is an article published as L. A. Barnes, B. E. Anderson, P.-Y. Le Bas, A. D. Kingsley, A. C. Brown, and H. R. Thomsen, "The physics of knocking over LEGO minifigures with time reversal focused vibrations for use in a museum exhibit," *J. Acoust. Soc. Am.* **151**(2), 738 (2022); https://doi.org/10.1121/10.0009364. It is reprinted in this dissertation under the terms of ASA's Transfer of Copyright Agreement, item 3. I hereby confirm that the use of this article is compliant with all publishing agreements.

JASA ARTICLE

The physics of knocking over LEGO minifigures with time reversal focused vibrations for use in a museum exhibit[a)]

Lucas A. Barnes,[1] Brian E. Anderson,[1,b)] Pierre-Yves Le Bas,[2] Adam D. Kingsley,[1] Aaron C. Brown,[1] and Henrik R. Thomsen[3]

[1]*Acoustics Research Group, Department of Physics and Astronomy, Brigham Young University, N283 Eyring Science Center, Provo, Utah 84602, USA*

[2]*Detonator Science and Technology (Q-6), Los Alamos National Laboratory, MS D446, Los Alamos, New Mexico 87545, USA*

[3]*Department of Earth Sciences, Eidgenössische Technische Hochschule Zürich, Zürich 8092, Switzerland*

ABSTRACT:

Time reversal (TR) is a method of focusing wave energy at a point in space. The optimization of a TR demonstration is described, which knocks over one selected LEGO minifigure among other minifigures by focusing the vibrations within an aluminum plate at the target minifigure. The aim is to achieve a high repeatability of the demonstration along with reduced costs to create a museum exhibit. By comparing the minifigure's motion to the plate's motion directly beneath its feet, it is determined that a major factor inhibiting the repeatability is that the smaller vibrations before the focal event cause the minifigure to bounce repeatedly and it ends up being in the air during the main vibrational focal event, which was intended to launch the minifigure. The deconvolution TR technique is determined to be optimal in providing the demonstration repeatability. The amplitude, frequency, and plate thickness are optimized in a laboratory setting. An eddy current sensor is then used to reduce the costs, and the impact on the repeatability is determined. A description is given of the implementation of the demonstration for a museum exhibit. This demonstration illustrates the power of the focusing acoustic waves, and the principles learned by optimizing this demonstration can be applied to other real-world applications.

https://doi.org/10.1121/10.0009364

(Received 22 September 2021; revised 5 January 2022; accepted 7 January 2022; published online 3 February 2022)

[Editor: James F. Lynch] Pages: 738–751

I. INTRODUCTION

Time reversal (TR) is a wave focusing method, which can be used to achieve spatial focusing.[1–3] The process involves reversing an impulse response obtained between two points in space and emitting it from one of these locations such that the waves constructively interfere at the other location. In fact, the time reversed impulse response (TRIR) may be emitted from either location, and the same focusing signal will result at the other location because of the acoustic reciprocity in a linear, time-invariant environment.

TR was originally called matched signal processing and developed for underwater acoustic applications.[4,5] During the traditional TR process, waves sent through the system are affected by the transfer function of the system during the forward step (when the impulse response is obtained) and again during the backward step (the broadcast of the TRIR). This double filtering of the system (the matched signal process) decreases the spatial resolution of the TR focusing and introduces relatively high temporal sidelobes compared to the focus peak, which reduce the quality of focus. One solution to this issue is a TR method termed inverse filtering or deconvolution TR,[6–9] which compensates for the forward step transfer function prior to the backward step. This provides improved spatial and temporal confinement when the TR focusing is impulsive in nature but at the cost of a reduced TR focusing amplitude. Other uses include energy focusing, secure communications, and source imaging. As an example of energy focusing, TR has been used to focus ultrasonic waves to the location of kidney stones to break them into smaller pieces non-intrusively.[10,11] TR is used to generate high-amplitude energy focusing of loud audible sound in a room,[12] ultrasound to generate a difference frequency,[13] and to excite structures with focused sound.[14,15] In communications applications, TR is used to send a private message that would only be discernable at the target location, whereas elsewhere it would just sound like noise.[4,16–19] TR can also be used to image earthquakes[20–23] and aero-acoustic sources[24–26] by modeling the propagation of time reversed recordings. TR has been used in nondestructive evaluation applications to focus energy to various points of interest to locally quantify the nonlinear response of those points, which allows cracks and defects to be imaged because they are the sources of that nonlinear response.[3,27–29]

One demonstration of TR acoustics was presented by Fink[30] in 1999. In the demonstration, an array of loudspeakers and microphones were used, which is called a TR mirror, to record sounds, reverse them, and then focus the reversed sounds back to their source. If a person stood in front of the array and said "hello," the TR mirror would focus the sound as "olleh" back to the person's mouth,

[a)]This paper is part of a special issue on Education in Acoustics.

[b)]Electronic mail: bea@byu.edu, ORCID: 0000-0003-0089-1715.

https://doi.org/10.1121/10.0009364

where the sound originated. It is stressed in the paper that the sound is not just being retransmitted to spread out into the room like normal sound, and instead it converges only at the person's mouth via the constructive interference of waves generated by the loudspeaker array and the virtual array made up of the appropriately timed reflections from the room boundaries.

In another demonstration by de Mello *et al.*,[31] TR was used to focus the surface water waves in a tank. The border of the tank was lined with 148 transducers, which could record the incoming waves and then emit the reversed recordings of them. For their TR experiments, first, an object was dropped into the tank as an impulsive source of the surface waves. The transducers recorded the reflections of the waves off of the sides of the tank and then after the water had settled, the reversed recordings were broadcast, causing the waves to converge at the original source location and create a focused motion of the surface, which was clearly visible to observers.

More recently, Heaton *et al.*[32] developed a visual demonstration of TR focused vibrations in a thin plate. A single vibration speaker or shaker was used to excite the vibrations in the plate after which a scanning laser Doppler vibrometer (SLDV) was used to quantify the reverberation time and vibration coupling efficiency from the shaker to the plates. The various plate materials were tested to explore the possible spatial confinement of the TR focus as well as the highest focal amplitude possible in the different plates. They found that glass, while fragile, provided the highest coupling efficiency and focal amplitude at the lowest cost, whereas aluminum provided results that were nearly as good while being much more durable. To demonstrate the focusing visually, salt was distributed on the plate. Using a slow-motion camera, the observers could then see the salt thrown off the plate at the location and time of the focus, whereas the salt elsewhere on the plate stayed mostly in contact with the plate during the focus. Additionally, some small objects, such as cardboard cylinders, wooden corks, and LEGO minifigures, could be placed at the focal location and knocked over (fall onto ones side) during the focus but not knocked over when placed away from the focal location. However, the ability to knock over the target object was not repeatable enough to use for a consistent demonstration (this is known because B.E.A. was a coauthor on the work of Heaton *et al.*[32]). Their work focused mainly on achieving the highest possible focal amplitude for the purpose of creating a visual demonstration of TR focusing, but they did not optimize the repeatability of knocking over small objects at the focal location. This resulted in a very loud and shrill sounding demonstration, which sometimes launched an object, such as a minifigure, several centimeters into the air before falling over and sometimes only made the object rattle on top of the plate, but it would remain standing.

This paper expands on the results of Heaton *et al.*[32] to create a more repeatable, interactive, user-friendly demonstration of TR focusing for a museum exhibit. Because the demonstration would be in an exhibition hall, reducing the audible noise of the demonstration was also a goal. A 100% reliable means of knocking over a target LEGO minifigure while leaving surrounding minifigures standing is determined in this work by using the TR inverse filter (or deconvolution) method at an optimal excitation level from the multiple shakers. Previously, the repeatability of knocking over a target LEGO minifigure with TR acoustics in a thin aluminum plate was around 30%, which was not previously reported by Heaton *et al.* An explanation is given here for why the target minifigure might not be knocked over despite a sufficiently large TR focal amplitude. The work of Heaton *et al.* focused on obtaining the largest possible peak focal amplitude through the use of the clipping TR (a variant of one-bit TR[33,34]), whereas, here, it is shown that the higher temporal quality of the TR focusing obtained with the deconvolution TR is critical to the successful repeatability of this demonstration. Additionally, a much less expensive noncontact vibration sensor is used to make the demonstration more practical in its implementation.

This paper will first describe the physics behind the main issue with creating a repeatable demonstration. A discussion of the experiments conducted to optimize the demonstration will then be given. The optimal plate thickness, frequency bandwidth, and input voltage to the shakers are explored. Then the use of an eddy current sensor (ECS) instead of a laser Doppler vibrometer is optimized. This paper explores the use of a velocity sensor versus using a displacement sensor to create the TR focusing of the plate's velocity or displacement. Finally, the details are provided about how the demonstration was adapted for an exhibit at a wave propagation museum, which is planned to be hosted at ETH University in Zurich, Switzerland.

II. UNDERSTANDING THE TR LEGO DEMONSTRATION

The experimental setup used to create the results discussed in this section and Fig. 1 consists of a 1.27 mm thick aluminum plate which is elevated 2 cm above an optical table by four rubber stoppers placed at the corners of the plate. Custom LabVIEW software (Austin, TX) is used to create a logarithmic chirp signal with a bandwidth of 100–2000 Hz, which lasts 0.5 s with 0.3 s of leading zeros and 0.2 s of trailing zeros. A 14-bit 4-channel Spectrum M2i.6022-exp generator card is used to output the chirp signal to one Mighty Dwarf 7W shaker (Milton, ON, Canada). The acquisition is done with a Polytec PSV-400 SLDV (Baden-Württemberg, Germany) and a 16-bit 4-channel Spectrum Instrumentation GmbH M2i.4931-exp digitizer card (Grosshansdorf, Germany) with a sampling frequency of 30 kHz. The SLDV is mounted above the plate and aimed at a patch of retroreflective tape on top of the plate. The impulse response is measured, normalized, and reversed in time and then any additional signal processing techniques, such as the clipping TR or deconvolution TR, are implemented. Finally, the resultant signal is broadcast from the shaker, creating a focus at the location where the SLDV measured the impulse response.

Heaton *et al.*[32] used the clipping TR and deconvolution TR together in an attempt to generate the largest focal amplitude possible, thinking that this was the only important

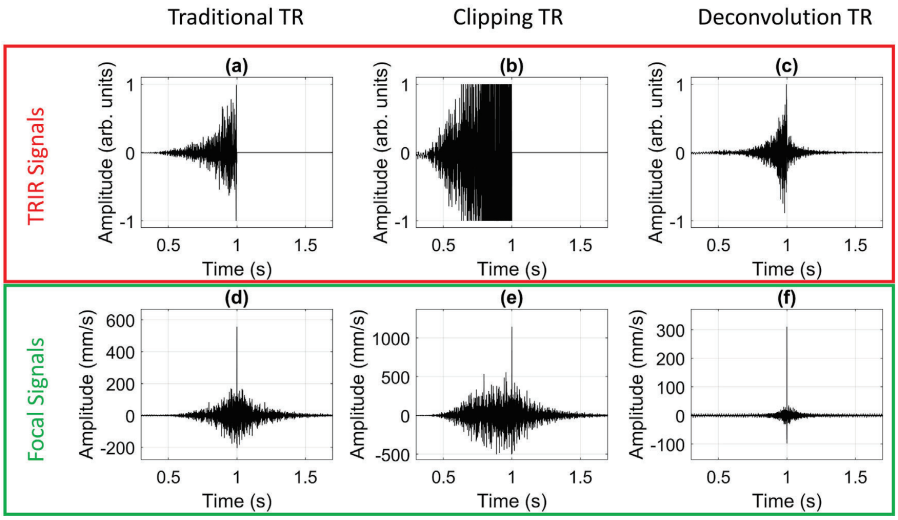

FIG. 1. (Color online) The TRIRs, including the modified ones, are displayed in the (a) traditional TRIR, (b) clipping TRIR, and (c) deconvolution TRIR. The focal signals obtained with these respective TRIR signals are displayed in the (d) traditional TR focus, (e) clipping TR focus, and (f) deconvolution TR focus. Note the differences in the ranges of the ordinate axes of the focal signals in (d)–(f).

goal for a repeatable demonstration of the localized focusing. However, as will be presented in this section, there were problems with the technique they used. To illustrate these issues, we will discuss the basics of the traditional TR, clipping TR, and deconvolution TR and discuss a critical finding that was made, which helped explain why the method used by Heaton *et al.* was not optimal for high repeatability. Their technique launches LEGO minifigures very high into the air but it is not very repeatable. The deconvolution TR technique can be used to obtain high repeatability of launching the LEGO but perhaps not quite with the same altitude. We will repeat the technique used by Heaton *et al.* along with some further measurements to illustrate its flaws along with similar measurements on the optimal deconvolution TR technique.

A. Traditional TR

In the traditional TR, a signal $s(t)$ is broadcast from a source into a system. A convolution of $s(t)$ with the impulse response of the system, $h(t)$, represents the response signal, $r(t)$, which would be recorded at some receiver location in the system

$$s(t) * h(t) = r(t). \tag{1}$$

If $s(t)$ is an impulsive signal, such as a delta function, $\delta(t)$, then $r(t) = h(t)$, and it can be used with further signal processing to achieve different types of TR focusing. Although this direct measurement of $h(t)$ seems theoretically easy to accomplish, it is difficult for realistic sources to produce a perfect impulse and attempts to do so result in a poor signal-to-noise ratio. Instead, the chirp method is used to indirectly obtain the impulse response.[35,36] In this method, a chirp or sweep through a range of frequencies is broadcast into the system as $s(t)$. The response to the chirp, $r(t)$, can then be –cross correlated with the chirp to produce a band limited impulse response, $h(t)$.

Once $h(t)$ is obtained, reversing it in time and broadcasting $h(-t)$ into the system yields

$$h(-t) * h(t) = y(t), \tag{2}$$

meaning that $y(t)$ is an autocorrelation result—a time-symmetric signal with a peak at the center—which corresponds to the peak focused amplitude that is characteristic of the TR process.[6] The method just described, simply broadcasting an unmodified $h(-t)$ is what we will refer to as the traditional TR. Two variants of TR, which were mentioned in the Introduction, the clipping TR and deconvolution TR, will now be described.

B. Clipping TR

The aim of the clipping TR method is to maximize the peak amplitude delivered to the focal location. The method is similar to the traditional TR except that before the reversed and normalized impulse response is broadcast into the system, a clipping threshold C is defined between zero and one. Then, every data point in the normalized impulse response that has a value $>C$ is set equal to C and every data point that has a value $< -C$ is set equal to $-C$. The clipped signal is then normalized such that the clipped portions of the signal are at ± 1. The clipping of the signal alters the amplitude of the wave arrivals in the impulse response, but the timing of the waves is still preserved. Thus, the

https://doi.org/10.1121/10.0009364

waves that are emitted in this clipped TRIR have a much larger relative amplitude than when using a traditional TRIR, and the amplitude is increased at the focal location. Figure 1 shows a comparison between a traditional TRIR in Fig. 1(a) and a clipping TRIR in Fig. 1(b) along with their corresponding focal signals, Figs. 1(d) and 1(e), respectively. As seen in a comparison of the signals displayed in Figs. 1(d) and 1(e), the clipping TR method creates a higher peak amplitude focus but at the cost of a lower signal-to-noise ratio (the peak amplitude compared to the amplitudes elsewhere).

C. Deconvolution TR or inverse filtering

The deconvolution or inverse filtering TR method seeks to maximize the signal-to-noise ratio of the focal signal by compensating for the resonances of the system. When the chirp signal described previously is broadcast into the system, its frequency content is affected by the resonances of the system transfer function, $H(f) = \mathcal{F}\{h(t)\}$, where $\mathcal{F}$ represents a Fourier transform operation. During the traditional TR, with an impulsive signal, the focal signal is equivalent to an autocorrelation of $h(t)$ or an autospectrum of $H(f)$. This means that the system resonances impact the focal signal during the forward and backward steps of the TR, hence, this is why the TR was originally called a matched signal process.[4,5] To compensate for these resonances, the inverse filter (or inverse transfer function) of the system $H^{-1}(f)$ is computed and then transformed into the time domain, normalized, time reversed, and broadcast into the system. When this modified impulse response is sent into the system, the inverse filter mixes with the resonances of the system, resulting in a relatively constant frequency response,

$$H(f)^{-1} * H(f) = 1. \tag{3}$$

The inverse filter or deconvolution TRIR [Fig. 1(c)] results in a focal signal with a lower peak amplitude than the traditional TR but yields a much better signal-to-noise ratio [Fig. 1(f)] than was achieved with the traditional TR or clipping TR.

D. TR technique optimization for high repeatability

Both the clipping TR and deconvolution TR were combined by Heaton *et al.*[32] by first calculating the deconvolution TRIR and then applying the clipping TR method to that signal before broadcasting it. This was used to achieve a moderately clean focus signal but with a higher peak amplitude focus than in the results with the deconvolution TR by itself. Despite having a high amplitude focus that could easily knock over a LEGO minifigure (an example result is shown in Fig. 2), an attempt to replicate the experiment using this method and a somewhat lower input amplitude and a thinner plate, resulted in a repeatability of 45% in the success rate of knocking over the target LEGO minifigure when performed on an aluminum plate with 2 shakers for a set of 40 trials. The LEGO minifigure might be launched up to 4 cm into the air before falling down 45% of the time. The rest of the time, the target LEGO minifigure would visibly vibrate (rattle on the plate surface) and rotate a bit, but it would not be launched into the air and instead would remain standing. The thickness of the plate used in these experiments, 1.27 mm, was smaller than that of the plates used in Heaton's experiments, which contributed to a slightly higher repeatability than the approximate 30% repeatability that Heaton *et al.* experienced. The optimization of the plate thickness is discussed in Sec. III.

To understand the reason for this low degree of repeatability, a SLDV was aimed at the top of a target LEGO minifigure's feet to measure the velocity over time of the minifigure during a broadcast of the TRIR. Then the experiment was repeated with the SLDV aimed to measure the velocity of the plate below its feet. The plate velocity recorded during the deconvolution plus the clipping TR and during deconvolution TR focusing is shown in Figs. 3(a) and 3(b), respectively. The velocity of the minifigure's feet during each of these focusing events is shown in Figs. 3(c) and 3(d), respectively. In Fig. 3(c), there are several abrupt increases in the velocity with each followed by a consistent downward sloping velocity, whose slope corresponds to the acceleration resulting from the gravity. Thus, it was discovered that the minifigure was repeatedly losing contact with the top of the plate for just a few milliseconds at a time but with enough vertical displacement from the plate to often miss the main focal event entirely. This discovery led to the critical understanding that if the smaller vibrations leading up to the focal event (termed sidelobes in the TR literature) were high enough in amplitude, they would cause the minifigure to lose contact with the plate and, thus, decrease the

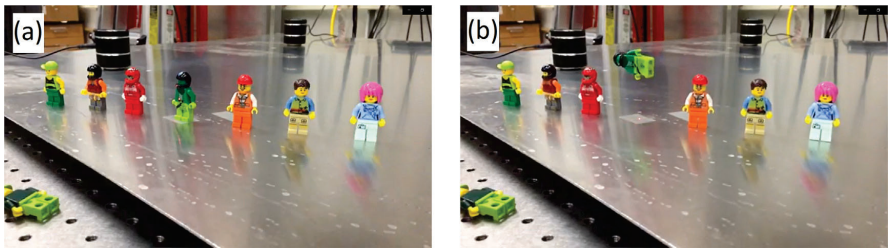

FIG. 2. (Color online) The (a) setup of the LEGO demonstration with two shakers in the background and the SLDV aimed (from above the plate) at the minifigure in the middle and (b) airborne minifigure after the focus are shown.

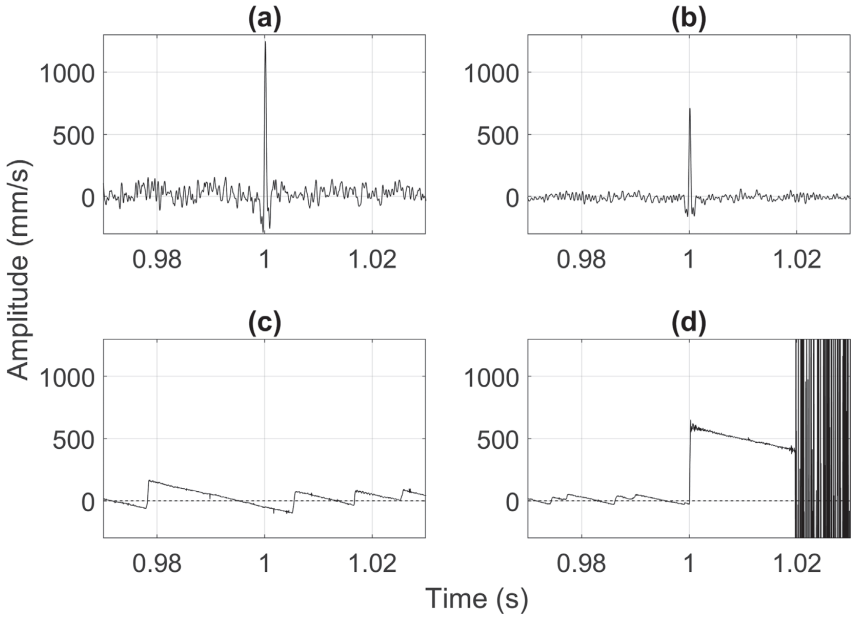

FIG. 3. The (a) plate velocity during the deconvolution plus the clipping TR focusing, (b) plate velocity during the deconvolution TR focusing, (c) LEGO minifigure velocity measured at their feet during the deconvolution plus clipping TR, and (d) LEGO minifigure velocity measured at their feet during the deconvolution TR are shown.

chances of the minifigure being knocked over by the main focal event.

With this understanding in mind, it is clear that a better approach to increasing the repeatability of the demonstration is to use the cleanest TR method possible, such as only deconvolution the TR without any clipping to minimize the amplitude of the sidelobes while maintaining enough amplitude in the focus to launch the minifigure. The repeatability experiment was performed again, this time only using the deconvolution TR, and the resulting repeatability was 75% for a set of 40 trials. Figure 3 shows a comparison between the clipping TR and deconvolution TR focal signals and examples of how the LEGO minifigures react to those signals. All further experiments discussed use the deconvolution TR.

III. OPTIMIZING THE DEMONSTRATION IN A LABORATORY

A set of experiments were designed and performed to optimize the parameters of the demonstration for increased repeatability. These included the plate thickness, chirp frequency range and bandwidth, and TRIR amplitude.

A. Plate thickness

While Heaton *et al.*[32] explored the use of different types of plate materials for the demonstration, the thickness of the plate was not previously explored. The TR experiments were performed on three different aluminum plates, whose thicknesses were 6.35 mm, 3.18 mm, and 1.27 mm. The dimensions of the 6.35 mm and 3.18 mm thick plates were 0.91 m × 1.22 m. The 1.27 mm thick plate was initially the same dimensions but was cut and bent into the shape of a bridge, which is the same shape that was used in the museum exhibit. The plate thickness is expected to play a more significant role in the trends observed than the plate's shape or area. Four shakers were used with their amplification settings at maximum on each plate along with a chirp bandwidth of 100–2000 Hz. The shakers were placed near the corners of the plate, but the shaker position was not explored in detail. Two metrics were used to quantify the results: temporal quality and peak amplitude. For these experiments, the temporal quality is defined[32,37] as

$$\xi_T = \frac{[A_P]^2}{\sqrt{\frac{1}{M}\sum_{m=1}^{M}\left[A(x_0, y_0, z_0, m)\right]^2}}, \tag{4}$$

where A_P is the peak amplitude at the focus location, $A(x_0, y_0, z_0, m)$ is an amplitude measurement at the focal location, (x_0, y_0, z_0), at a given time sample m, and M is the total number of time samples in the signal. ξ_T provides a relative indication of the focal amplitude as compared to the sidelobe amplitudes. Because high amplitude sidelobes are undesirable, a high ξ_T is desired. As the plate thickness decreased, several trends were noticed. As indicated in Table I, the smaller plate thickness yields both a higher peak

JASA
https://doi.org/10.1121/10.0009364

TABLE I. The experimentally obtained results when using TR in the different thickness aluminum plates for the peak amplitude of the TR focusing, A_P, and temporal quality, ξ_T.

Thickness (mm)	A_P (mm/s)	ξ_T
6.35	96	60.2
3.18	662	69.4
1.27	1490	73.9

amplitude as well as a higher temporal quality, which are both desirable traits for the TR focusing.

Another noticeable trend was that when the demonstration uses a thicker plate, the sound radiated by the plate is louder and has a shrill sound quality, which is undesirable for the demonstrations. The bending waves (or zeroth-order, antisymmetric Lamb waves) in the plate, which are assumed to dominate in these experiments, are dispersive. The phase speed of these bending waves, c_b, is proportional to the square root of the frequency, f (and angular frequency, $\omega = 2\pi f$), and proportional to the square root of the plate thickness, h,

$$c_b = \left(\frac{\omega^2 E h^2}{12\rho(1-\nu^2)}\right)^{1/4}, \tag{5}$$

where E is Young's modulus, ρ is the mass density, and ν is Poisson's ratio.[38] The expected wave speeds for the three plates studied are all subsonic (slower than the speed of sound in air) with the exception of the wave speeds in the 6.35 mm plate above 1880 Hz. As the bending wave speed increases, the radiation efficiency of the sound generated by these waves traveling in the plate generally increases (for the subsonic wave speeds).[38] This is the reason why thicker plates and higher frequencies are heard better and result in a shrill sound quality because of the higher bending wave speeds. Thus, the thinner plates are more desirable for the museum demonstration because the noise made by the demonstration can be annoying for users and others nearby. However, if the plate is too thin, then it is not structurally stable enough to support the weight of the equipment for the demonstration. From these experiments, it was concluded that the 1.27 mm thick plate was optimal.

B. Frequency range and bandwidth

Next, the interaction between the plate and target LEGO minifigure was optimized. When the downward acceleration of the plate underneath the minifigure exceeds the acceleration due to gravity, the minifigure loses contact with the plate. Thus, if the downward acceleration exceeds 9.8 m/s^2 just prior to the TR focusing peak, then the minifigure is not maximally launched into the air, leading to the repeatability problem described in Sec. II. Thus, reducing the acceleration of the plate prior to the arrival of the focusing peak increases the amount of time that the minifigure is in contact with the plate and the likelihood that the minifigure will be hit by the main focal peak and be launched off of the plate. The acceleration amplitude, $a(t)$, in a time-harmonic motion is a function of the velocity amplitude, $v(t)$, and angular frequency, ω,

$$a(t) = \omega v(t). \tag{6}$$

A parametric study was conducted on the amplitude, frequency range, and bandwidth to find the optimal values for both of these parameters. The optimal values of the amplitude, frequency range, and bandwidth are defined as the values that lead to the target minifigure being knocked over most repeatably while leaving the other nontarget minifigures on the plate standing. There are trade-offs, however, with the amplitude and frequency. Lower amplitudes and lower frequencies decrease the acceleration of the plate, but the amplitude still needs to be high enough to launch the target minifigure during the main focal event, and high frequencies are desirable because they increase the spatial confinement of the TR focusing, reducing the likelihood of the nearby minifigures being knocked over.

First, repeatability as a function of the frequency range of the chirp signal was studied, i.e., whether low, mid, or high frequencies are most important. These repeatability experiments were conducted with a set of fixed frequency bandwidths (each of 1000 Hz), but the range of the frequencies was changed (the starting and ending frequencies were changed by the same amounts). The chirp signal used to get the impulse response was set to a fixed bandwidth of 1000 Hz. A set of 40 trials were performed for each of the 12 different frequency ranges with the starting frequencies ranging from 100 to 1200 Hz in 100 Hz intervals [Fig. 4(a) gives the starting and ending frequencies for all of the ranges tested]. These experiments were performed on a 0.91 m × 1.22 m × 1.27 mm aluminum plate with four shakers and a SLDV. In an individual trial, the forward and backward steps of the TR were conducted and then a LEGO minifigure was placed at the focal location to see if it would be knocked over. Nine additional minifigures were placed at other locations on the plate at least 10 cm away from the shakers and the focal location. A successful trial was one in which the target minifigure was knocked over (fell down). The results of these fixed-bandwidth, varying-range experiments are shown as percentages of the success (repeatability) in Fig. 4(a) with 100% meaning that the target minifigure was knocked over 40 out of 40 times. Note that the results in Fig. 4(a) represent $12 \times 40 = 480$ individual trials of the demonstration. The results indicate that the 1000 Hz ranges at the lower frequencies were more effective in launching the target minifigure, and the success rate (or repeatability) dropped off quickly as the frequency increased.

To explore the effects of varying the bandwidth with a fixed starting frequency, 40-trial repeatability experiments were performed for 9 different bandwidths with each starting at 100 Hz but ending at frequencies ranging from 400 Hz to 10 kHz. Figure 4(a) shows that the lower frequency ranges are better, but Fig. 4(b) shows that the inclusion of

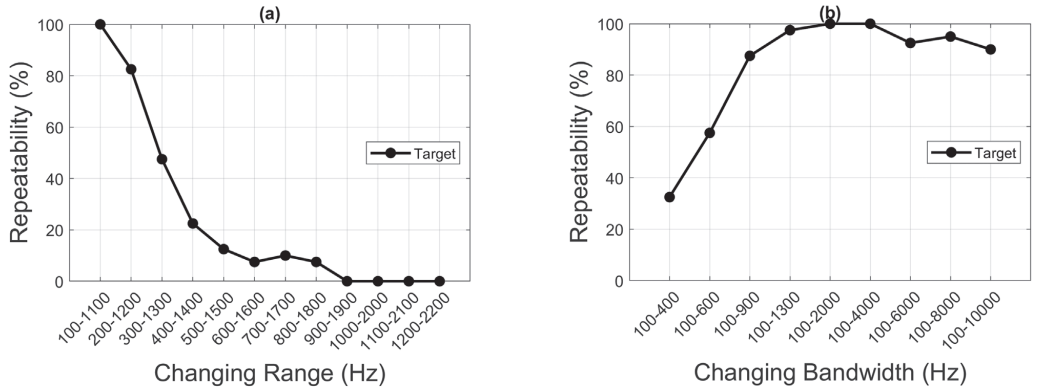

FIG. 4. The repeatability tests of the demonstration. Each data point represents the success rate (repeatability percentage) from 40 trials to knock over the target minifigure. The (a) repeatability when using various fixed frequency bandwidths of 1000 Hz while varying the range of the frequencies, and (b) repeatability when varying the bandwidth are depicted.

the higher frequency content (a wider bandwidth) increases the repeatability.

C. TRIR amplitude

Next, a similar set of repeatability experiments were conducted for the different TRIR broadcast amplitudes to understand the effect of the amplitude on the repeatability of the demonstration. At this point, the 1.27 mm thick plate had been cut and bent into the shape of a bridge because the museum demonstration would use a bridge-shaped plate (one potential application of TR, which visitors could understand, is to detect and locate cracks in bridges and other structures). The TR experiments were performed starting with a low amplitude TRIR, which rarely knocked over the target minifigure and was not strong enough to ever knock any of the other minifigures over. For each of 12 different input amplitudes, 40 trials were performed. These repeatability results are shown in Fig. 5. The SLDV was again used along with a frequency bandwidth of 100–2000 Hz.

Although the specific input voltages greatly depend on the instrumentation used, the experimental results in Fig. 5 illustrate that a certain amplitude threshold is needed to repeatedly knock over the target minifigure. However, too much amplitude actually reduces the likelihood that the target will be knocked over and increases the likelihood of knocking over the other minifigures. The reduction of knocking over the target and the increase in knocking over nontarget minifigures can be explained by the higher amplitude sidelobes caused by a higher output amplitude from the shakers. The higher amplitude sidelobes can cause the target minifigure to be in the air when the main focal event happens, and the higher sidelobes will correspond to larger vibrations elsewhere in the plate, knocking over the nontarget minifigures. It is important to note that because the museum exhibit will only use two shakers, these repeatability versus amplitude experiments were done with two shakers, whereas the repeatability versus frequency experiments were done using four shakers. Using less shakers is the main reason why the highest repeatability achieved in these experiments was 92.5% (37/40) despite being performed with a bandwidth of 100–2000 Hz, which achieved 100% repeatability in the previous experiments [see Fig. 4(b)].

Based on the optimization experiments for the plate thickness, input amplitude, fixed bandwidth, and varying bandwidth, the optimal parameters for this specific setup with two shakers were determined to be 1.27 mm plate thickness, 1.5 V input amplitude to the shakers, and 100–2000 Hz frequency range for the chirp signal. With these optimal parameters, a repeatability of 92.5% was achieved. When using 4 shakers instead of 2 and an input voltage of 1 V, 100% repeatability was achieved for a set of 80 trials.

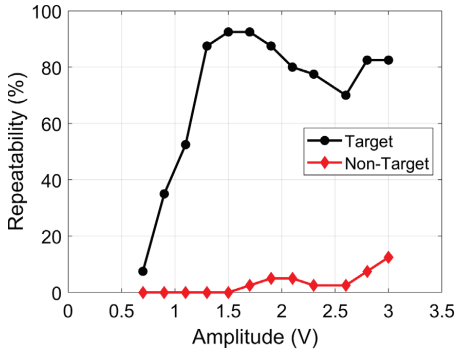

FIG. 5. (Color online) The repeatability of the demonstration when using different input amplitudes to the shaker sources. Here, the percentage of the times that the target minifigure was knocked over is tracked as well as the percentage of the times that the nontarget minifigures fell down. Each data point represents the success rate (repeatability percentage) for 40 trials conducted at each input amplitude. The SLDV was used here to create the velocity foci for these experiments.

JASA
https://doi.org/10.1121/10.0009364

IV. USING DIFFERENT SENSORS BETWEEN STEPS OF THE TR PROCESS

The SLDV was used for all of the laboratory experiments previously discussed, but it is too expensive to use in a practical demonstration setting such as the planned museum exhibit. The SLDV is a velocity sensor, meaning that throughout the usable frequency bandwidth of the SLDV, the voltage output is proportional to the velocity of the plate. The SLDV shines monochromatic light at a vibrating surface, and some of this light must be reflected back to the SLDV's detector. The vibrating surface dynamically changes the frequency of the reflected light as the surface moves because of the Doppler effect. A comparison between the incident light and reflected light yields the velocity amplitude as a function of the time.

One relatively inexpensive sensor that was still able to measure the 100–2000 Hz frequency range adequately was an ECS, which is a noncontact displacement sensor. The ECS uses an active coil of wire to generate an alternating magnetic field in the vicinity of a conducting surface. The magnetic field causes small electric currents, called eddy currents, to be induced in the conductive surface, in this case, an aluminum plate. These eddy currents oppose the excitation current and cause a drop in the voltage across the sensor, which is measured and converted to an output voltage that is proportional to the displacement between the plate and sensor head. An additional advantage of the ECS over the SLDV is its portability, which is useful for performing this demonstration in various venues with ease. The purpose of this section is to contrast the use of the ECS (approximate cost $1.3k USD), a displacement sensor, to that of the SLDV (approximate cost $250k USD), a velocity sensor, in the TR experiments.

The ECS sensor used here is a Micro-Epsilon DT3001-U8-A-SA eddy current measuring system (Ortenburg, Germany) with a sensing range of 8 mm from the ECS surface. Because the ECS outputs a voltage proportional to the displacement relative to the sensing head, the signal response has a direct current (DC) offset [Fig. 6(a)], corresponding to the overall distance between the plate and ECS. The DC offset was removed by subtracting the mean of the dynamic signal recordings as in the chirp response pictured in Fig. 6(b). The ECS measurement range corresponds to an output voltage range from 0.5 to 9.5 V. To allow for the motion of the plate toward and away from equilibrium, it is optimal to place the plate well within the measuring range such that the alternating current (AC) voltages will not exceed the dynamic range of the digitizer card. This ECS also picks up quite a bit of low frequency noise, therefore, a second-order Butterworth filter, which had a bandpass response between 100 and 2000 Hz, was used to filter the signal response, as shown in Fig. 6(c). After removing the DC offset and filtering the chirp response signal, the cross correlation is performed to obtain the impulse response.

Because the ECS is a displacement sensor, the impulse response obtained between the shaker and ECS is a displacement signal. Thus, the use of this impulse response results in a TR focus that has a displacement peak [Fig. 7(a)]. If this displacement focus is recorded using a velocity sensor, such as a SLDV, the signal would instead show up as the "*N*-shaped" time derivative of the displacement focus signal [Fig. 7(b)]. If a SLDV is used to obtain the impulse response, which is subsequently used to create a TR focus, a SLDV recording will show a standard symmetric TR focus, which has a velocity peak [Fig. 7(d)]. A displacement recording of that velocity TR focus will appear as a backwards *N*-shaped time integral of that focus signal [Fig. 7(c)].

It is conceivable that the ESC could be used to create a backwards *N*-shaped displacement focus signal, similar to the one in Fig. 7(c), by modifying the displacement impulse response. This would allow a peak velocity to be created during the focusing. One way to create a backwards *N*-shaped focus and mimic the phase shift that an integral imposes would be to introduce a phase shift of −90° at all frequencies in the spectrum of the TRIR. The displacement during this TR focusing would look similar to that pictured in Fig. 7(c), but the velocity would look like that pictured in Fig. 7(d). A velocity sensor could be used with a modified impulse response to create a focusing like that pictured in Fig. 7(b) to create a displacement peak in the focusing like that pictured in Fig. 7(a). Applying a 90° phase shift to the velocity TRIR would create a velocity signal like that shown

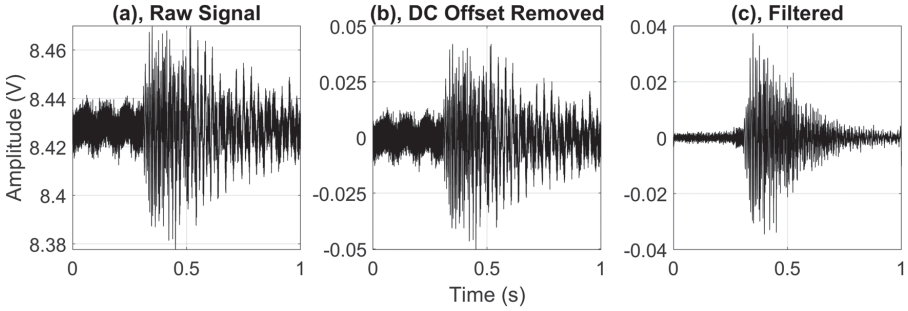

FIG. 6. The example signals recorded with the ECS. The (a) unfiltered chirp response with the DC offset, (b) unfiltered chirp response with the DC offset removed, and (c) filtered chirp response with the DC offset removed are shown.

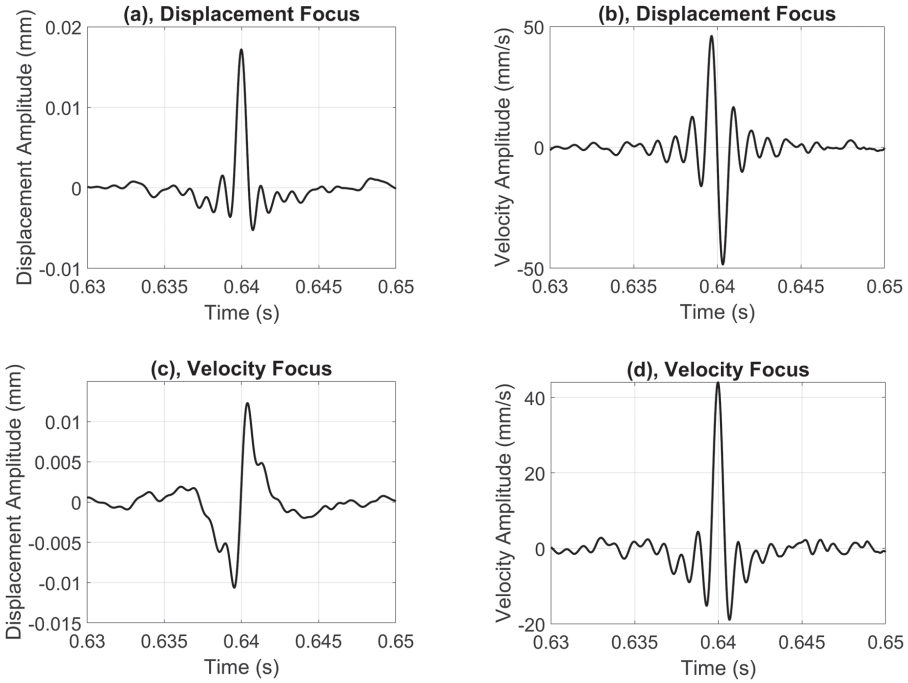

FIG. 7. The (a) displacement amplitude recording during the displacement TR focusing, (b) velocity amplitude recording during the displacement TR focusing, (c) displacement amplitude recording during the velocity TR focusing, and (d) velocity amplitude recording during the velocity TR focusing are shown.

in Fig. 7(b) during the TR focusing, whereas the displacement signal would look like that shown in Fig. 7(a). An accelerometer or another acceleration-based vibration sensor may also be used to create a displacement or velocity TR focus peak by applying a 180° or 90° phase shift to the TRIR, respectively. The authors verified that each of these experiments work as described by using the ECS and SLDV. A similar idea, called phase inversion or pulse inversion, introduced the idea of applying a 180° phase shift to the TRIR to create a symmetric, negative-value, TR focus peak.[39] Third-order phase symmetry analysis introduced the idea of implementing 120° and 240° phase shifts to the TRIR so that the 0°, 120°, and 240° phase shifted TRIR signals could be used to create three different focal signals, which may be combined in such a way to detect the presence of even or odd harmonics caused by the nonlinearities in a high amplitude TR focus.[40]

With the ability to create the different shaped focal signals comes the question of what focal shape will launch a LEGO minifigure the highest into the air to increase the chances of knocking over the minifigure? In Sec. III, it was found that the lower velocity and acceleration amplitudes were desirable to reduce the likelihood of the LEGO minifigure losing contact with the plate and being in the air when the focus peak arrives. The optimal, local motion of the plate would be a large upward velocity to give the minifigure a large upward momentum followed by a large downward acceleration (steep negative slope of velocity versus time) such that the minifigure would lose contact with the plate, and the plate would travel downward while the minifigure continued to rise further above the plate. The higher the minifigure travels, the more likely it will be to fall over on returning to the plate surface.

Because the displacement focus and velocity focus, measured in the velocity [Figs. 7(b) and 7(d), respectively], exhibit a large, positive-velocity peak followed by a large negative slope, it is expected that both types of foci could launch a LEGO minifigure. The experiments confirmed that a displacement focus and velocity focus were equally capable of launching the LEGO minifigure and knocking it over. In comparing Fig. 8 with Fig. 5, it can be seen that the ECS provided a similar overall repeatability trend as for the experiments performed with the SLDV in Sec. III with a set of 40-trial repeatability tests. These repeatability trials were also performed with only two shakers on the bridge-shaped plate as was performed with the SLDV repeatability versus amplitude trials. Using the ECS and two shakers on the bridge, the demonstration had a repeatability up to 92.5% (37/40) at an input voltage of 1.8 V to the shakers, which is the same maximum repeatability achieved with the SLDV and two shakers on the bridge. We expect that the findings for the plate thickness and general findings of the frequency optimization work hold when using the ECS instead of the SLDV. Some brief optimization checks were performed

https://doi.org/10.1121/10.0009364

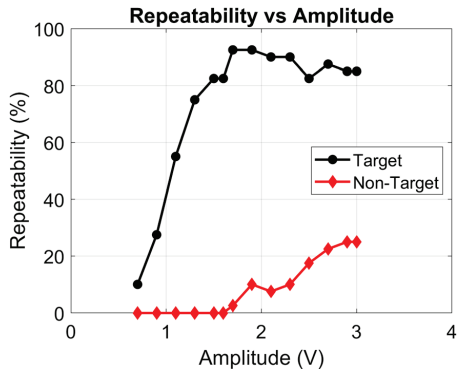

FIG. 8. (Color online) The repeatability of the demonstration when using different input amplitudes to the shaker sources. Here, the percentage of the times that the target minifigure was knocked over is tracked as well as the percentage of the times that the nontarget minifigures fell down. Each data point represents the success rate (repeatability percentage) for 40 trials conducted at each input amplitude. The ECS was used here to create the displacement foci for these experiments.

with the ECS to determine that the optimizations performed with the SLDV still held when using the ECS.

Whereas the low frequencies were found to contribute significantly to the successful launching of the target minifigure, they also have larger wavelengths and lead to a wider spatial focus. This is not desirable because a larger focal area will be more likely to knock over the nontarget minifigures. Because the ECS is more sensitive to the lower frequency motion than the SLDV, the spatial extent of the focusing was a concern. Also, as the ECS induces currents in the target material, the manufacturer states that the required sensing area is about 3–5 cm in diameter, which is much larger than the sensing area of the SLDV ($\sim$30 μm). This larger sensing area of the ECS also likely contributes to a wider focus. Heaton *et al.*[32] showed what the velocity profile of a velocity focus looks like. For comparison, in Fig. 9, the displacement profile of a displacement focus at the time of the maximal focusing using the ECS is shown. Note that

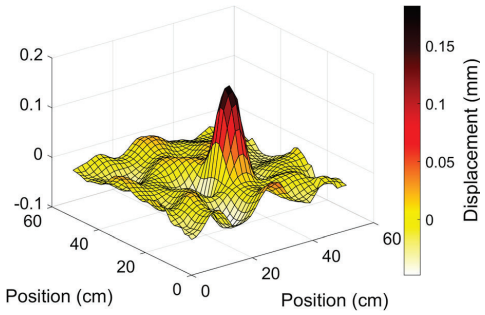

FIG. 9. (Color online) The surface plot of a displacement TR focus peak during the time of peak focusing. An ECS was used to obtain the impulse response and a SLDV was used to record the displacement at each scan position.

the scan area was 51 × 51 cm, and the flat, top surface of the bridge-shaped plate was 61 × 91 cm in area. The full width at half maximum of this displacement focus was determined to be 6.2 cm.

V. MUSEUM EXHIBIT

This section will focus on describing how the demonstration was made more practical and cheaper for the museum exhibit "Waves" at *focus*Terra, the Earth and Science Discovery Center of ETH Zurich, Switzerland.[41] The "Waves" exhibition showcases the many facets of wave phenomena in daily life.[42] The exhibition allows visitors to playfully and experimentally explore the characteristics of the waves and how they are used in nature and technology. Figure 10(a) shows a bird's eye view of the exhibition. TR is a great example of focusing energy via waves and, thus, the demonstration described and optimized throughout this work was a perfect fit for the "Waves" exhibition. The visitors are shown videos of the wave propagation during the forward (Mm. 1) and backward steps, focused to two different locations (Mm. 2 and Mm. 3, respectively) as obtained by a SLDV and slowed down for visualization purposes.

Mm. 1. Video presented to the museum visitor, which describes the forward propagation step of the demonstration during the broadcast of the chirp signals. A video of the vibrations as acquired with a scanning laser vibrometer is shown. This is a file of type "mp4" (9.3 MB).

Mm. 2. Video presented to the museum visitor, which describes the backward propagation step of the demonstration during the broadcast of the reversed impulse responses. A video of the vibrations as acquired with a scanning laser vibrometer is shown for the focus position A. This is a file of type "mp4" (8.0 MB).

Mm. 3. Video presented to the museum visitor, which describes the backward propagation step of the demonstration during the broadcast of the reversed impulse responses. A video of the vibrations as acquired with a scanning laser vibrometer is shown for the focus position B. This is a file of type "mp4" (7.5 MB).

For the museum exhibit setup, a bridge-shaped aluminum plate with a thickness of 1.5 mm and top surface measuring 91 cm × 61 cm was used. The bridge shape illustrates a possible application in which the TR may be used. Two Mighty Dwarf 7W shakers were placed at an offset at opposite ends of the bridge. Less output channels meant lower cost, but this also decreased the repeatability of the demonstration somewhat. The ECS was mounted on three computer-controlled FUYU FSL40 linear motion stages (Chengdu City, China) in the shape of an "*H*" so that the ECS can be translated in two dimensions underneath the plate and acquire the necessary displacement recordings.

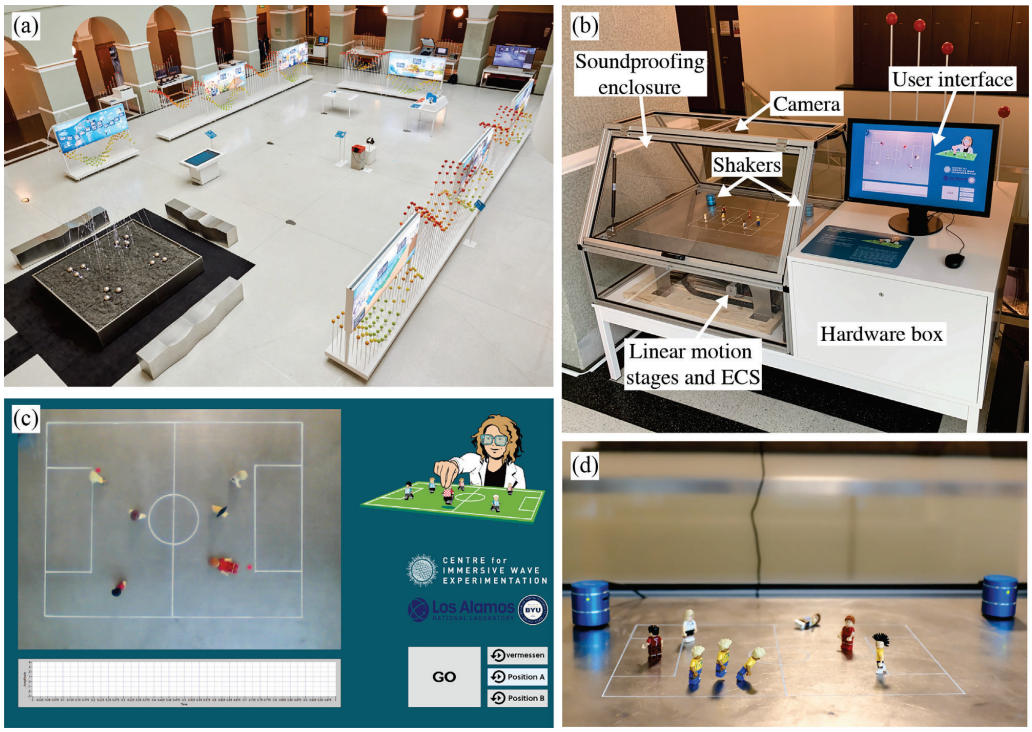

FIG. 10. (Color online) The (a) "Waves" exhibition at *focus*Terra (Courtesy of Matthias Auer of *focus*Terra), and (b) TR demonstration described in this work, found in the upper left corner of the exhibition [see (a)], are depicted. The aluminum table with the two shakers and LEGO minifigures is enclosed by a soundproofing enclosure. (c) The user interface requires the visitors of the museum to first select a LEGO minifigure on the soccer field and then press "GO." The ECS below the aluminum plate then records the impulse response at the location of the target minifigure while successively exciting the two shakers. After which, the TRIR is broadcast. (d) The overlay of the three consecutive photographs shows a targeted Lego minifigure jumping and falling due to the TRIR (courtesy of Matthias Auer of *focus*Terra).

The data acquisition and generation are managed with a National Instruments (Austin, TX) USB-6211 multifunction input/output device. This device had a lower amplitude resolution than the data acquisition cards used in the laboratory, and this reduced the temporal quality of the TR focusing somewhat, which reduced the repeatability some. The complete setup is shown in Fig. 10(b). A user interface, a screenshot of which is shown in Fig. 10(c), along with an overhead camera allows users to select a location on the plate where they want to create a TR focus. The translation stages underneath the plate then move the ECS to the selected location and a chirp is emitted in turn from each shaker while the ECS records the response between each shaker and the target location. The impulse responses are determined through filtering and cross correlation. Then, the ECS is moved away from the target location, and the two shakers simultaneously broadcast their respective TRIRs, creating a focus at the target location.

As shown in Figs. 10(b) and 10(c), the bridge is populated with LEGO minifigures, arranged to resemble two opposing soccer teams. The visitors to the museum exhibit then take turns trying to knock over the players of the other team using the TR focusing. The user interface, provides further information on how the TR aims to focus waves to a selected location and its application in science and industry. Moreover, the user can view three animations of the plate vibrations acquired with a SLDV system when sending the chirps and a TR focus at two fixed positions on the plate (the videos can be seen in Mm. 1–Mm. 3).

Of note is the Plexiglas enclosure covering the aluminum table visible in Fig. 10(b). The museum *focus*Terra is integrated into the Earth Science building. Thus, one requirement that the demonstration had to meet was to not disturb the students and employees working in the building. The findings introduced in this paper have allowed the demonstration to be much quieter than the previous version of the demonstration presented by Heaton *et al.*[32] The use of a thinner plate and reduced bandwidth both help to reduce the radiated noise. The deconvolution TR technique and the use of multiple shakers also allows smaller vibration amplitudes to be used while still yielding a sufficiently large focal amplitude to launch the minifigure. However, the noise broadcast by the shaker's interaction with the aluminum plate was still too loud. Consequently, a soundproofing

https://doi.org/10.1121/10.0009364

enclosure was designed and manufactured in cooperation with Kanya AG (Rüti, Switzerland) to ensure an acceptable noise emission. The enclosure can be opened at the front to allow users to place the minifigures on the soccer field (pitch). The camera is mounted at the top, directly above the soccer field. Moreover, 5 cm thick soni WAVE sound absorbing foam (Soniflex, Denmark), targeting sound absorption in the 400 Hz–5 kHz range) was attached to the lower back face (35×114 cm) and the face was adjacent to the hardware box (35×92 cm).

The sound pressure level (SPL) was then measured using the XL2 audio analyzer by NTI audio (Schaan, Liechtenstein) at a distance of 1 m and height of 1.5 m without and with the soundproofing enclosure present. Figure 11 shows a reduction in the SPL of 18.5 dB when emitting the chirps and a reduction in the SPL of 26.7 dB when the TRIR is introduced to the aluminum plate. As a result, using the soundproofing enclosure, the demonstration is quiet enough but still audible to the user when directly interacting with it. The latter point is important as it makes it easier for the user to establish the link between the waves and the focusing of energy.

The initial testing found that repeatable TR focusing results, i.e., the LEGO minifigure either jumping or falling, were only found when manually increasing the volume of the two Mighty Dwarf shakers to their maximum (this is required to do every time the shakers are powered on). However, this is not practical for an exhibition piece, which should require the least amount of maintenance possible. Thus, the output of the National Instruments USB-6211 (Austin, TX) is amplified by a Monacor SA-100 stereo amplifier (Bremen, Germany) prior to being sent to the Mighty Dwarf speakers. Also, in an effort to streamline the processing of the data, the experiment was tested without bandpass filtering the recordings. These factors led to a decrease in the repeatability compared to the repeatability of the laboratory demonstration at Brigham Young University (BYU), which was described previously. Further reduction in the repeatability was observed due to the user's accuracy when interacting with the demonstration and camera alignment precision. In other words, if the user does not exactly select where the target minifigure is or the positioning system for the ECS is not aligned with the camera view on the user interface, the target minifigure might not be standing at the exact TR focal spot.

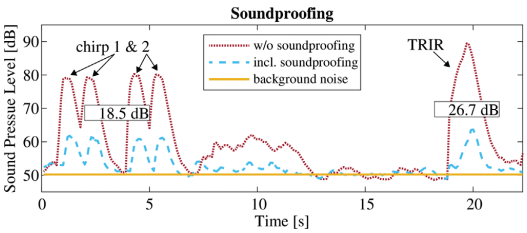

FIG. 11. (Color online) The difference in the sound pressure level as a function of time when covering the TR demonstration with a soundproofing enclosure. The (red) dotted line shows the measured SPL without the soundproofing enclosure. The (light blue) dashed line shows the drop in the SPL when covering the demonstration with the soundproofing enclosure. Each chirp is broadcast twice from each of the two shakers. After which, the TRIR signal is broadcast. A drop of 18.5 dB is measured for the chirps and 26.7 dB for the TRIR. Finally, the (yellow) line indicates the measured average background noise.

The settings for the exhibition are as follows. The chirp signals span a range from 100 Hz to 1.6 kHz and are played for a duration of 500 ms. Additionally, the signal measured by the ECS is averaged twice. It was found that the averaging leads to a better calculated TRIR as the ambient vibrations are a factor when the visitors interact with the exhibition. The amplitude of the TRIR emitted by the two shakers is 11.6 times as large as the amplitude of the initial chirps.

The repeatability was tested using these settings. Out of 40 trials, the target minifigure visibly jumped in the air 75% of the time but only fell over 30% of the time, and the nontarget minifigures were knocked over 15% of the time. However, because the demonstration is presented in a game format, a decreased repeatability is desirable because it adds an element of unpredictability, which makes it more fun for the users. Figure 10(d) shows an example of a jumping and falling soccer player. When compared with Fig. 2(b), the minifigure does not jump as high. However, the desired effect of playfully and experimentally demonstrating the focusing of the energy in a medium via waves is clearly conveyed to the user.

VI. CONCLUSION

This paper proves a better physical understanding and optimization of a demonstration of TR acoustics introduced by Heaton *et al.*[32] First, a comparison between the traditional TR, deconvolution TR, and clipping TR was presented. This led to the experimental discovery that large amplitude sidelobes were causing the target minifigure to bounce prematurely, sometimes causing it to be in the air during the main focal event and not be knocked over. This critical insight indicates that the best TR method to use for high repeatability in the demonstration is deconvolution because the deconvolution method leads to a better signal-to-noise ratio than is typical of traditional TR or clipping TR and, therefore, smaller sidelobes, while maintaining enough amplitude in the focus to launch the minifigure.

Several parameters of the setup and TR process were optimized, including the thickness of the plate, frequency range of the chirp, and amplitude of the TRIR. Three different plate thicknesses were studied, and it was found that the thinner plates yield higher peak amplitudes as well as a higher temporal quality. These are both desirable traits for a TR focal signal so long as the structure is strong enough to stand and support any required equipment. Additionally, less noise is radiated from the thinner plates because the waves are more likely to be traveling at subsonic speeds.

For the chirp frequency range optimizations, one set of repeatability experiments was performed while varying the upper bound of the chirp and holding the lower bound

constant, and another set of experiments were performed while holding the bandwidth constant and raising the lower and upper bounds of the chirp together. It was found that the lower frequencies are the most effective in knocking over the target minifigure, but the higher frequencies are also necessary to reduce the number of times the nontarget minifigures were knocked over by reducing the spatial extent of the focusing. In the end, the frequency range of 100–2000 Hz was determined to be optimal for the demonstration.

Another set of repeatability experiments was performed while varying the output amplitude of the TRIR. An important trade-off discovered was that there needs to be enough amplitude to knock over the target but too much amplitude would cause the sidelobes to be too large, and the minifigure could prematurely bounce into the air and miss the main focal event. Therefore, a balance must be found, but the specific amplitude will vary from setup to setup. The optimal parameters for our specific setup with two shakers were determined to be 1.27 mm plate thickness, 1.5 V input amplitude to the shakers, and 100–2000 Hz frequency range for the chirp signal. With these optimal parameters, a 92.5% repeatability for a set of 40 trials was achieved. Additionally, when using 4 shakers instead of 2 and an input voltage of 1 V, a 100% repeatability for a set of 80 trials was achieved.

The main differences in the state of the demonstration before and after the contributions of this paper are that the launch height of the minifigure is lower, which is quieter and much more repeatable, a cheaper sensor was implemented, and there are less nontarget minifigures falling over. These optimizations made the demonstration suitable for the implementation as an exhibit in a wave propagation museum at ETH Zurich in Switzerland. Due to the hardware limitations, the repeatability in the museum exhibit was 30%, which was lower than the repeatability found in the laboratory. Fortunately, the lower repeatability provides for a more fun game of chance, and the demonstration remains an effective way to visualize the focusing power of the TR acoustics.

Videos of the TR LEGO minifigure demonstration can be found in Refs. 43–45.

Reference 43 includes a description of the demonstration as narrated by B.E.A. Reference 44 shows the demonstration conducted in the BYU laboratory using an ECS, and illustrates the repeatability with these conditions. Reference 45 shows the focusing waves followed by the initial video of the first demonstration along with an optimal launch result as conducted in the BYU laboratory.

ACKNOWLEDGMENTS

The funding was provided by BYU College of Physical and Mathematical Sciences. The authors also thank the *focus*Terra team for the opportunity to include the TR demonstration in the "Waves" exhibition. Furthermore, the authors thank Thomas Haag for his technical assistance in getting the demonstration ready for the exhibition.

[1]M. Fink, "Time reversed acoustics," Phys. Today **50**(3), 34–40 (1997).
[2]B. E. Anderson, M. Griffa, C. Larmat, T. J. Ulrich, and P. A. Johnson, "Time reversal," Acoust. Today **4**(1), 5–16 (2008).
[3]B. E. Anderson, M. C. Remillieux, P.-Y. Le Bas, and T. J. Ulrich, "Time reversal techniques," in *Nonlinear Acoustic Techniques for Nondestructive Evaluation*, 1st ed., edited by T. Kundu (Springer and Acoustical Society of America, New York, 2018), Chap. 14, pp. 547–581.
[4]A. Parvulescu and C. S. Clay, "Reproducibility of signal transmission in the ocean," Radio Elec. Eng. **29**, 223–228 (1965).
[5]C. S. Clay and B. E. Anderson, "Matched signals: The beginnings of time reversal," Proc. Mtgs. Acoust. **12**, 055001 (2011).
[6]M. Tanter, J.-L. Thomas, and M. Fink, "Time reversal and the inverse filter," J. Acoust. Soc. Am. **108**(1), 223–234 (2000).
[7]M. Tanter, J. F. Aubry, J. Gerber, J.-L. Thomas, and M. Fink, "Optimal focusing by spatiotemporal filter. I. Basic principles," J. Acoust. Soc. Am. **110**, 37–47 (2001).
[8]T. Gallot, S. Catheline, P. Roux, and M. Campillo, "A passive inverse filter for Green's function retrieval," J. Acoust. Soc. Am. **131**, EL21–EL27 (2012).
[9]B. E. Anderson, J. Douma, T. J. Ulrich, and R. Snieder, "Improving spatio-temporal focusing and source reconstruction through deconvolution," Wave Motion **52**, 151–159 (2015).
[10]M. Fink, "Time-reversal acoustics in biomedical engineering," Annu. Rev. Biomed. Eng. **5**(1), 465–497 (2003).
[11]M. Fink, "Time reversal and phase conjugation with acoustic waves: Industrial and medical applications," Lasers Electro-Opt. **3**, 2334–2335 (2005).
[12]M. L. Willardson, B. E. Anderson, S. M. Young, M. H. Denison, B. D. Patchett, and T. Akal, "Time reversal focusing of high amplitude sound in a reverberation chamber," J. Acoust. Soc. Am. **143**(2), 696–705 (2018).
[13]C. B. Wallace and B. E. Anderson, "High-amplitude time reversal focusing of airborne ultrasound to generate a focused nonlinear difference frequency," J. Acoust. Soc. Am. **150**(2), 1411–1423 (2021).
[14]P.-Y. Le Bas, M. C. Remillieux, L. Pieczonka, J. A. Ten Cate, B. E. Anderson, and T. J. Ulrich "Damage imaging in a laminated composite plate using an air-coupled time reversal mirror," Appl. Phys. Lett. **107**, 184102 (2015).
[15]M. Farin, C. Prada, and J. de Rosny, "Selective remote excitation of complex structures using time reversal in audible frequency range," J. Acoust. Soc. Am. **146**(4), 2510–2521 (2019).
[16]G. F. Edelmann, H. C. Song, S. Kim, W. S. Hodgkiss, W. A. Kuperman, and T. Akal, "Underwater acoustic communications using time reversal," IEEE J. Ocean. Eng. **30**(4), 852–864 (2005).
[17]G. Zhang, J. M. Hovem, D. Hefeng, and L. Liu, "Coherent underwater communication using passive time reversal over multipath channels," Appl. Acoust. **72**(7), 412–419 (2011).
[18]C. He, Q. Zhang, and J. Huang, "Passive time reversal communication with cyclic shift keying over underwater acoustic channels," Appl. Acoust. **96**(9), 132–138 (2015).
[19]B. E. Anderson, T. J. Ulrich, P.-Y. Le Bas, and J. A. Ten Cate, "Three dimensional time reversal communications in elastic media," J. Acoust. Soc. Am. **139**(2), EL25–EL30 (2016).
[20]C. Larmat, J.-P. Montagner, M. Fink, Y. Capdeville, A. Tourin, and E. Clevede, "Time-reversal imaging of seismic sources and applications to the great Sumatra earthquake," Geophys. Res. Lett. **33**(19), L19312, https://doi.org/10.1029/2006GL026336 (2006).
[21]C. Larmat, J. Tromp, Q. Liu, and J.-P. Montagner, "Time-reversal location of glacial earthquakes," J. Geophys. Res. **113**(B9), B09314, https://doi.org/10.1029/2008JB005607 (2008).
[22]C. Larmat, R. A. Guyer, and P. A. Johnson, "Tremor source location using time-reversal: Selecting the appropriate imaging field," Geophys. Res. Lett. **36**(22), L22304, https://doi.org/10.1029/2009GL040099 (2009).
[23]C. S. Larmat, R. A. Guyer, and P. A. Johnson, "Time-reversal methods in geophysics," Phys. Today **63**(8), 31–35 (2010).
[24]I. Rakotoarisoa, J. Fischer, V. Valeau, D. Marx, C. Prax, and L.-E. Brizzi, "Time-domain delay-and-sum beamforming for time-reversal detection of intermittent acoustic sources in flows," J. Acoust. Soc. Am. **136**(5), 2675–2686 (2014).
[25]A. Mimani, Z. Prime, C. J. Doolan, and P. R. Medwell, "A sponge-layer damping technique for aeroacoustic time-reversal," J. Sound Vib. **342**, 124–151 (2015).

[26]A. Mimani, Z. Prime, D. J. Moreau, and C. J. Doolan, "An experimental application of aeroacoustic time-reversal to the Aeolian tone," J. Acoust. Soc. Am. **139**(2), 740–763 (2016).
[27]T. J. Ulrich, P. A. Johnson, and A. Sutin, "Imaging nonlinear scatterers applying the time reversal mirror," J. Acoust. Soc. Am. **119**, 1514–1518 (2006).
[28]T. J. Ulrich, A. M. Sutin, R. A. Guyer, and P. A. Johnson, "Time reversal and nonlinear elastic wave spectroscopy TR NEWS techniques," Int. J. Nonlin. Mech. **43**, 209–216 (2008).
[29]B. E. Anderson, M. Griffa, T. J. Ulrich, P.-Y. Le Bas, R. A. Guyer, and P. A. Johnson, "Crack localization and characterization in solid media using time reversal techniques," Am. Rock Mech. Assoc., presented at the 44th U.S. Rock Mechanics Symposium and 5th U.S.-Canada Rock Mechanics Symposium, Salt Lake City, Utah, June 2010.
[30]M. Fink, "Time-reversed acoustics," Sci. Am. **281**(5), 91–97 (1999).
[31]P. C. de Mello, N. Pérez, J. C. Adamowski, and K. Nishimoto, "Wave focalization in a wave tank by using time reversal technique," Ocean Eng. **123**, 314–326 (2016).
[32]C. Heaton, B. E. Anderson, and S. M. Young, "Time reversal focusing of elastic waves in plates for educational demonstration purposes," J. Acoust. Soc. Am. **141**(2), 1084–1092 (2017).
[33]A. Derode, A. Tourin, and M. Fink, "Ultrasonic pulse compression with one-bit time reversal through multiple scattering," J. Appl. Phys. **85**(9), 6343–6352 (1999).
[34]G. Montaldo, P. Roux, A. Derode, C. Negreira, and M. Fink, "Generation of very high pressure pulses with 1-bit time reversal in a solid waveguide," J. Acoust. Soc. Am. **110**(6), 2849–2857 (2001).
[35]B. Van Damme, K. Van Den Abeele, Y. Li, and O. Bou Matar, "Time reversed acoustics techniques for elastic imaging in reverberant and non-reverberant media: An experimental study of the chaotic cavity transducer concept," J. Appl. Phys. **109**, 104910 (2011).
[36]B. E. Anderson, M. Clemens, and M. L. Willardson, "The effect of transducer directionality on time reversal focusing," J. Acoust. Soc. Am. **142**(1), EL95–El101 (2017).
[37]M. H. Denison and B. E. Anderson, "Time reversal acoustics applied to rooms of various reverberation times," J. Acoust. Soc. Am. **144**(6), 3055–3066 (2018).
[38]F. Fahy and P. Gardonio, *Sound and Structural Vibration, Radiation, Transmission and Response* (Academic, Cambridge, MA, 2007), Vol. 26, pp. 185–195.
[39]A. Sutin, B. Libbey, V. Kurtenoks, D. Fenneman, and A. Sarvazyan, "Nonlinear detection of land mines using wide bandwidth time-reversal techniques," Proc. SPIE **6217**, 398–409 (2006).
[40]F. Ciampa and M. Meo, "Nonlinear elastic imaging using reciprocal time reversal and third order symmetry analysis," J. Acoust. Soc. Am. **131**(6), 4316–4323 (2012).
[41]focusTerra, The Earth and Science Discovery Center of ETH Zurich, available at https://focusterra.ethz.ch/en/ (Last viewed September 20, 2021).
[42]foucsTerra, "Waves, dive in!," available at https://waves.ethz.ch/en/ (Last viewed September 20, 2021).
[43]The Brigham Young University video of the time reversal LEGO demonstration, available at https://youtu.be/tCuIRNyXi6s (Last viewed September 20, 2021).
[44]The time reversal LEGO demonstration conducted in the Brigham Young University laboratory showing repeatability with the eddy current sensor, available at https://youtu.be/xbbQZo-Us80 (Last viewed September 20, 2021).
[45]The wave propagation visualization, the first time reversal LEGO demonstration video, and an optimized launch demonstration, available at https://youtu.be/emgzUa3U5bg (Last viewed September 20, 2021).

Bibliography

[1] A. A. Maznev and O. B. Wright, "Upholding the diffraction limit in the focusing of light and sound," *Wave Motion,* vol. 68, pp. 182-189, 2017.

[2] C. S. Clay and B. E. Anderson, "Matched signals: The beginnings of time reversal," *Journal of the Acoustical Society of America,* vol. 129, no. 4, pp. 2530-2530, 2011.

[3] M. Fink, "Time Reversed Acoustics," *Physics Today,* vol. 50, no. 3, pp. 34-40, 1997.

[4] Holy Bible King James Version, Church of Jesus Christ of Latter-day Saints https://www.churchofjesuschrist.org/study/scriptures/nt/matt/20, 1611.

[5] B. E. Anderson, M. Griffa, C. Larmat, T. J. Ulrich and P. A. Johnson, "Time reversal," *Acoust. Today,* vol. 4, no. 1, pp. 5-16, 2008.

[6] M. H. Denison and B. E. Anderson, "The effects of source placement on time reversal focusing in rooms," *Appl. Acoust.,* vol. 156, pp. 279-288, 2019.

[7] M. H. Denison and B. E. Anderson, "Time reversal acoustics applied to rooms of various reverberation times," *J. Acoust. Soc. Am.,* vol. 144, no. 6, p. 3055, 2018.

[8] M. Fink, "Time-reversal acoustics in biomedical engineering," *Ann. Rev.Biomed. Eng.,* vol. 5, no. 1, pp. 465-497, 2003.

[9] G. Zhang, J. M. Hovem, D. Hefeng and L. Liu, "Coherent underwatercommunication using passive time reversal over multipath channels," *Appl. Acoust.,* vol. 72, no. 7, pp. 412-149, 2011.

[10] H.-C. Song, "An Overview of Underwater Time-Reversal Communication," *IEEE J. Oceanic. Eng.,* vol. 41, no. 3, pp. 644-655, 2016.

[11] B. D. Patchett and B. E. Anderson, "Nonlinear characteristics of high amplitude focusing using time reversal in a reverberation chamber," *J. Acoust. Soc. Am.,* vol. 151, no. 6, p. 3603, 2022.

[12] B. E. Anderson, L. Pieczonka, M. C. Remillieux, T. J. Ulrich and P.-Y. L. Bas, "Stress corrosion crack depth investigation using the time reversed elastic nonlinearity diagnostic," *J. Acoust. Soc. Am.,* vol. 141, no. 1, pp. EL76-EL81, 2017.

[13] A. Mimani, "A point-like enhanced resolution of experimental Aeolian tone using an iterative point-time-reversal-sponge-layer damping technique," *Mech. Sys. Sig. Proc.,* vol. 151, p. 107411, 2021.

[14] G. Lerosey, J. d. Rosny, A. Tourin and M. Fink, "Focusing beyond the diffraction limit with far-field time reversal.," *Science,* vol. 315, no. 5815, pp. 1120-1122, 2007.

[15] F. Lemoult, M. Fink and G. Lerosey, "Acoustic resonators for far-field control of sound on a subwavelength scale," *Phys. Rev. Lett.,* vol. 107, no. 6, p. 064301, 2011.

[16] F. Ma, Z. Huang, C. Liu and J. H. Wu, "Acoustic focusing and imaging via phononic crystal and acoustic metamaterials," *J. Appl. Phys.,* vol. 131, p. 011103, 2022.

[17] C. E. Bradley, "Acoustic Bloch Wave Propagation in a Periodic Waveguide," Technical Report of Applied Research Laboratories, ARL-TR- 91-19 (July), The University of Texas at Austin, 1991.

[18] N. Sugimoto and T. Horioka, "Dispersion characteristics of sound waves in a tunnel with an array of Helmholtz resonators," *J. Acoust. Soc. Am.,* vol. 97, no. 3, pp. 1446-1459, 1995.

[19] A. Maznev, G. Gu, S.-y. Sun, J. Xu, Y. Shen, N. X. Fang and S.-y. Zhang, "Extraordinary focusing of sound above a soda can array without time reversal," *New Journal of Physics,* vol. 17, no. 4, p. 042001, 2015.

[20] C. T. Vongsawad, T. B. Neilsen, A. D. Kingsley, J. E. Ellsworth, B. E. Anderson, K. N. Terry, C. E. Dobbs, S. E. Hollingsworth and G. H. Fronk, "Design of an underwater acoustics lab," *Proc. Mtgs. Acoust.,* vol. 45, no. 070005, 2021.

[21] A. Parvulescu and C. S. Clay, "Reproducibility of signal transmissions in the ocean," *Radio and Electronic Engineer,* vol. 29, no. 4, pp. 223-228, 1965.

[22] B. E. Anderson, M. . Griffa, T. J. Ulrich and P. A. Johnson, "Time reversal reconstruction of finite sized sources in elastic media," *Journal of the Acoustical Society of America,* vol. 130, no. 4, p. , 2011.

[23] A. D. Kingsley, B. E. Anderson and T. J. Ulrich, "Super-resolution within a one-dimensional phononic crystal of resonators using time reversal in an equivalent circuit model," *J. Acoust. Soc. Am.,* vol. 152, no. 3, pp. 1263-1271, 2022.

[24] "Solve systems of linear equations Ax = B for x," Mathworks, [Online]. Available: https://www.mathworks.com/help/matlab/ref/mldivide.html. [Accessed Oct. 2022].

[25] L. E. Kinsler, A. R. Frey, A. B. Coppens and J. V. Sanders, Fundamentals of acoustics, John wiley & sons, 2000.

[26] J. Kergomard and A. Garcia, "Simple discontinuities in acoustic waveguide at low frequencies: critical analysis and formulae," *Journal of Sound and Vibration,* vol. 114, pp. 465-479, 1987.

[27] A. N. Norris and I. C. Sheng, "Acoustic radiation from a circular pipe with an infinite flange," *Journal of Sound and Vibration,* vol. 135, pp. 85-93, 1989.

[28] J.-P. Dalmont, C. J. Nederveen and N. Joly, "Radiation impedance of tubes with different flanges: numerical and experimental investigations," *Journal of Sound and Vibration,* vol. 244, no. 3, pp. 504-534, 2001.

[29] U. Ingard, "On the Theory and Design of Acoustic Resonators," *J. Acoust. Soc. Am.,* vol. 25, p. 1037, 1953.

[30] U. Ingard, "The Near Field of a Helmholtz Resonator Exposed to a Plane Wave," *J. Acoust. Soc. Am.,* vol. 25, p. 1062, 1953.

[31] J. Dang, C. H. Shadle, Y. Kawanishi, K. Honda and H. Suzuki, "An experimental study of the open end correction coefficient for side branches within an acoustic tube," *J. Acoust. Soc. Am.,* vol. 104, p. 1075, 1998.

[32] M. Alster, "Improved calculation of resonant frequencies of Helmholtz resonators," *Journal of Sound and Vibration,* vol. 24, no. 1, pp. 63-85, 1972.

[33] Z. L. Ji, "Acoustic length correction of closed cylindrical side-branched tube," *Journal of Sound and Vibration,* vol. 283, no. 3-5, pp. 1180-1186, 2005.

[34] A. D. Kingsley, J. M. Clift, B. E. Anderson, J. E. Ellsworth, T. J. Ulrich and P.-Y. L. Bas, "Development of software for performing acoustic time reversal with multiple inputs and outputs," *Proc. Meet. Acoust.,* vol. 46, no. 055003, 2022.

[35] B. Zimmermann and C. Studer, "FPGA-based real-time acoustic camera prototype," *Proceedings of 2010 IEEE International Symposium on Circuits and Systems,* p. 1419, 2010.

[36] G. Montaldo, P. Roux, A. Derode, C. Negreira and M. Fink, "Ultrasound shock wave generator with one-bit time reversal in a dispersive medium, application to lithotripsy," *Applied Physics Letters,* vol. 80, no. 5, pp. 897-899, 2002.

[37] B. E. Anderson, M. C. Remillieux, P.-Y. L. Bas and T. J. Ulrich, "Time reversal techniques," in *Nonlinear Acoustic Techniques for Nondestructive Evaluation*, 1st ed., T. Kundu, Ed., Springer and Acoustical Society of America, 2018, pp. 547-581.

[38] M. A. Jaimes and R. Snieder, "Spatio-temporal resolution improvement via weighted time-reversal," *Wave Motion,* vol. 106, no. 102803, 2021.

[39] C. Larmat, J.-P. Montagner, M. Fink, Y. Capdeville, A. Tourin and E. Clevede, "Time-reversal imaging of seismic sources and application to the great Sumatra earthquake," *Geophys. Res. Lett.,* vol. 33, p. L19312, 2006.

[40] J. d. Rosny and M. Fink, "Overcoming the Diffraction Limit in Wave Physics Using a Time-reversal Mirror and a Novel Acoustic Sink," *Phys. Rev. Lett.,* vol. 89, no. 12, p. 124301, 2002.

[41] G. Ma, X. Fan, F. Ma, J. d. Rosny, P. Sheng and M. Fink, "Towards anti-casual Green's function for three-dimensional sub-diffraction focusing," *Nature Phys.,* vol. 14, no. 6, pp. 608-612, 2018.

[42] S. G. Conti, P. Roux and W. A. Kuperman, "Near-field time-reversal amplification," *J. Acoust. Soc. Am.,* vol. 121, no. 6, p. 3602, 2007.

[43] M. Tanter, J. Thomas and M. Fink, "Time reversal and the inverse filter," *J. Acoust. Soc. Am.,* vol. 108, no. 1, pp. 223-234, 2000.

[44] K. F. Warnick, "MIMO communications and inverse scattering," *2009 IEEE Antennas and Propagation Society International Symposium,* pp. 1-4, 2009.

[45] C. Prada and M. Fink, "Eigenmodes of the time reversal operator: A solution to selective focusing in multiple-target media," *Wave Motion,* vol. 20, pp. 151-163, 1994.

[46] C. Prada and J.-L. Thomas, "Experimental subwavelength localization of scatterers by decomposition of the time reversal operator interpreted as a covariance matrix," *J. Acoust. Soc. Am.,* vol. 114, no. 235, 2003.

[47] B. D. Patchett, B. E. Anderson and A. D. Kingsley, "The impact of room location on time reversal focusing amplitudes," *J. Acoust. Soc. Am.,* vol. 150, no. 2, pp. 1424-1433, 2021.

[48] B. E. Anderson, M. Clemens and M. L. Willardson, "The effect of transducer directivity on properties of time reversal focusing," *J. Acoust. Soc. Am.,* vol. 139, no. 4, p. 2083, 2016.

[49] C. Heaton, B. E. Anderson and S. M. Young, "Time reversal focusing of elastic waves in plates for an educational demonstration," *J. Acoust. Soc. Am.,* vol. 141, pp. 1084-1092, 2017.

[50] C. G. B. Garrett and D. E. McCumber, "Propagation of a Gaussian light pulse through an anomalous dispersion medium," *Physical Review A,* vol. 1, no. 2, p. 305, 1970.

[51] S. Chu and S. Wong, "Linear Pulse Propagation in an Absorbing Medium," *Phys. Rev. Lett.,* vol. 48, no. 11, p. 738, 1982.

[52] A. Sutin and H. Salloum, "Prospective medical applications of nonlinear time reversal acoustics," *Proc. Meet. Acoust.,* vol. 34, no. 1, p. 020003, 2018.

[53] B. E. Anderson, M. Griffa, T. J. Ulrich, P.-Y. L. Bas, R. A. Guyer and P. A. Johnson, "Crack localization and characterization in solid media using time reversal techniques," *Am. Rock Mech. Assoc.,* vol. 10, no. 154, 2010.

[54] S. M. Young, B. E. Anderson, S. M. Hogg, P.-Y. L. Bas and M. C. Remillieux, "Nonlinearity from stress corrosion cracking as a function of chloride exposure time using the time reversed elastic nonlinearity diagnostic," *J. Acoust. Soc. Am.,* vol. 145, no. 1, pp. 382-391, 2019.

[55] C. S. Larmat, R. A. Guyer and P. A. Johnson, "Time-reversal methods in geophysics," *Phys. Today,* vol. 63, no. 8, pp. 31-35, 2010.

[56] R. K. Ing and N. Quieffin, "In solid localization of finger impacts using acoustic time-reversal process," *Appl. Phys. Lett.,* vol. 87, no. 20, p. 204104, 2005.

[57] A. A. E. Ouahabi, L. Chisari and G. Memoli, "Analytical and experimental investigation of the transmission/reflection coefficient from labyrinthine metamaterials," *Proc. Meet. Acoust.,* vol. 42, p. 065003, 2020.

[58] V. S. Gomez, I. Spiousas and M. C. Eguia, "Time reversal focusing in the audible range using a tunable sonic crystal," *J. Acoust. Soc. Am.,* vol. 149, no. 6, pp. 4024-4035, 2021.

[59] B. V. Damme, K. V. D. Abeele, Y. Li and O. B. Matar, "Time reversed acoustics techniques for elastic imaging in reverberant and nonreverberant media: An experimental study of the chaotic cavity transducer concept," *J. Appl. Phys.,* vol. 109, no. 10, p. 104910, 2011.